**UNIVERSITÄT PADERBORN**
*Die Universität der Informationsgesellschaft*

# 245 GHz Subharmonic Receivers For Gas Spectroscopy in SiGe BiCMOS Technology

Der Fakultät für Elektrotechnik, Informatik und Mathematik
der Universität Paderborn

zur Erlangung des akademischen Grades

Doktor der Ingenieurwissenschaften (Dr.-Ing.)

vorgelegte Dissertation
von

Dipl.-Ing. Yanfei Mao
geboren am 01.09.1983 in Yiwu

Zusammenfassung der Dissertation:

## 245 GHz Subharmonic Receivers
## For Gas Spectroscopy in SiGe BiCMOS
## Technology

### von Frau Yanfei Mao

   Millimeterwellen -Gas-Spektroskopie ermöglicht die hochgenaue Detektion von Gasen auf Basis ihrer typischen Absorptionsspektren im Vakuum. Die Anregungsfrequenzen für die Gasspektroskopie liegen dabei typischerweise im höheren Millimeterwellen-Bereich. Für die vorliegende Anwendung wurde eine Mittenfrequenz von 245 GHz gewählt. Ziel der Arbeit ist die Realisierung eines integrierten 245-GHz-Empfängers in SiGe BiCMOS-Technologie. Zunächst wird das Wellenleiter-Design für einen 122 GHz Kaskode-LNA untersucht. Verschiedene Topologien für die Leitungen werden in der gleichen LNA-Topologie implementiert und verglichen. Dann wird das Schaltungsdesign von LNAs diskutiert und ein mehrstufiger 245-GHz-LNA in Basisschaltung untersucht. Im nächsten Schritt warden 245-GHz-Implementierungen von aktiven und passiven subharmonischen Mischern untersucht und realisiert. Daraufhin werden drei integrierte subharmonische 245-GHz-Empfänger untersucht und verglichen. Schließlich wird ein subharmonischer Empfänger in einer Gasspektroskopie-Anwendungen erfolgreich erprobt.

UNIVERSITÄT PADERBORN
*Die Universität der Informationsgesellschaft*

Summary of Dissertation:

## 245 GHz Subharmonic Receivers
## For Gas Spectroscopy in SiGe BiCMOS
## Technology

### By  Ms Yanfei Mao

Millimeter-wave gas spectroscopy enables the precise detection of gases based on their typical absorption spectra in vacuum. Excitation frequencies for gas spectroscopy lie typically in the high millimeter-wave region. For the presented gas spectroscopy application a center frequency of 245 GHz was chosen. Target of this work is the realization of an integrated 245 GHz receiver in SiGe BiCMOS technology. Initially the on-chip transmission line design for a 122 GHz cascade LNA is investigated. Different transmission line topologies are implemented in different version of the same 122 GHz LNA and compared. Then the circuit design of LNAs is discussed and a multi-stage common-base LNA at 245 GHz is investigated. Then in a next step 245 GHz implementations of different active and passive subharmonic mixers are investigated and realized. Furthermore three integrated subharmonic 245 GHz receivers are investigated and compared. Finally a subharmonic receiver is used successfully in a gas spectroscopy application.

## Dissertation

## 245 GHz Subharmonic Receivers

## For Gas Spectroscopy in SiGe BiCMOS Technology

25. November 2014
Yanfei Mao

## Contents

# 1    Introduction

## 1.1    Motivation

An ISM band at 245 GHz with 2 GHz bandwidth is available in Europe, which could be used for imaging radar for security applications, bio-medical sensors for medical diagnostics [1].

In this work, 245 GHz receivers are studied for the gas spectroscopy application. Gas spectroscopy is a technique based on the vibration of the atoms of a gas molecule. A spectrum is obtained by passing microwave radiation through a sample and determining what fraction of the incident radiation is absorbed at a particular energy. The energy at which any peak in an absorption spectrum appears corresponds to the frequency of a vibration of a part of a sample molecule.[2]

Recently in [3], a millimeter-wave spectroscopy in the band of 210-270 GHz was presented. The results showed that mm-wave spectroscopy can be used to detect a variety of gases such as HCN, $CH_2CL_2$, $CH_3CL$ and so on (in total a family of 32 kinds of gases) with high accuracy using only electronic sources and detectors. The measurement setup for the experiment is shown in Fig. 1.1.
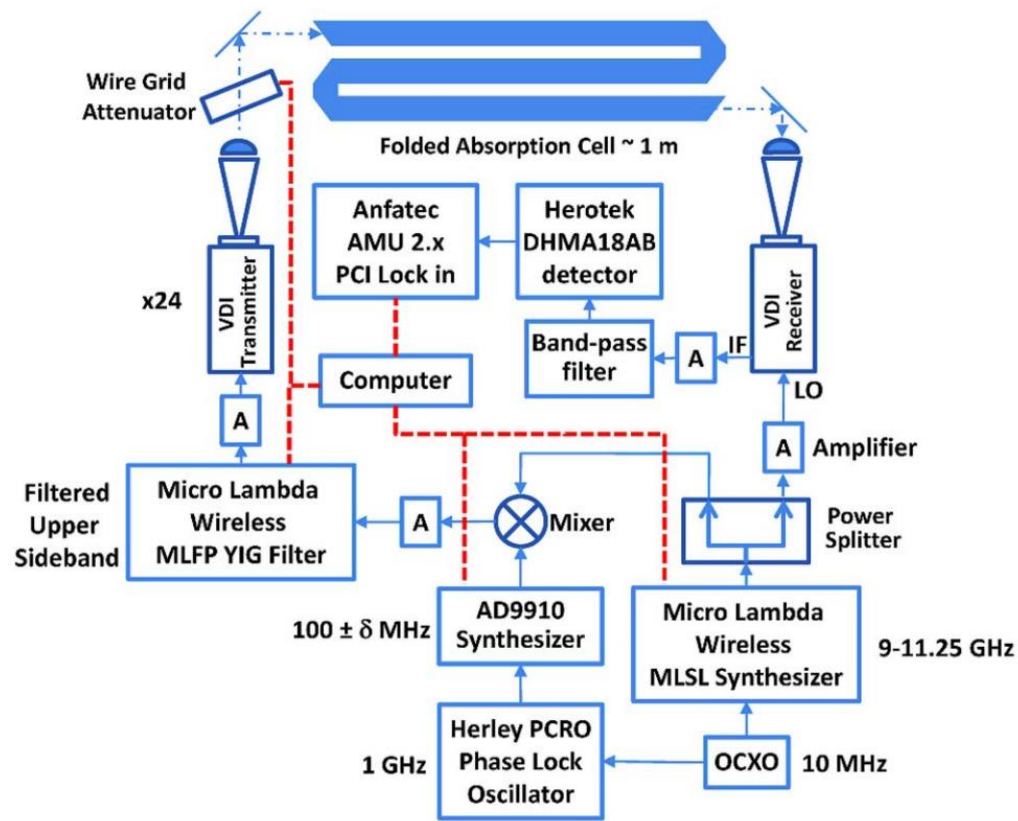
Figure 1.1 Overview of a SMM frequency multiplication, heterodyne receiver gas sensor

In figure 1.1, in this system a frequency synthesizer near 10 GHz drives a 24 diodebased frequency multiplier to provide the local oscillator of a heterodyne receiver. A sideband generation scheme provides synchronized, but offset in frequency, drive to a similar multiplier chain for probe power to the folded 1.2 m absorption cell.

While [3] used instrumentation synthesizers and expensive as well as complex measurmement equipment, this paper investigates highly-integrated receivers based on SiGe BiCMOS technology to provide a low cost solution for detector in gas spectroscopy. In the future such sensor electronics could be used for low-cost, miniaturized gas sensors. Applications could be e.g. for use climate control (detection of O2, CO, CO2), detection of toxical industrial gases in production sites, environmental monitoring or medical applications such as breathing gas analysis.

At the time of the start of this work no high-frequency gas spectroscopy systems using highly-integrated ICs in GaAs, InP or Si technologies were reported. The advances in silicon semiconductor technology, especially SiGe BiCMOS technology and the successful demonstration of a purely electronic gas spectroscopy detection system, motivated this work.

For frequency as high 120 GHz or 240 GHz, passive design becomes crucial. In this thesis, transmission line designs upon 120 GHz LNA are discussed and different transmission line topologies are compared in the same 120 GHz cascode LNA design.

In [4] a fully differential 220 GHz integrated receiver front-end without VCO has been demonstrated in SiGe technology. Both the LNA and the active subharmonic mixer are implemented with differential signaling. Although differential signaling is more robust to common-mode noise, it comes at the expense of higher power and more complicated LO distributions. In order to reduce power dissipation, single-ended receiver structure is chosen in this work. Hence receivers comprising of the single-ended LNA and single-ended subharmonic mixers (SHMs) are proposed and compared.

LNAs with different topologies, such as common emitter, cascode are reported. In [5] using SiGe technology, a differential 3 stage common emitter LNA at 60 GHz with 18 dB gain and 22 GHz 3dB bandwidth is reported. In [6] a two stage cascode SiGe LNA with 13.5 dB gain and a noise figure of 9.6 dB at 122 GHz is reported. In [4] a differential 3 stage cascode LNA at 220 GHz with 15 dB is reported. In [7], A five-stage differential SiGe low noise amplifier (LNA) in cascode topology with 18 dB gain at 245 GHz is presented. In this thesis, a four stage common base 245 GHz LNA boasting of high gain, low noise and lower power is introduced. Simulation and meausrement results are given.

With respect to mixer design, subharmonic mixers (SHM) offer an alternative solution to fundamental mixers in the millimeter-wave range since they allow for a local oscillator at lower frequency. In [8], a $2^{nd}$ active subharmonic mixer based on two stacked switching quads with conversion gain of 21 dB at 122 GHz and noise figure of 21 dB is reported. In [9] $2^{nd}$ transconductance subharmonic balanced mixers with 0.7 dB conversion gain at 77 GHz are demonstrated. In [10] a $4^{th}$ transconductance SHM at 650 GHz with -13 dB conversion gain and 42 dB noise figure is presented. In [11] a $4^{th}$ passive GaAs monolithic subharmonic mixer with a maximum conversion loss of 13.2 dB is achieved at 60 GHz. This thesis investigates and compares the two single-ended subharmonic mixers: transconductance SHM and passive SHM.

Utilizing CB LNA, $4^{th}$ transconductance SHM, $2^{nd}$ transconductance SHM and $2^{nd}$ passive SHM, three integrated single-ended 245 GHz receivers were implemented and compared. One subharmonic receiver: $2^{nd}$ transconductance subharmonic receiver is chosen to be demonstrator in gas spectroscopy application.

## 1.2 Organization of the Dissertation

The theis is organized as follows. In Chapter 2, transmission line design for 122 GHz cascode LNA design is discussed. Different transmission line topologies in a same cascode LNA are compared. In Chapter 3, circuit design of LNAs is discussed and multi-stage CB LNA is presented. Simulation and measurement results for CB LNA are given. In Chapter 4, design of transconductance subharmonic mixer and passive subharmonic mixer are investigated and realized. Meausurement and simulation results of subharmonic mixers are given. In Chapter 5, simulation and measurement results of three integrated subharmonic receivers comprising of CB LNA and SHMs are shown and compared. In Chapter 6, a subharmonic receiver in gas spectroscoy application is described. Basic system design considerations are made and measurements results are presented. Finally, conclusions are given in Chapter 7.

# 2 Design and Modeling of Integrated Passive Devices Beyond 100 GHz

## 2.1 Description of Semiconductor Technology

Three kinds of IHP BiCMOS technologies are available throughout the design of various circuits in this thesis. Different technologies are utilized for different circuits.

Dotfive is an experimental 0.25 μm SiGe BiCMOS technology. The technology has 5 metal layers. The 5 metal layers include 3 aluminum metal layers and 2 top-metal layers with 2μm and 3μm thickness, respectively. Low-loss transmission lines could be designed with the two thick top-metal layers. The $f_T$ and $f_{max}$ of the experimental transistors are reported to be 300 GHz and 500 GHz, respectively [35]. Dotfive technology includes resistors $R_{sil}$ and $R_{ppd}$, MIM (metal-insulator-metal) capacitors, MOS varicaps and Schottky diodes. $R_{sil}$ utilizes salicided, n-doped gate polysilicon as resistor material. $R_{ppd}$ utilize unsalicided, p-doped gate polysilicon as resistor material [36].

SG13S is IHP's standard 0.13 μm SiGe BiCMOS technology. The SG13S technology has 7 aluminum layers. The 7 layers include 5 thin metal layers and 2 top-metal layers with 2μm and 3μm thickness, respectively. The $f_T$ and $f_{max}$ of the SiGe heterobipolar transistors are 250 GHz and 300 GHz, respectively [37]. SG13S technology includes resistors $R_{sil}$, $R_{ppd}$ and $R_{high}$, MIM (metal-insulator-metal) capacitors, MOS varicaps, and Schottky diodes. $R_{sil}$ utilizes salicided, n-doped gate polysiliconas resistor material. $R_{ppd}$ utilize unsalicided, p-doped gate polysilicon as resistor material. $R_{high}$ utilizes unsalicided, partially compensated gate polysilicon as resistor material [38].

SG13G2 is an improved 0.13 μm SiGe BiCMOS technology. The technology has the same metal layers, CMOS transistors, and passive devices as SG13S but offers different SiGe heterobipolar transistors. The $f_T$ and $f_{max}$ of the transistor are 300 GHz and 500 GHz, respectively [39]. [40].

## 2.2 Resistors

Resistors are utilized in bias circuits for LNA, subharmonic mixers and so on. Resistors are usually not utilized in matching networks. In order to achieve lossless matching in narrow band circuitry, transmission lines, inductors, and

MIM capacitors are typically used in matching networks to achieve low loss and low noise.

Figure 2.1 shows the frequency modeling of a polysilicon resistor. C1, C2 are parasitic capacitance between terminals of the resistor and polysilicon layertowards the substrate. C3 is parasitic capacitance between the terminals of resistor.
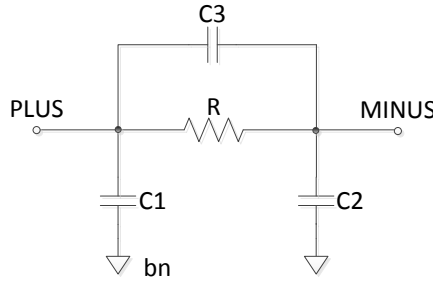


Figure 2.1 High frequency modeling of the resistor

## 2.3    Capacitors

MIM capacitors are fabricated between metal 5 and top metal 1, an insulator layer is inserted between metal 5 and top metal 1.

Capacitance calculation for the MIM capacitor is as follows:

$$C = l * w * c_{MIM} + 2 * (l + w) c_{PER} \qquad (2.1)$$

In equation 2.1, l is length, w is width, $c_{MIM}$ is specific area capacitance, $c_{PER}$ is specific perimeter capacitance.

In my simulations, MIM spectre model was utilized even beyond 100 GHz. No EM simulation of the substrate capacitance was included.

MIM capacitors are utilized in various circuits presented in this thesis. Compared to MOS capacitors, MIM capacitors have higher Q factor and more accurate capacitance modeling, less tolerance, and constant capacitance wrt. the applied voltage. Therefore they are preferred for high-frequency circuit design.

Accumulation type MOS varicap is utilized as variable capacitors in VCOs. In [27], with accumulation type MOS varicap, phase noise of -82dBc/Hz at 1 MHz offset is measured at 1.5 V with corresponding LO frequency of 122 GHz.

## 2.4     High-Frequency Probe Pads

Input and output RF bondpads in this thesis are realized by top metal 2. Metal 1 shielding is adopted for the RF bondpads to prevent substrate loss and obtain a high Q pad capacitance.

Figure 2.2 shows the "Ground-Signal-Ground" (GSG) bondpad for 245 GHz RF signal of 245 GHz LNA. Pitch length of the GSG bondpad is 70 um. Figure 2.3 shows the GSG bondpad for 120 GHz RF signal of 120 GHz LNA. Pitch length of the GSG bondpad is 100 um. Figure 2.4 shows the GSGSG bondpad for 1 GHz IF signal and DC signals of subharmonic mixer. Pitch length of the GSGSG bondpad is 100 um. Different bondpads are designed for different frequencies because different probes are utilized for different frequencies.

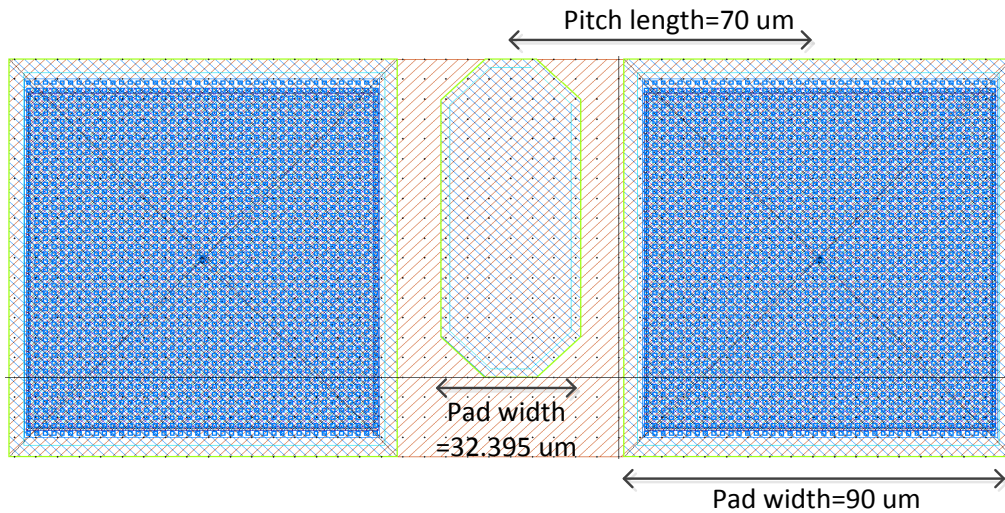ADS momentum is utilized for EM simulation of the bondpads.
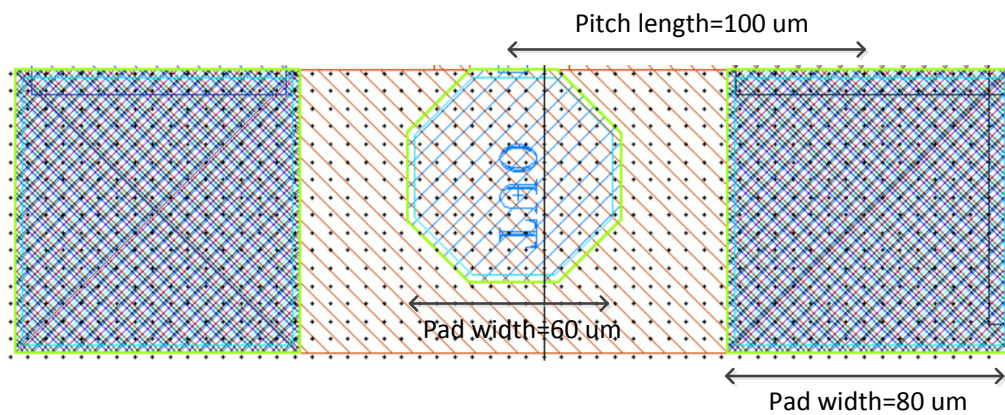


Figure 2.2 GSG bondpad for 245 GHz RF signal



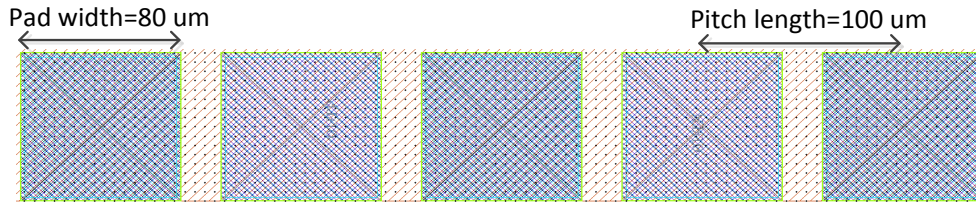Figure 2.3 GSG bondpad for 120 GHz RF signal

Figure 2.4 GSGSG bondpad for 1 GHz IF and DC signals

## 2.5    Inductors vs. Transmission Lines

For frequency beyond 100 GHz, wavelength of RF signals is less than 3 mm in the air, and around less than 1.5 mm in silicon dioxide with $\varepsilon_r$=4. Quarter wavelength of RF signals is less than 750 um in the air, and around less than 375 um in silicon dioxide with $\varepsilon_r$=4. For wavelength smaller than 375 μm, it is area efficient to utilize shorted transmission lines as inductors (see also chapter 2.6).

With metal 1 as return ground, low loss, high Q transmission lines can be easily realized as inductors. Metal 1 performs as shielding to prevent substrate loss.

Traditional planar integrated inductors in comparison suffer from substrate loss and threrefore lead to lower Q factors.

For all the reasons mentioned above, in this thesis, transmission lines are vastly used as inductors in various circuit blocks. More details on transmission line design follow in succeeding part of the thesis.

## 2.6    Basic Transmission Line Theory [12]

A transmission line is often schematically represented as a two-wire line, since transmission line always has at least two conductors [12].

Wave propagation on a transmission line of the lumped element model is shown as in equation 2.2 and 2.3. In equation 2.4, $Z_0$ represents the characteristic impedance of the transmission line. L represents the total self inductance of the two conductors, and the shunt capacitance C is due to the close proximity of the two conductors. The series resistance R represents the resistance due to the finite conductivity of the conductors, and the shunt conductance G is due to dielectric loss in the material between the conductors. γ is the complex propagation constant.

$$V(z) = V_o^+ e^{-\gamma z} + V_o^- e^{\gamma z} \tag{2.2}$$

$$I(z) = \frac{\gamma}{R + j\omega L}[V_o^+ e^{-\gamma z} - V_o^- e^{\gamma z}] \qquad (2.3)$$

$$Z_0 = \frac{R + j\omega L}{\gamma} = \sqrt{\frac{R + j\omega L}{G + j\omega C}} \qquad (2.4)$$

$$\gamma = \alpha + j\beta = \sqrt{(R + j\omega L)(G + j\omega C)} \qquad (2.5)$$

The above equations are referring to general transmission lines, including loss effects. In many practical cases, the loss of the line is very small, and can be neglected, resulting in a simplification of the above results. Setting R=G=0 yields:

$$\gamma = \alpha + j\beta = j\omega\sqrt{LC} \qquad (2.6)$$

$$Z_0 = \sqrt{\frac{L}{C}} \qquad (2.7)$$

$$V(z) = V_o^+ e^{-j\beta z} + V_o^- e^{j\beta z} \qquad (2.8)$$

$$I(z) = \sqrt{\frac{C}{L}}[V_o^+ e^{-j\beta z} - V_o^- e^{j\beta z}] \qquad (2.9)$$

The wavelength is

$$\lambda = \frac{2\pi}{\beta} = \frac{2\pi}{\omega\sqrt{LC}} \qquad (2.10)$$

and phase velocity is

$$v_p = \frac{\omega}{\beta} = \frac{1}{\sqrt{LC}} \qquad (2.11)$$

The input impedance of a length of transmission line with an arbitrary load is [12]

$$Z_{in} = Z_0 \frac{Z_L + jZ_0 \tan \beta l}{Z_0 + jZ_L \tan \beta l} \qquad (2.12)$$

With equation 2.12, 4 special cases of lossless terminated transmission lines are discussed as follows.

Consider the transmission line terminated in a short circuit, $Z_L = 0$.

$$Z_{in} = jZ_0 \tan \beta l \qquad (2.13)$$

As mentioned in the previous chapter shorted transmission lines with length of less than a quarter wavelength can be used effectively for inductor re-

alizations. Now consider the transmission line terminated with an open, i.e. $Z_L = \infty$. then

$$Z_{in} = -jZ_0 \cot \beta l \tag{2.14}$$

Consider the terminated transmission line with length of $l = \lambda/2$, then

$$Z_{in} = Z_L \tag{2.15}$$

Consider the terminated transmission line with some special length. If $l = n\lambda/4$, for n=1, 3,5,7... the impedance becomes

$$Z_{in} = \frac{Z_0^2}{Z_L} \tag{2.16}$$

Equation 2.16 shows the principle of quarter-wave transformer.

## 2.7    Investigation of Integrated Transmission Line Topologies

Passive design is critical for the circuit performance. In order to achieve low loss matching, high Q transmission lines and MIM capacitors are utilized in matching networks. With low loss matching network, high gain, low noise and low power circuitry could be designed.

Therefore different transmission line topologies were investigated before the active circuit design was started. Various topologies of transmission lines are reported in the literature and investigated in this thesis. Inverted transmission line is reported in [13] and utilized for 122 GHz LNA matching and biasing. A classical microstrip transmission line is reported e.g. in [14] where it is used for 60 GHz LNA matching. Microstrip with side-shielding is reported in [15] and used for matching purposes in an SHM upconverter and frequency doubler.

In this work, three transmission line (TL) topologies are simulated in ADS momentum and compared [16]. The transmission lines are fabricated in SG13S BiCMOS technology. The $f_T$ and $f_{max}$ of the transistors are 250 GHz and 300 GHz, respectively. This technology has 7 metal layers. The 7 metal layers include 5 aluminum metal layers and 2 top-metal layers with 2um and 3um thickness respectively. Low-loss transmission lines could be designed with the two thick top-metal layers. Figure 2.5 shows the three types of transmission lines with its layer stack and size; the side-shielding transmission line with TM2 as conductor, with M1 as ground and with side metal shielding (TL A); the inverted transmission line with TM2 as ground, and TM1 as the conductor

(TL B); the inverted transmission with TM2 as ground, TM1 as conductor, and surrounding metal layers as complete ground shielding (TL C).[16]
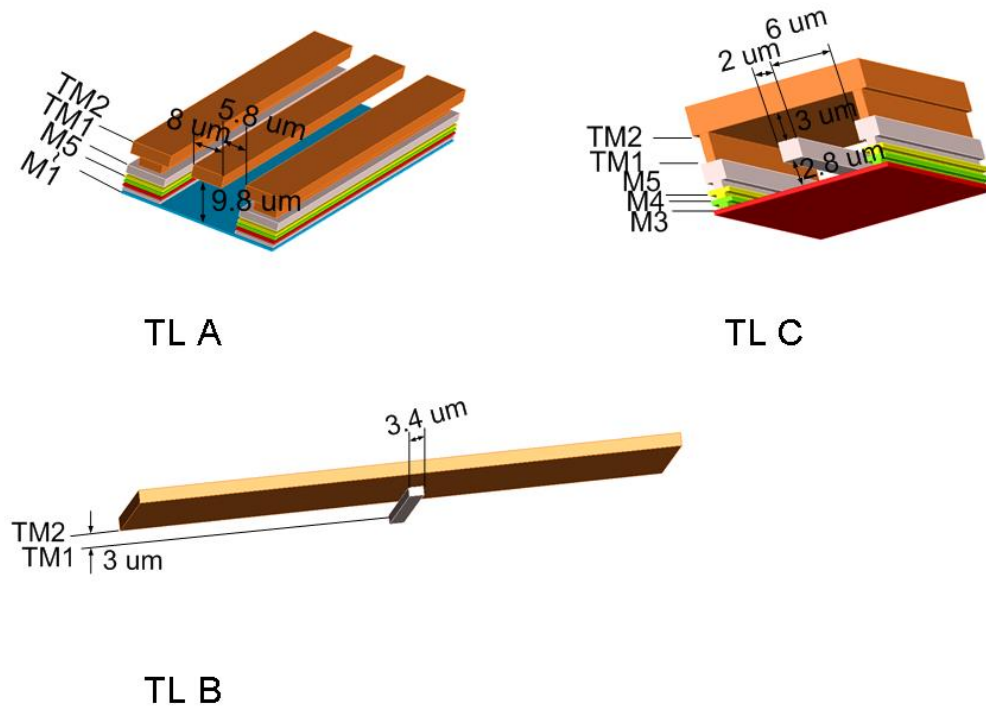


Figure 2.5: Layer stack and physical size of the three investigated types of

transmission lines

Figure 2.6 shows the Q factor comparison of the three shorted transmission lines with the same inductance value (60 pH) and the same characteristic impedance (50 Ω). Both TL A and TL C have substrate shielding. Due to complete ground shielding, TL C has larger shunt capacitance, and conductor width of TL C is smaller to have the same characteristic impedance. Thus more loss is introduced and Q factor is smaller. Comparing TL B and TL C, even if TL B has substrate loss, due to wider conductor width, its loss is smaller than that of TL C, and Q factor is larger. Q factor of TL A is larger than that of TL B due to wider conductor width and no substrate loss.

Figure 2.6: Simulated Q factor of the three types of transmission lines. For comparison purpose all TLs are designed as shorted transmission lines with 60 pH of input impedance and a characteristic impedance of 50 $\Omega$

## 2.8    Comparison of LNAs with different transmission line topologies

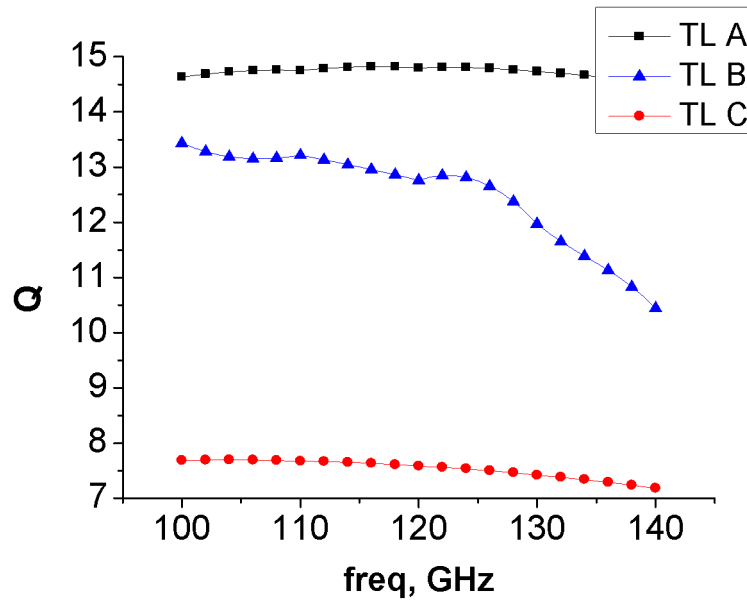In section 2.7, figure 2.6 shows the simulation results of Q quality factor comparison of the three shorted transmission lines with the same inductance value (60 pH) and the same characteristic impedance (50 $\Omega$). In this section, LNAs with these different transmission line topologies are designed, measured, and compared.

Figure 2.7 shows the schematic of the two stage cascode LNA for 122 GHz. Cascode structure is chosen for each stage for its high gain, high isolation, and wide bandwidth [13], [6]. Transmission lines TL2, TL3 are utilized as the load for each stage. Transmission line TL1 and Metal-insulator-metal capacitor MIM 1 are used for the input matching; MIM 2 is utilized for inter stage matching and decoupling; MIM 3 is for output matching. Both input and output bondpad capacitors are included for the input and output matching and the input and output matching impedance $Z_{in}$ and $Z_{out}$ are 50 Ohm. Capacitors MIM 4, MIM 5, MIM 6 provide ac ground for the load transmission lines TL2, TL3, and transmission line short stub TL1. Capacitors MIM_CB1, MIM_CB2 provide ac ground for the cascode transistors. Resistors R5, R6 are inserted for decoupling of the two stages and for preventing oscillations [6]. Unconditional stability of the LNA is verified for each stage and as well the two stages together to ensure a robust design [17]. A power supply of 3.3V is used.
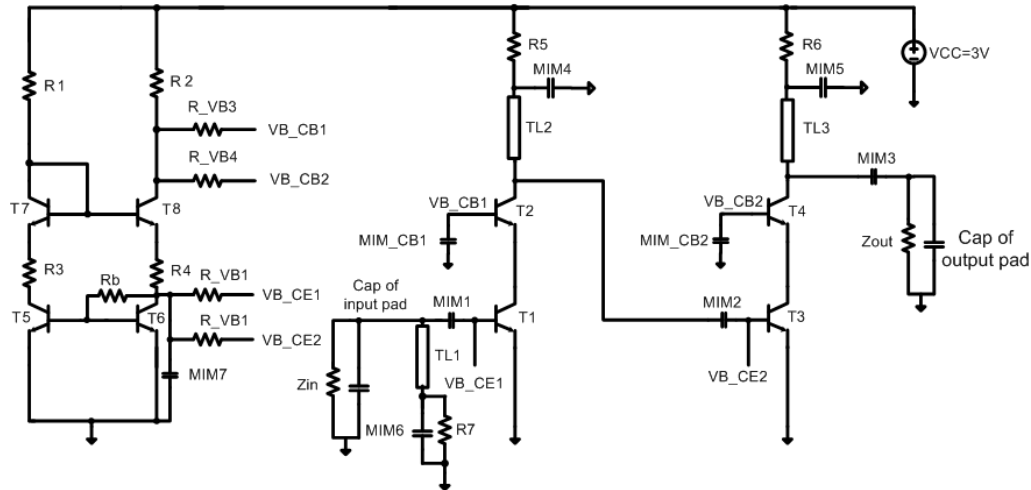
Figure 2.7: Circuit schematic of LNA

The bias circuits for the LNA are also shown in figure 2.7. VB_CE1,2 set the base bias voltage for the common emitter transistor T1, T3; VB_CB1,2 set the base bias voltage for the cascode transistor T2, T4. Resistors R_VB1,2 do not only force the base-emitter voltage of T6 equal to that of the common emitter transistor of the LNA T1, T3, but as well are chosen large values to reduce noise contribution by the bias circuits. With resistor R1, R2 and R3, R4, voltage VB_CB1,2 could be easily tuned. Because the bias circuit forms positive current feedback by the two current mirrors T5 and T6, T7 and T8, there is potential stability problem. The stability of the bias circuit was checked by ac and transient simulation.

Three LNAs with above mentioned different transmission lines as described in Sect. 2.7 were fabricated by IHP in 130nm SG13S BiCMOS technology. The layout overview of the three LNAs are shown in figure 2.8. The chip size is 0.38*0.51 mm$^2$, 0.51*0.51 mm$^2$, 0.37*0.52 mm$^2$ respectively for LNA with TL A, TL B and TL C. LNAs with TL A, TL C have more compact area than LNA with TL B. GSG bond pad with 100um pitch length and M1 substrate shielding is utilized for the on wafer measurement. On the left and right side are the input and output bondpads. On the top are the VCC pads. Channel stop implant was blocked at critical places like input, output pad, transmission lines, long interconnects etc., in order to reduce the ohmic loss. Large areas of decoupling MIM capacitors are also included in the chip between the supply and the ground.

LNA with TL A



LNA with TL B

0.37 mm

0.52 mm
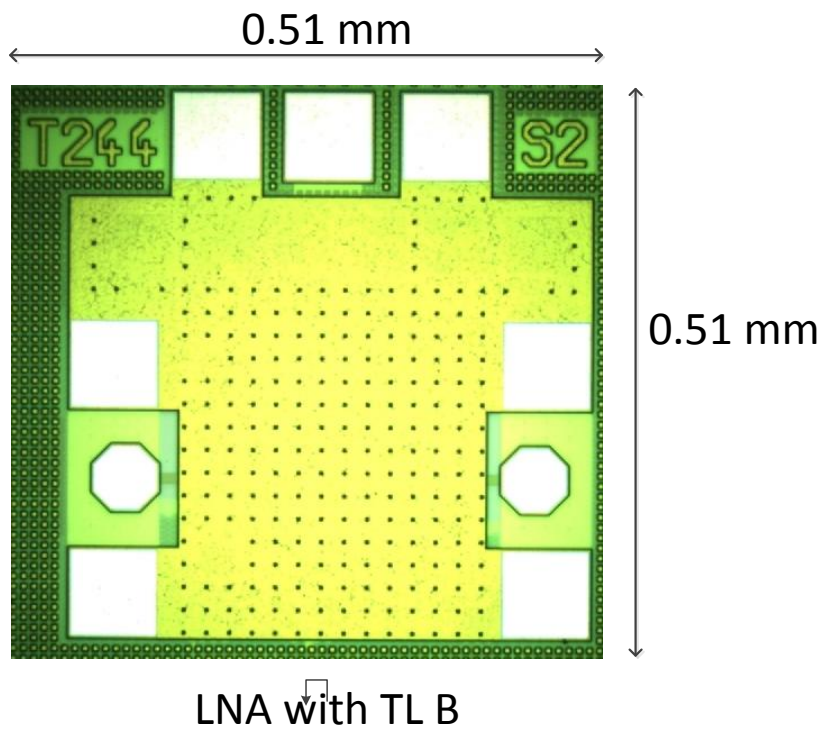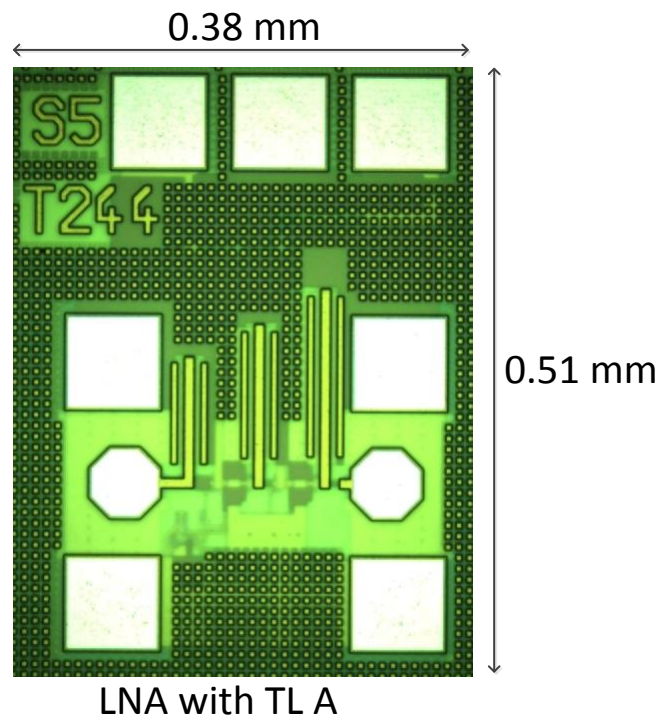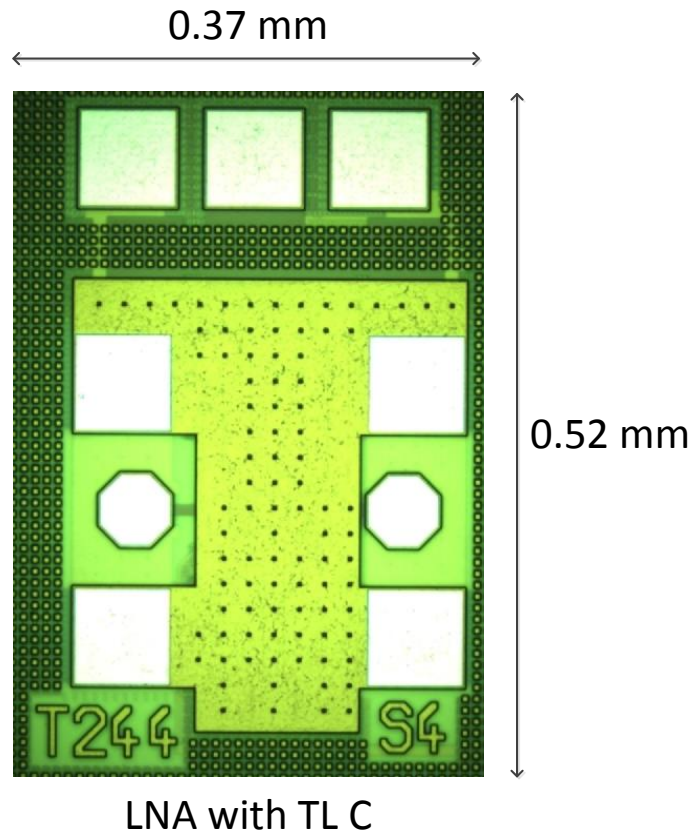
LNA with TL C

Figure 2.8: Chip photos of the LNAs with TL A, TL B, TL C

For different transmission lines, different design methodologies are used. For LNA with TL B, full-chip EM simulation of the critical passives including transmission line, input pad, output pad, long metal interconnections etc. is performed. Full-chip EM simulation is in principle most accurate way to design passives. For LNA with TL A and TL C, the simulation results of the individual transmission lines are fitted to transmission line model TLINP in ADS [41]. The LNAs were designed with the ADS transmission line model (TLINP). For TL A and TL C, full-chip EM simulation is very time consuming. And due to shielding there is good isolation between two neighboring lines (below -30 dB for two TL A, with the shielding 20 um apart in simulation), transmission line model already meets the accuracy requirement. For full-chip EM simulation, instability of the LNA with TL B is overestimated in simulation (instability is overestimated, with higher gain in simulation the LNA becomes unstable and therefore in order to achieve stable LNA in simulation, we have to reduce the gain of the LNA) thus the designed gain of the LNA is smaller than LNAs with TL A, TL C.

## 2.9    2-port Measurement Setup For 122 GHz LNA

Figure 2.9 shows the 2-port measurement setup for 122 GHz LNA.

The 4 port network analyzer ZVA67 from Rohde und Schwarz provides RF signals RF/12 and (RF/8-279MHz/8) to frequency extenders Z140. (RF/8-279MHz/8) signal is provided to the two port via a power divider. The 120 GHz RF signal is obtained by the RF signal multiplications in Z140. 120 GHz RF signal is supplied to the device under test through the waveguide transition S-band WR 8-S-band and the probe tip 140-GSG-100-BT-N from Cascade Microtech. The signal paths are symmetrical for the two ports. DC probes provide the DC bias for the chip in on-wafer measurements.
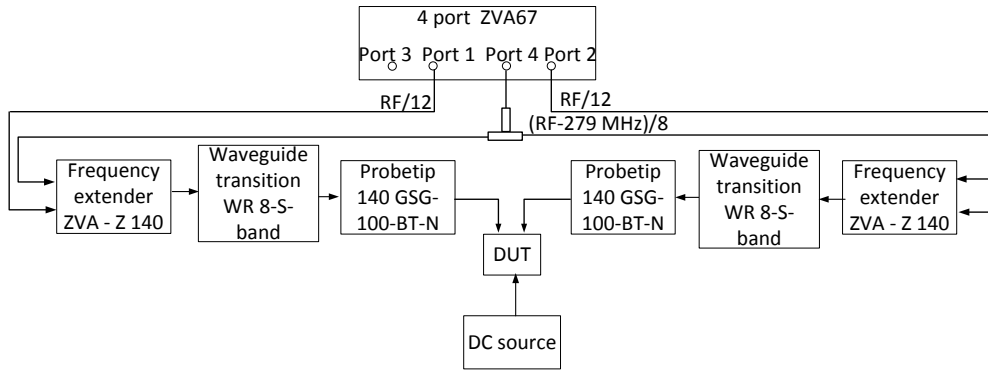


Figure 2.9: measurement setup for 122 GHz LNA

Figure 2.10 shows the S parameter simulation and measurement comparison of the three LNAs in the first design run. The thin line is the simulated result of the LNA's S-parameters, the thick line is the measured result of the LNA's S parameters. Markers are at target frequency 122 GHz. It shows that peak frequency shifts comparing the measurement result with the simulation result. That is because for frequency as high as 122GHz, frequency shift occurs for LNAs even if minor parasitics like pieces of short inter connects, the terminal connections, parasitic bottom capacitor of the MIM capacitor etc. are introduced.

Colum I in Table 2.1 gives a summary of the simulation and measurement numeric comparison of the three LNAs in the first design run. From simulation, gain of the LNA with TL A is larger than LNA with TL C, because Q factor of TL A is larger than TL C. Gain of the LNA with TL B is the smallest due to full-chip EM simulation of the passive structures. The measurement results agree well with the simulation. Although peak frequency shift, the measured peak gains are in good accordance with the simulation results.

Table 2.1: Simulation and measurement performance comparison

of three LNAs

|  | LNA TL A (I) | LNA TL A (II) | LNA TL B (I) | LNA TL C (I) | LNA TL C (II) |
|---|---|---|---|---|---|
| **Peak gain sim.** | 21.7 dB | 19.7 dB | 14.3 dB | 19.7 dB | 18.6 dB |
| **Peak gain meas.** | 18.8 dB | 16.7 dB | 11.1 dB | 15.8 dB | 14.9 dB |
| **Gain@122 GHz meas.** | 14.7 dB | 15.9 dB | 10.5 dB | 14.4 dB | 14.9 dB |
| **NF sim.** | 6.9 dB | 8.4 dB | 8.3 dB | 6.9 dB | 8.3 dB |
| **Peak freq meas.** | 111 GHz | 117 GHz | 127 GHz | 114 GHz | 122 GHz |

In order to get LNAs with frequency centering around 122GHz, LNAs with several frequency versions are redesigned and measured. After measurement, the LNA with least frequency shift is chosen as the final design. In this way with several frequency versions of LNA frequency margin is intended preparatorily between the simulation and measurement results before measurement, and the problem of frequency shift is solved.

Figure 2.11 gives the S parameter simulation and measurement comparison of the three LNAs after redesign. All of the frequency shifts of the three LNAs are within 5 GHz, 4% relatively. Markers are at the peak frequency for simulation and at 122 GHz for measurement. Colum II in Table 2.1 gives the numeric comparison after redesign. LNA with TL B was not redesigned.

Table 2.2: Comparison with state of the art

|  | LNA TL A | LNA in [6] |
|---|---|---|
| **gain @122 GHz** | 15.9 dB | 13.5 dB |
| **NF @peak freq** | 8.4 dB (sim) | 9.6 dB |
| **VCC** | 3.3 V | 3.5 V |
| **ICC** | 10.2 mA | 14.2 mA |

Figure 2.12 gives the S21 comparison of the three LNAs with different transmission lines. Gains are the same as predicted. The gain performance of the modified LNAs with TL A,C are also better than that of the previous 122GHz LNA work with 13.5dB [6] and even with much smaller power. Table 2.2 gives a measurement performance comparison of this work with the data of [6].

In [6], the 122 GHz LNA is biased by short stub transmission lines. This introduces extra loss in short stub transmission lines comparing with biasing with resistors as used in this work.
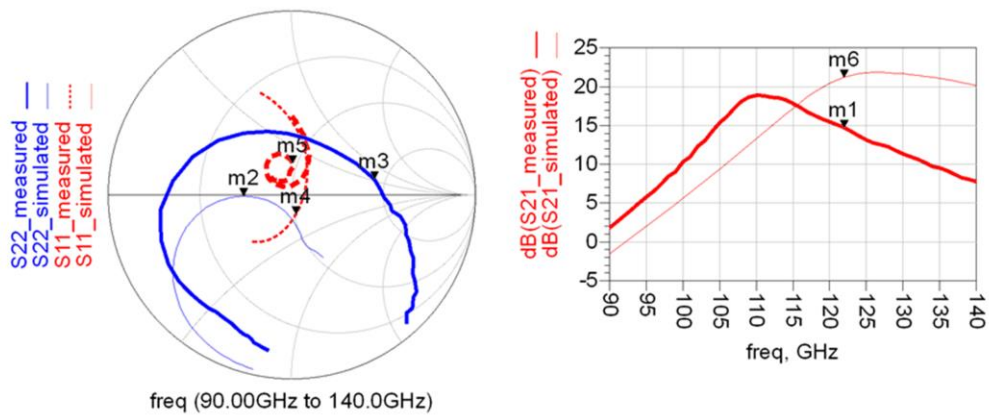
(a) LNA with TL A
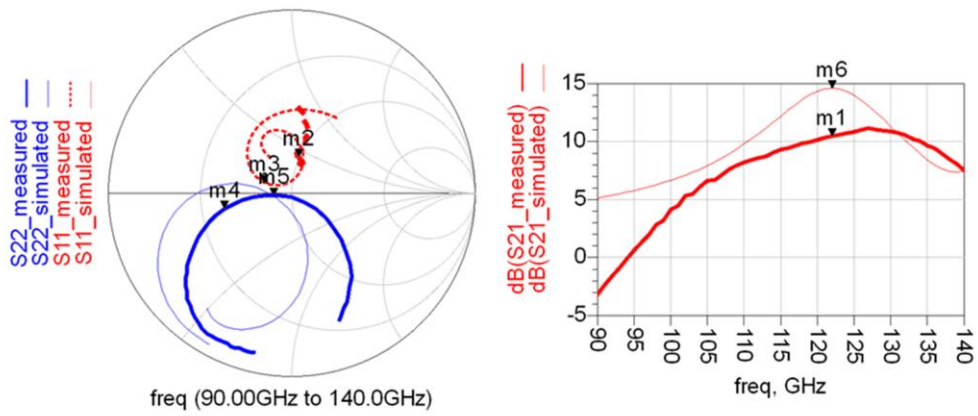


(b) LNA with TL B
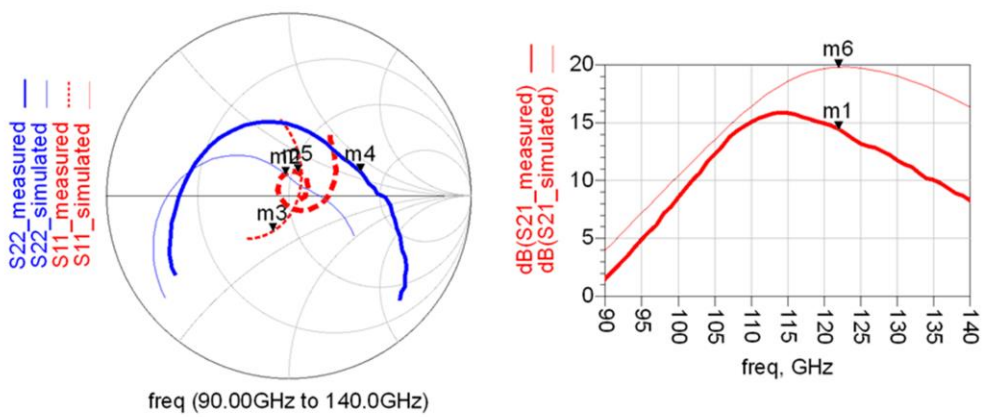


(c) LNA with TL C

Figure 2.10: The S parameter simulation and measurement comparison of the

three LNAs in first run (markers at 122GHz).
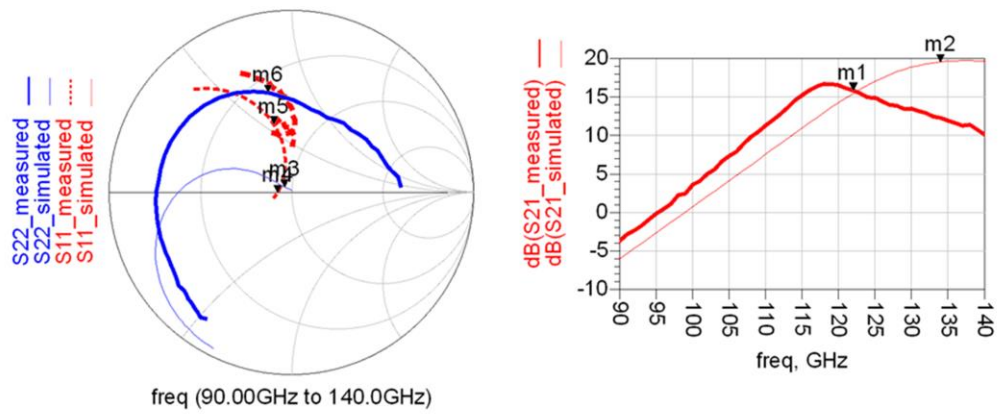
(a) LNA with TL A
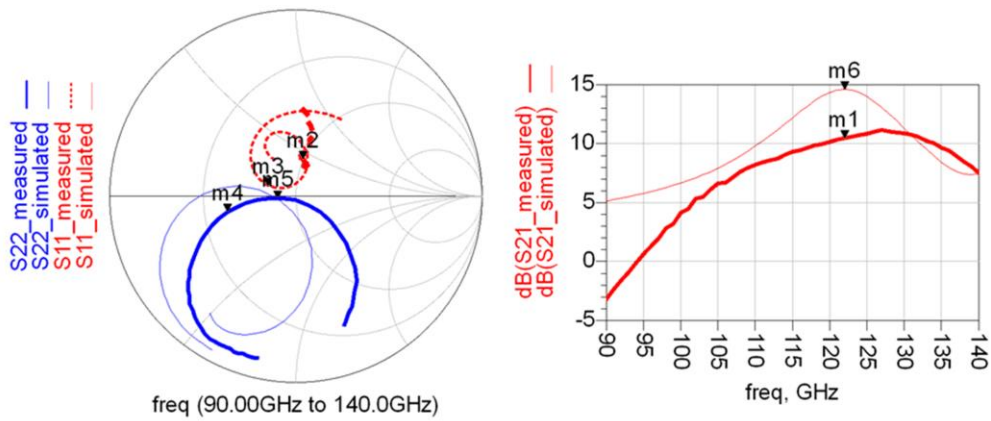


(b) LNA with TL
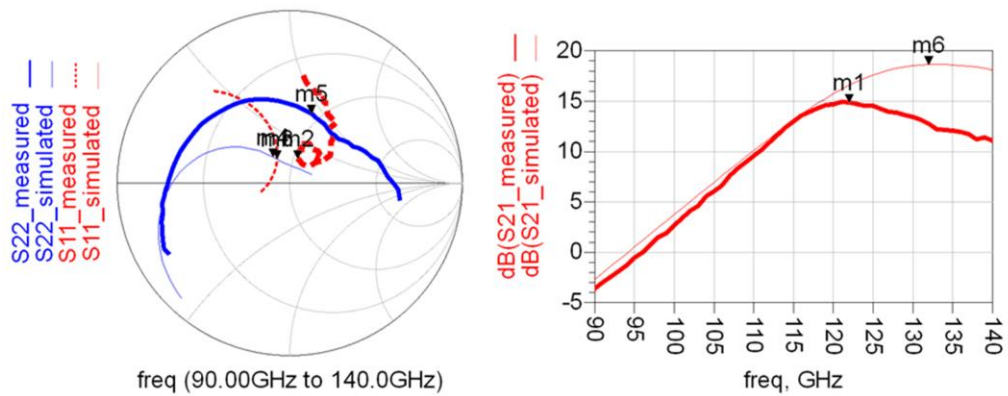


(c) LNA with TL C

Figure 2.11: The S parameter simulation and measurement comparison of the three LNAs after redesign (markers at peak freq for simulation and at 122GHz for measurement).
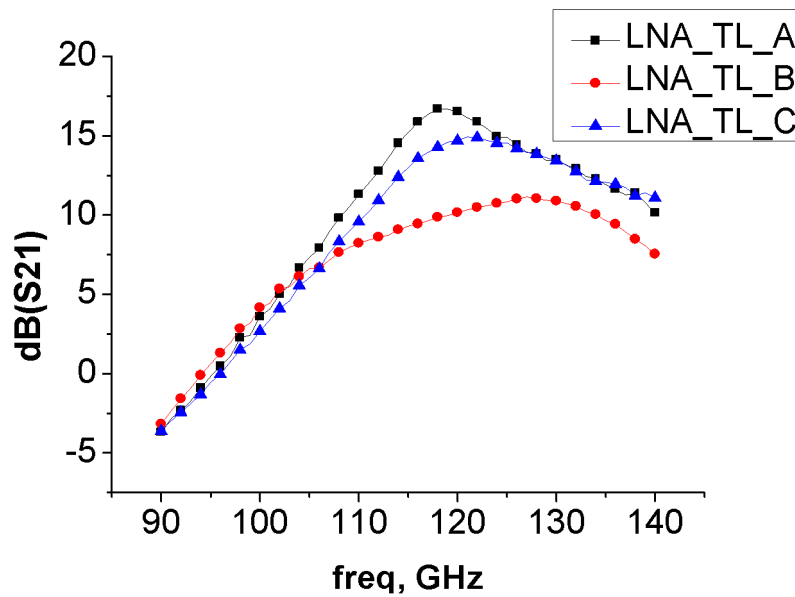
Figure 2.12: The S21 comparison of the three LNAs

with different transmission lines.

## 2.10   Conclusions

Three types of IHP SiGe BiCMOS technologies are introduced. Design model and RF models for passives like MIM capacitors, resistors in the design kit are explored. Bondpad and probe pad design was discussed. The advantages and disadvantages of spiral inductors vs. transmission lines beyond 100 GHz are discussed. Transmission lines are chosen to be utilized as inductors for circuits beyond 100 GHz.

Three types of transmission lines are designed and simulated using an EM field solver. A comparison and discussion of the three types of transmission lines is given.

For an experimental validation of the usefulness of the different transmission line types, 122 GHz LNAs with the three transmission line topologies are designed, measured and compared. Good agreement is achieved between the simulation and measurement results. TL A with highest Q leads to highest LNA gain. Full-chip EM simulation methodology can achieve best accuracy in design. Nevertheless it was shown that a design methodology with conventional transmission line models can already achieve enough accuracy. And given with frequency margin in simulation redesigned LNAs are successfully achieved to solve the problem of frequency shift. This investigation was published in [16]. For the remainder of the work within this thesis TL A was chosen as preferred TL configuration.

# 3 CB LNA design

## 3.1 IEEE two-port noise model

Figure 3.1 shows the IEEE two-port noise model plus signal source, signal impedance, signal source noise, and load impedance.[32] From circuit theory it can be shown that any linear noisy network can be represented by an equivalent circuit consisting of a noiseless two-port with a noise current $\overline{i_n^2}$ and a noise voltage $\overline{v_n^2}$ at the input. We call the noise at the input "input-referred" noise. It is basically the two port output noise divided by the gain of the two-port.

In some text books and applications a noiseless two-port and noise sources at the output are used. This approach has the advantage that it is also a little more intuitive. However input-referred noise allows us to compare the input signal directly with its input-referred noise (=SNR) without knowing the two-port gain. Input-referred noise leads to simplified system and circuit analysis and is a classical model for noise analysis.

Figure 3.2 shows IEEE two-port noise model with alternative representation of the source: Norton equivalent for signal source and signal source noise current. This is equivalent with circuit in figure 3.1. Using admittances for the source gives us a little simpler equation for the NF.
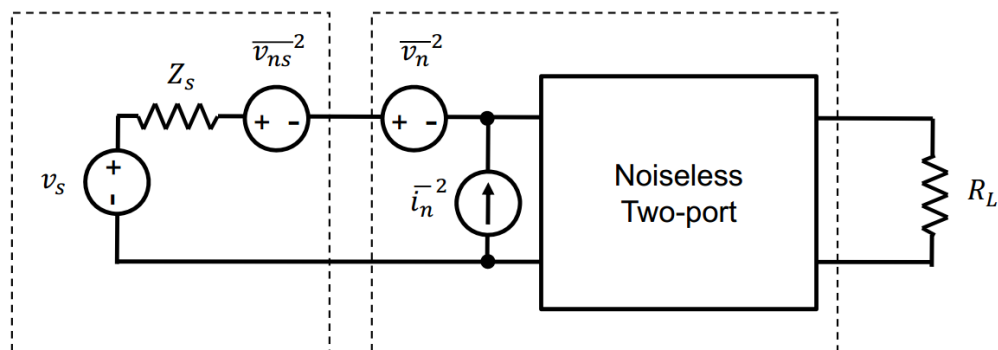


Figure 3.1 IEEE two-port noise model with signal source and load impedance, picture taken from [32]
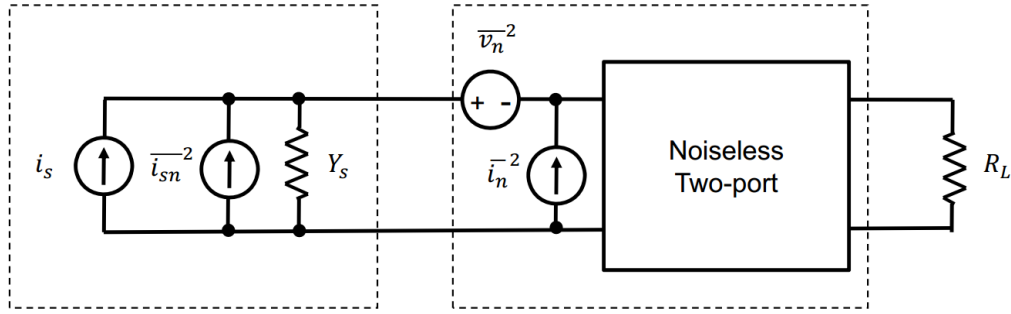
Figure 3.2 IEEE two-port noise model with Norton equivalent for signal source, picture taken from [32]

Using the above circuit in figure 3.2 the 2-port NF is derived as in equation 3.1 [42]:

$$NF = NF_{min} + \frac{R_n}{G_s} * \left| Y_s - Y_{opt} \right| \tag{3.1}$$

With $NF_{min}$ being the lowest possible NF of the noisy two-port, $R_n$ being the equivalent noise resistance of the two-port $R_n = \dfrac{\overline{v_n^2}}{4kT\Delta f}$. $Y_{opt} = G_{opt} + jB_{opt}$ being the complex noise admittance of the two-port. $Y_s = G_s + jB_s$ being the complex signal source admittance.

If $Y_s = Y_{opt}$, signal source and amplifier (2-port) are "noise matched". For noise matched circuits we get $NF = NF_{min}$. $NF_{min}$, $R_n$, $Y_{opt}$ are properties of the noisy 2-port while $Y_s$ pertains to the signal source. $NF_{min}$ is the lowest possible NF of the amplifier, which should be as near as possible to the transistor's $NF_{min}$. Noise resistance $R_n = \dfrac{\overline{v_n^2}}{4kT\Delta f}$ is a measure of the sensitivity of NF to deviations from noise-matching conditions, e.g. due to device parameter variations.

NF circle is a circle in the complex plane which has the equation $\left| X - X_0 \right|^2 = r^2$ with X, $X_0$ being complex variables, $X_0$ is the origin and r is the radius of the circle. Hence $\left| Y - Y_{opt} \right|^2 = const.$ represent circles in the admittance plane.
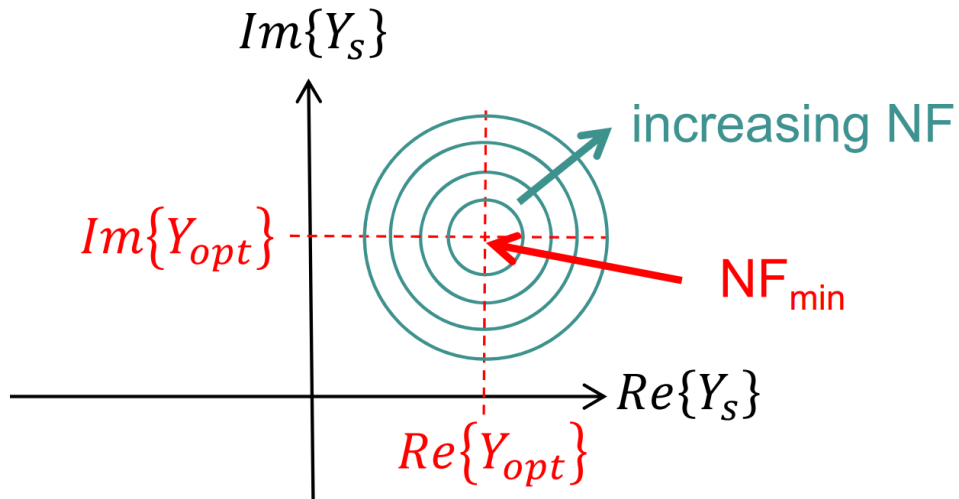
Figure 3.3 NF   circles in admittance plane, picture taken from [32]

The concentric circles represent $Y_s$ for which NF is constant, as shown in figure 3.3. Each circle represents a certain NF. The larger the circle, the larger is NF. For $Y_s = Y_{opt}$, NF $= NF_{min}$   (center of the circles).

## 3.2    Relationship between noise parameter and noise correlation chain matrix $C_A$

The definition of noise correlation chain matrix is as in equation 3.2:

$$C_A = \begin{bmatrix} \overline{v_A v_A^*} & \overline{v_A i_A^*} \\ \overline{i_A v_A^*} & \overline{i_A i_A^*} \end{bmatrix}$$

(3.2)

Using the noise correlation chain matrix representation, the correlated noise voltage and current are located at the input of the circuit, supporting a direct relation with the four noise parameters [43].

The ABCD correlation matrix $[C_A]$ can now be written in terms of the noise figure parameters as,

$$C_A = \begin{bmatrix} \overline{v_A v_A^*} & \overline{v_A i_A^*} \\ \overline{i_A v_A^*} & \overline{i_A i_A^*} \end{bmatrix} = \begin{bmatrix} c_{uu^*} & c_{ui^*} \\ c_{u^*i} & c_{ii^*} \end{bmatrix} = 2kT \begin{bmatrix} R_n & \dfrac{NF_{min}-1}{2} - R_n Y_{opt}^* \\ \dfrac{NF_{min}-1}{2} - R_n Y_{opt} & R_n \left| Y_{opt} \right|^2 \end{bmatrix}$$

(3.3)

Or vice versa,

The optimum noise admittance:

$$Y_{opt} = \sqrt{\frac{c_{ii^*}}{c_{uu^*}} - \left[ \mathrm{Im}\left( \frac{c_{ui^*}}{c_{uu^*}} \right) \right]^2} + j\,\mathrm{Im}\left( \frac{c_{ui^*}}{c_{uu^*}} \right) \tag{3.4}$$

The minimum noise figure:

$$NF_{\min} = 1 + \frac{c_{ui^*} + c_{uu^*} Y_{opt}^*}{kT} \tag{3.5}$$

The noise resistance:

$$R_n = \frac{c_{uu^*}}{2kT} \tag{3.6}$$

The IEEE noise model can be used for the noise analysis of complete amplifiers but also for just the HBT alone as done e.g. in [44]. A noise analysis of HBTs yields as NF$_{\min}$ of the transistor [44]:

$$NF_{\min} = 1 + \frac{1}{\beta} + \sqrt{2 g_m r_b} \sqrt{\frac{1}{\beta} + (\frac{f}{f_T})^2} \tag{3.7}$$

when $g_m r_b \gg \frac{1}{2}$. $\beta$ is current gain of the transistor, $g_m$ is transconductance, $r_b$ is base resistance, $f_T$ is transit frequency.

The two terms inside the second square root of equation 3.7 become equal at corner frequency $f = \frac{f_T}{\sqrt{\beta}}$, which defines a transition of NF from a white noise behavior (independent of frequency) to a 10-dB/decade increase as the frequency increases. In other words, NF$_{\min}$ degrades as 10-dB/decade with increasing frequency when frequency is larger than corner frequency $f = \frac{f_T}{\sqrt{\beta}}$.

$$g_m = \frac{qI_C}{kT} \tag{3.8}$$

$$f_T = \frac{g_m}{2\pi C_i} \tag{3.9}$$

$$C_i = C_{be} + C_{bc} \tag{3.10}$$

$$NF_{\min} = 1 + \frac{1}{\beta} + \sqrt{\frac{2 g_m r_b}{\beta} + 2 r_b \frac{f^2}{g_m} 4\pi^2 C_i^2} \tag{3.11}$$

$C_{be}$ is base emitter capacitance, $C_{bc}$ is base collector capacitance. Substituting equation 3.8-3.10 into equation 3.7, equation 3.11 is obtained. Assume parameters $\beta, r_b, C_i, f$ are constant, $g_m$ is proportional to collector current

$I_C$ , according to equation 3.11, $NF_{\min}$ has a minimum value when $g_m = 2\pi f C_i \sqrt{\beta}$ . $g_m$ is proportional to $I_C$, therefore $NF_{\min}$ decreases when collector current density increases and after reaching a minimum value, $NF_{\min}$ increases when collector current increases.

According to equation 3.7, at low frequencies beta dominates the NF. With increasing frequency with f being beyond $f_T/\sqrt{\beta}$ small $r_b$ becomes important, too.

According to equation 3.9, in order to obtain peak $f_T$, high collector current density is applied in order to obtain high $g_m$. Collector current density for peak $f_T$ is higher than the collector current density for minimum $NF_{\min}$ .

For extreme high-frequency LNA design, in order for the transistors to work at extreme high-frequency, transistors are biased close to the peak $f_T$ .

## 3.3    Comparison of Common Base (CB) Stage With Other Circuit Topologies

Various LNAs with different topologies like common emitter or cascode are reported. In [5] using SiGe technology, a differential 3 stage common emitter  LNA at 60 GHz with 18 dB gain and 22 GHz 3dB bandwidth is reported. With differential topology the circuit can work robustly to bondwire inductances and variations of the on-chip ground potential are less harmful. In [6] a two stage cascode SiGe LNA with 13.5 dB gain and a noise figure of 9.6 dB at 122 GHz is reported. The cascode configuration is chosen for its high gain, high isolation and wide bandwidth.

For frequency as high as 245 GHz, gain achieved by each stage in case of common emitter topology is reduced dramatically compared to 60 GHz. Cascode topology although still provide high gain nevertheless the noise figure degrades with the increase of the operating frequency. In order to obtain high gain and while maintaining low noise figure for 245 GHz, this work investigates another topology : common base and presents a four stage LNAs with high gain and low noise figure.

Table 3.1: A comparison of three topologies

|  | CE | CB(1 stage) | CB (2 stage) | cascode |
|---|---|---|---|---|
| **Gain** | 1.9 dB | 3.2 dB | 6.2 dB | 5.2 dB |
| **NFmin** | 8.5 dB | 7.9 dB | 9.8 dB | 12.1 dB |
| **NF** | 8.7 dB | 9.4 dB | 10.8 dB | 12.1 dB |
| **Power** | 7mA*1.5V | 7 mA* 2V | 14 mA*2V | 7 mA*3.5 V |

Common base topology (CB) is chosen for each stage for its wide bandwidth, high gain, high isolation for the design frequency[19]. Comparing common base stage with common emitter stage (CE), common-base stage does not contain a feedback capacitance from collector to emitter to cause the Miller effect. As a consequence, the bandwidth of the common base stage is much higher than common emitter stage. For circuit design up to the frequency of 245GHz, common base stage could achieve higher gain for each stage. Comparing common base stage with cascode topology, with comparable gain and comparable power, the noise figure of the common base topology is smaller than cascode topology in simulation. Table 3.1 shows a summary of simulation comparison between the three different topologies with transistors of the same size biased at the same collector current density at 245 GHz. The collector current density is chosen so that the transistors are biased close to the peak $f_T$.

From table 3.1, the common base topology has much better gain performance than common emitter topology per stage. Comparing common base of 2 stages with cascode topology, gain of common base topology is a little higher than cascode, and noise figure is 1dB less than that of cascode topology. Power dissipations of the two are comparable.

Figure 3.4 shows the schematic of the four-stage CB LNA . With resistor ladder R1 and R2, pad $V_{cb}$ provides the base bias for the common base transistor. The transmission lines $TL_{sh}$ not only provide the dc ground for the emitters of the transistors but as well work together with the $TL_{ser}$ and Metal-Insulator-Metal (MIM) capacitors C1,C2,C3,C4,C5 to form the input, output, and inter-stage impedance matching network. Transmission lines $TL_{load}$ are inductive loads for each common base stage. $C_{byp}$ provides the ac ground for the base connection and the dc supply. Besides, resistors $R_{byp}$ and $C_{byp}$ at the collector terminal form a low pass filter for the dc supply VCC, which helps to improve the isolation between CB stages. Bondpad capacitance $C_{bondpad}$ are also included in both the input and output matching networks and the input and output matching impedance $Z_{in}$ and $Z_{out}$ are 50 Ohm. $Z_{in}$ and $Z_{out}$ are not part of the circuit but represent the (ideal) impedance of the signal source (i.e. VNA port plus cable plus probe).
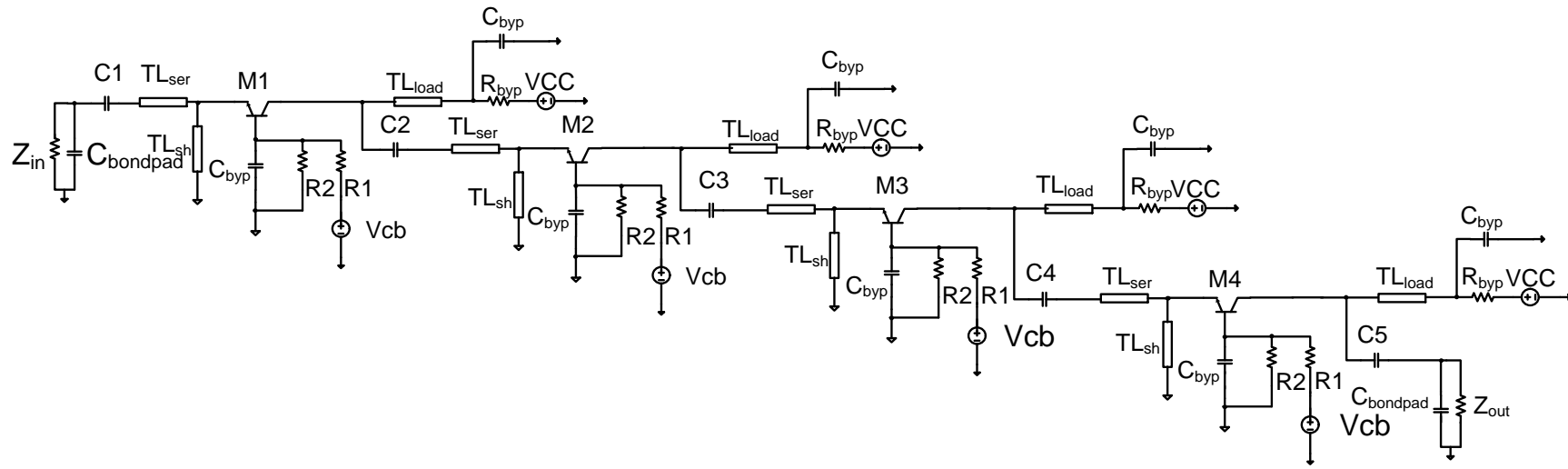
Figure 3.4: schematic of the 4 stage common base LNA

## 3.4    CB LNA simulation and measurement results in 0.25 um SG25 H1 BiCMOS (DotFive) technology

The design was carried out using the transistor model of IHP for its experimental 0.25 um SG25 H1 BiCMOS (DotFive) technology. The technology has 5 metal layers. The 5 metal layers include 3 aluminum metal layers and 2 top-metal layers with 2um and 3um thickness respectively. Low-loss transmission lines could be designed with the two thick top-metal layers. The $f_t$ and $f_{max}$ of the experimental transistor are reported to be 300 GHz and 500 GHz respectively [20].

All of the transmission lines were simulated with 2.5D planar EM-simulator (Momentum). The simulation results were fitted to transmission line model TLINP. And then TLINP is utilized in the design.

The chip photo of the LNA is shown in figure 3.5. The chip size is 0.42*0.46 mm2, GSG input and output bondpads with 100um pitch length are utilized for on wafer measurement. Metal1 shielding is adopted for the pad design in order to prevent substrate loss and obtain high Q pad capacitance. On the left and right side are the input and output bondpads. On the top are the VCC and $V_{cb}$ pads. Channel stop implant was blocked at critical places like input, output pad, transmission lines, long inter connects etc., in order to reduce the ohmic loss. Large areas of decoupling MIM capacitors are also included in the chip between the supply and the ground.
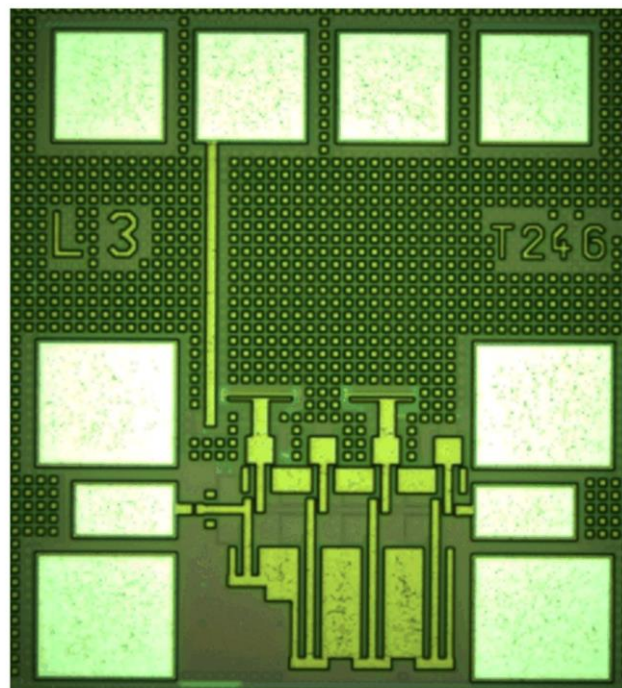


Figure 3.5: chip photo of the 4 stage common base LNA

For frequency as high as 245 GHz, frequency shift occurs for LNAs even if minor parasitics like pieces of short inter- connects, the terminal connections, parasitic bottom capacitor of the MIM capacitor etc. are introduced. Thus in order to give some frequency margin for measurement, two LNAs peaking at 245 GHz and at 265 GHz are designed. Figure 3.6 shows the S parameter simulation of the two LNAs. The two LNAs are both input and output matched to 50 Ohms. They can achieve 13 dB and 10 dB gain, 12 dB and 14 dB noise figure respectively at the designed frequency. Unconditional stability of the LNA is verified from dc to 300GHz.

Figure 3.7 shows the measurement result of the 265 GHz LNA. During the measurement with the original bias points in simulation, the LNA behaves unstable, and by reducing the bias voltage at the base terminal $V_{cb}$ from 1.8 V to 1.55 V, the LNA becomes stable again. In order to give complete information, measurement results of two typical bias points are given. LNA with $V_{cb}$ of 1.65V is not stable, with S22@212GHz above zero, it has power dissipation of 29mA*2V. LNA with $V_{cb}$ of 1.55V is stable, it has a power dissipation of 14mA*2V. For the latter, the peak frequency shifts to 235 GHz. It has 12 dB gain at 245 GHz , and a 3 dB bandwidth of 26 GHz. Besides that, because the base is biased by resistor ladder, the LNA performance is sensitive to $V_{cb}$. Nevertheless this could be improved by more accurate transistor biasing circuits. Due to the limitation of the measurement equipment, the noise figure was not measured.

The difference between the simulation and measurement is assumed to be due to the parasitic inductance between base terminal and the ground. The inductance could come from the connection between base terminal and bypass capacitor (ac ground) or the unideal metal ground plane and it is in the range of 1-5 pH. Nevertheless, at such high frequency 245 GHz , already such low inductance affects the LNA performance a lot. Figure 3.8 shows the 3D view of base-MIM capacitor connection. Bottom blue layer is metal 1, which is connected to base terminal of transistor, while top grey layer is TM1, which is connected to the two top plate of MIM capacitors at base terminal.

An analysis of the effect of the small parasitic inductance at the common base is given below. In 3.12 $\omega_T$ is the cut off frequency of the transistor, $g_m$ is the transconductance of the transistor and $C_\pi$ is the base emitter capacitance. The impedance at the base terminal $Z_B$ can be expressed by the parasitic inductance $L_P$ as shown in 3.13. According to $\beta$ -transformation, from the emitter terminal, the impedance $Z_E$ can be expressed by the base terminal impedance $Z_B$ reflected back to the emitter as shown in 3.14; $\beta$ (j$\omega$) is the current gain of the transistor.[21] Inserting 3.13 into 3.14, 3.15 is obtained. From 3.15, the parasitic inductance at the base terminal introduces negative resistance at the

emitter terminal. The circuit is operating near $\omega_T$, $\omega \approx \omega_T$, therefore 3.16 is obtained.

$$\omega_T = \frac{g_m}{C_\pi} \tag{3.12}$$

$$Z_B = j\omega L_P \tag{3.13}$$

$$Z_E \approx \frac{Z_B}{\beta(j\omega) + 1}$$
$$\approx \frac{Z_B}{\dfrac{\omega_T}{j\omega} + 1} \tag{3.14}$$

$$Z_E = \frac{(j\omega - \omega_T)L_P}{(\dfrac{\omega_T}{\omega}) + 1} \tag{3.15}$$

$$Z_E \approx \frac{(j\omega - \omega_T)L_P}{2} \tag{3.16}$$

From 3.16, the negative resistance is proportional to $\omega_T$. $\omega_T$ is proportional to $g_m$, which is proportional to the collector current. The collector current is determined by the base emitter bias $V_{be}$. Thus by reducing base emitter bias voltage $V_{be}$, collector current is reduced, $\omega_T$ is reduced and the negative resistance at the emitter can be reduced. In this way, the stability of the LNA is improved by decreasing the base terminal bias voltage.

In order to verify the explanation, an estimated parasitic inductance of 4pH is inserted between the base terminal and bypass capacitors (ac ground) for the 265 GHz LNA, and biased with the measured bias voltage value. S parameter simulation results of the LNA including the parasitic inductance are shown in figure 3.9. In comparison the measurement result is also plotted. The peak frequency is shifted to around 245 GHz due to the parasitic inductance, and the LNA could achieve higher gain even with lower collector current density. The simulation confirms the measurement result. Unconditional stability is verified across the 2 GHz to 300 GHz. Nevertheless, between dc and 2 GHz conditional stability is verified for specific frequency range. Furthermore, with reduced bias voltage value, taking advantage of the parasitic inductance, the LNA can have even smaller simulated noise figure, which is only 11 dB at 245 GHz. Table 3.2 shows a comparison of the simulation and measurement result of the LNA. In table 3.2, NF is very close to $NF_{min}$ in simulation. Excellent noise matching is obtained when impedance matching is realized at design frequency.

Table 3.2: A comparison of simulation and measurement results

|  | simulation @265GHz | simulation with parasitic inductance | measurement |
|---|---|---|---|
| **S21** | 10 dB | 14.1 dB | 12 dB |
| **Vcb** | 1.8 V | 1.55 V | 1.55 V |
| **NF** | 13.7 dB | 11.3 dB | - |
| **NFmin** | 13.1 dB | 11.2 dB | - |
| **Power** | 44mA*2V | 16mA*2V | 14mA*2V |

In a word, a four stage common base 245 GHz LNA is designed and measured in 0.25 um SG25 H1 BiCMOS (DotFive) technology. A four stage common base 245 GHz LNA with 12 dB gain, 25 GHz 3-dB bandwidth, and a small power dissipation of 28 mW is demonstrated. The base bias voltage decreased to reduce current density compared with that in simulation. This phenomenon is explained and verified well by including a parasitic inductance between the base terminal and ground. Measurement results agree well with the simulation.

## 3.5    Modified CB LNA in SG13G2 BiCMOS technology

Figure 3.10 shows the schematic of one stage of the four-stage modified CB LNA in SG13G2 BiCMOS technology. The technology has the same metal layers as in SG13S technology but with different transistors. The $f_T$ and $f_{max}$ of the transistor are 300 GHz and 500 GHz, respectively. In Dotfive technology, $V_{cb}$ provides the base bias for the common base transistor through resistor ladder R1 and R2. In SG13G2 BiCMOS technology, the bias circuit is modified as shown in figure 3.10. Diode-connected transistor biasing is adopted in order to realize more accurate bias. Figure 3.11 presents LNA sensitivity vs base bias $V_{cb}$ in order to give a comparison. S21 increases from 9.5 dB to 11 dB when $V_{CB}$ changes from 1.9 V to 2.1 V. Comparing the LNA measurements in figure 3.8, the LNA becomes much less sensitive to $V_{CB}$ with the diode-connected bias circuit.

In figure 3.10, transistor Q0 is biased at close to peak $f_T$ collector current density in order to achieve high speed for Q0. $TL_{sh}$ provide the dc ground for the emitters of the transistors and, with the $TL_{ser}$ and Metal-Insulator-Metal (MIM) capacitors Cn (n=1-4), form the input and inter-stage impedance matching network, where n presents the number of the stage in the four-stage CB

LNA. Transmission lines $TL_{load}$ represent inductive loads for each common base stage. $C_{byp}$ provides the ac ground for the base connection and the dc supply.

Figure 3.12 shows S-parameter measurement results of standalone CB LNA biased with $V_{cb}$ of 2.1V. S21 of the CB LNA has a 3-dB bandwidth extending from 237 GHz to 261 GHz. A gain of 11 dB is achieved at 243 GHz. S11 and S22 are below -4 dB at 245 GHz. The simulated NF is 12 dB.

## 3.6    2-port measurement setup for 245 GHz LNA

Figure 3.13 shows the measurement setup for 245 GHz LNA.

4 port network analyzer ZVA67 provides RF signals RF/18 and (RF/16-279MHz/16) to frequency extender Z325. RF signal (RF/16-279MHz/16) is provided through power divider. 245 GHz RF signal is obtained by the RF signal multiplications in Z325. 245 GHz RF signal is supplied to device under test through the waveguide transition S-band WR 3.4-S-band and probe tip 325-GSG-60-BT. The signal paths are symmetrical for the two ports. DC probes MCW-14 Multi-Contact Wedge provide the DC bias for the chip in on-wafer measurements.
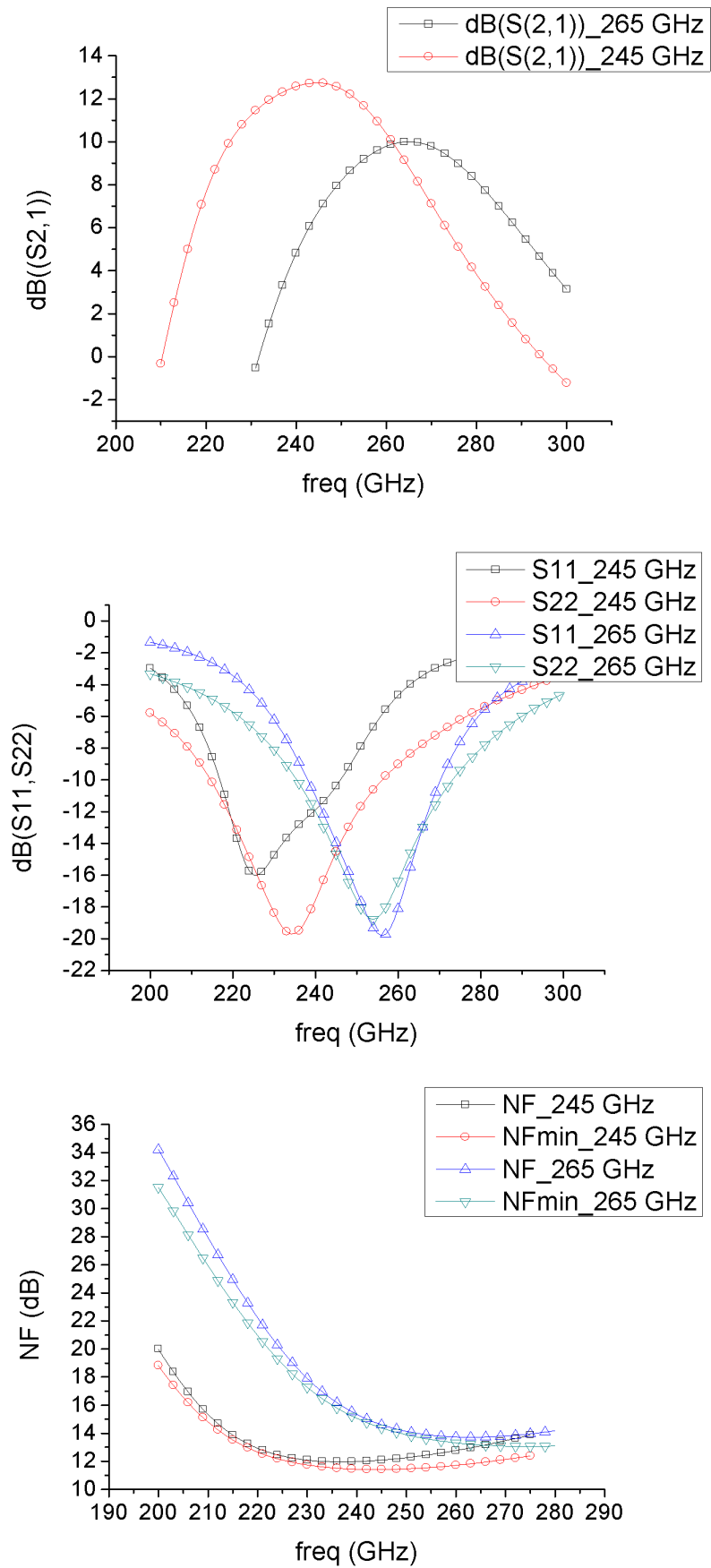
Figure 3.6: Simulation results of the 245 GHz and 265 GHz LNAs
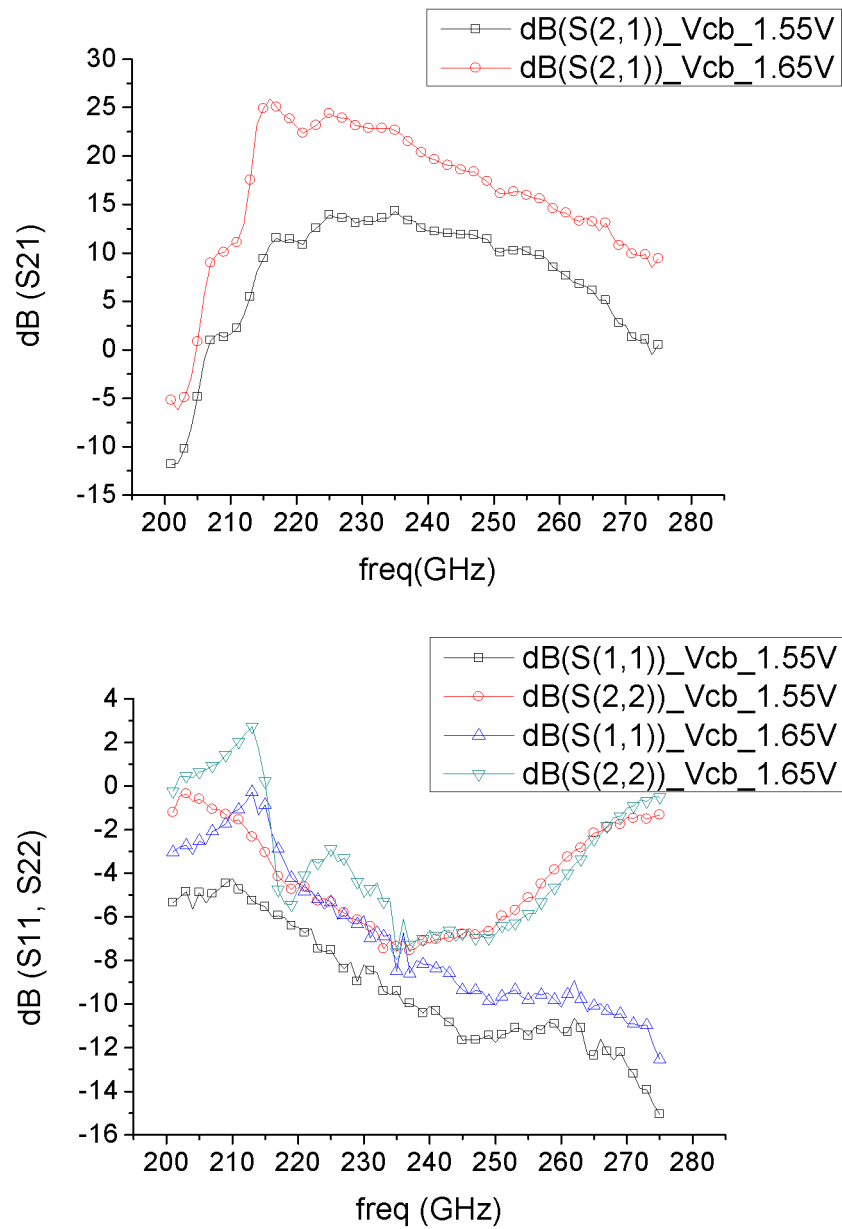
Figure 3.7: Measured results of the 265 GHz LNA with different current density: 29mA*2V ($V_{cb}$: 1.65V) and 14mA*2V ($V_{cb}$: 1.55V)

Figure 3.8 3D view of base-MIM capacitors connection

Figure 3.9: Simulation and measurement results when parasitic inductance at base terminal is included.

Figure 3.10: Schematic of the one stage of modified CB LNA



Figure 3.11: S21 sensitivity vs base bias Vcb in SG13G2 BiCMOS technology.



Figure 3.12: S-parameter measurement results of modified CB LNA.

Figure 3.13: measurement setup for 245 GHz LNA

# 4 Subharmonic Mixer Design

## 4.1 Subharmonic Mixers

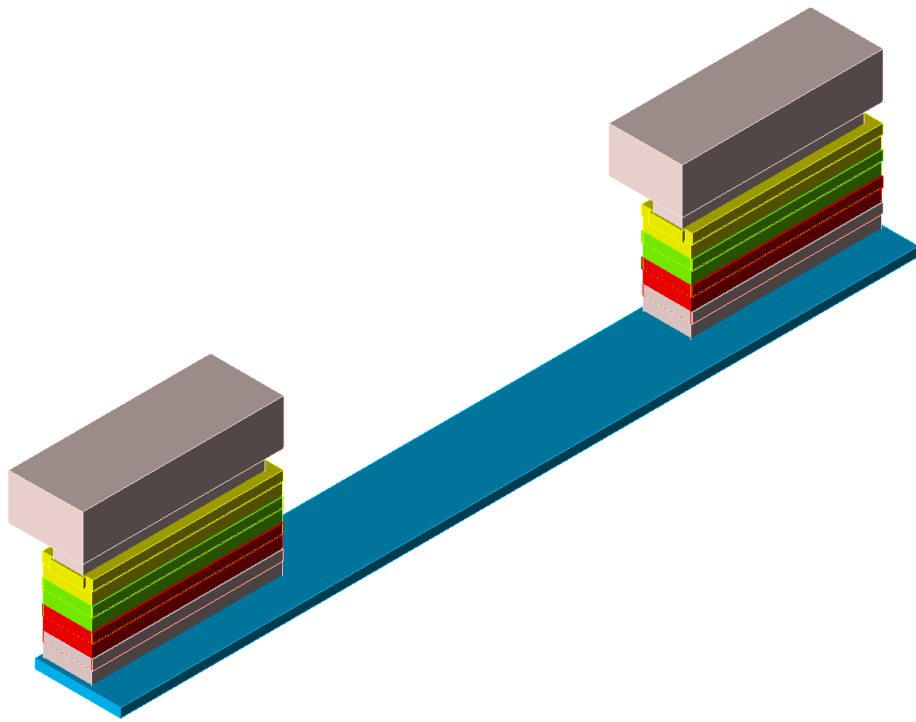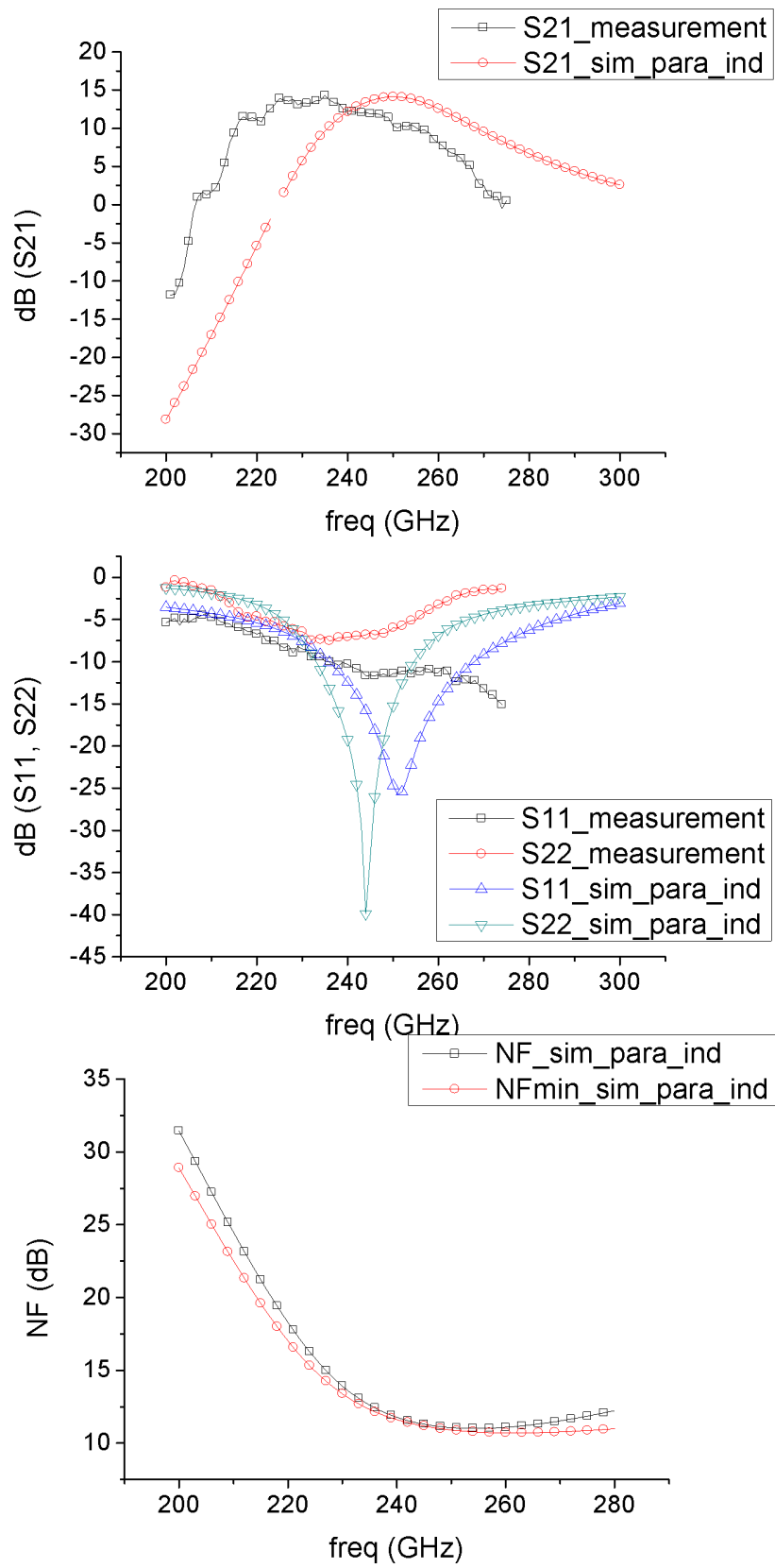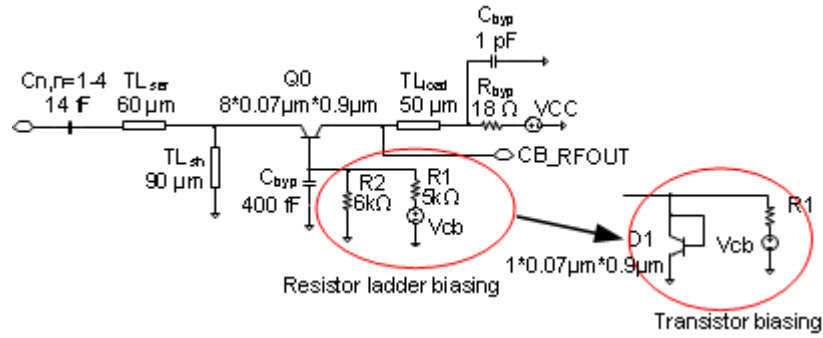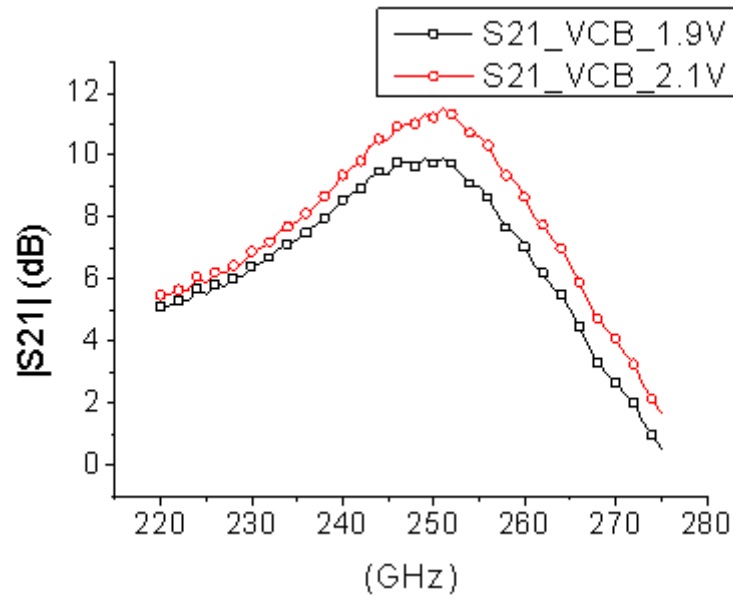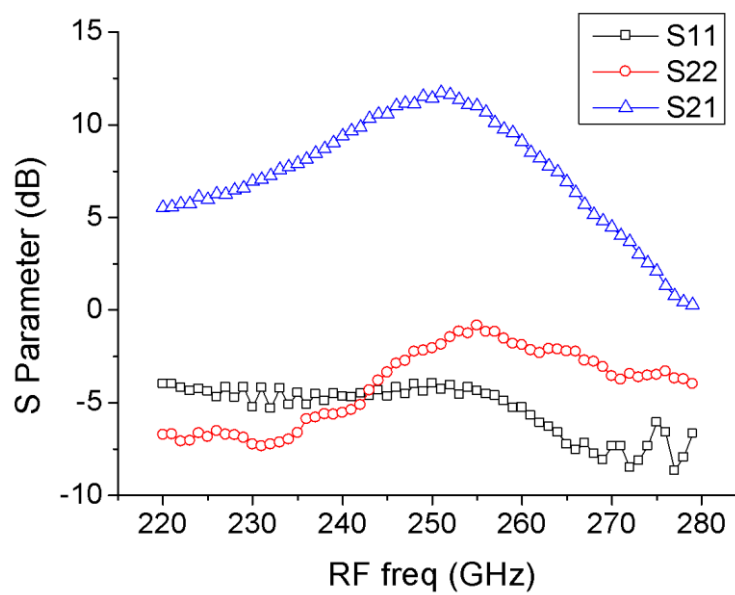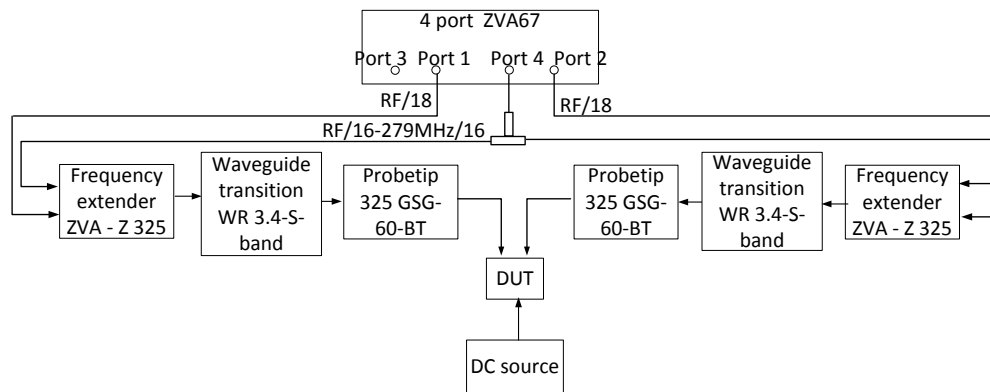In a subharmonic mixer (SHM), the LO frequency is internally multiplied, thus producing mixing components from the RF frequency and an integer multiple of the LO frequency. If $f_{RF}$ is the RF input frequency and $f_{LO}$ is the LO input frequency then the output signals will have frequency $f_{IF} = f_{RF} \pm n f_{LO}$, where n is the order of the subharmonic mixer. When n = 2 the circuit will be referred to as a 2× subharmonic mixer and when n = 4 the circuit will be called a 4× subharmonic mixer. [46]

## 4.2 Topologies of Subharmonic Mixers

In RFIC design, Gilbert-cell is one of the most popular balanced mixer design. An active subharmonic mixer can be achieved by extending the Gilbert-cell with a further line of LO switching transistors yielding in a stacked Gilbert-cell topology. In [13], a differential 2$^{nd}$ active subharmonic mixer (SHM) based on two stacked switching quads with conversion gain of 21 dB at 122 GHz and noise figure of 21 dB is reported. In [4], a differential 2$^{nd}$ subharmonic receiver utilizing 2$^{nd}$ active subharmonic mixer is presented. The receiver has conversion gain of 16 dB at 220 GHz and an NF of 16 dB. Figure 4.1 is schematic of an active subharmonic mixer and its LO switching cycles [8]. Subharmonic mixing can be obtained in this topology by feeding the RF input signal to the first port and driving the two remaining ports with the in-phase and quadrature components of the LO signal according to the trigonometric identity [4].

$$V_{out} = A * V_{RF}(t) * \sin(\omega t) * \cos(\omega t) = \frac{A}{2} * V_{RF}(t) * \sin(2\omega t) \qquad (4.1)$$

Figure 4.2 shows a simplified schematic of a transconductance mixer. In transconductance mixing, the time-varying transconductance is the dominant contributor to frequency conversion. The LO is a large signal and its voltage across the base and emitter junctions create a time-varying transconductance $G_m(t)$. In general, $G_m(t)$ is periodic but not a sinusoidal signal and can be represented as a Fourier series 4.2.

$$G_m(t) = G_{m0} + G_{m1} \cos(\omega_{LO}t) + G_{m2} \cos(2\omega_{LO}t) + G_{m3} \cos(3\omega_{LO}t) + ... \qquad (4.2)$$

The collector current $i_C$ is the product of the $G_m(t)$ and input voltage $V_{BIAS}+V_{RF}cos(\omega_{RF}t)$. The output current consists of many mixing products. $G_{m1}V_{RF}2cos[(\omega_{RF}-\omega_{LO})t]$ is the fundamental mixing term, which could be utilized as fundamental frequency translation. In [9], it is the 2nd mixing term $G_{m2}V_{RF}2cos[(\omega_{RF}-2\omega_{LO})t]$ that generates the desired 2nd index mixing product. In [10], it is the 4th mixing term $G_{m4}V_{RF}2cos[(\omega_{RF}-4\omega_{LO})t]$ that generates the 4th index subharmonic mixing product. The 2nd or 4th mixing term should be maximized for higher conversion gain. In principle, the 2nd and 4th harmonic signal is a function of conduction duty cycle and its optimum value can be obtained when the transistor is biased close to its turn-on point.

In [9] 2nd transconductance subharmonic balanced mixers with 0.7 dB conversion gain at 77 GHz are demonstrated. In [10] a 4th transconductance SHM at 650 GHz with -13 dB conversion gain and 42 dB noise figure is presented. In [11] a single-ended 4th passive anti-parallel-diode-pair (APDP) GaAs monolithic subharmonic mixer with a maximum conversion loss of 13.2 d dB is achieved at 60 GHz. Figure 4.3 shows a schematic of the anti-parallel-diode-pair. In a subharmonic mixer using APDP, even mixing components, e.g. $2f_{LO}$, $4f_{LO}$ and $f_{RF}-f_{LO}$, flow within the diode loop. Only odd mixing components, e.g. $f_{RF}-2f_{LO}$ and $3f_{LO}$ are outputted. Therefore, the IF frequency $f_{IF}$ can be expressed as follows: 4.3

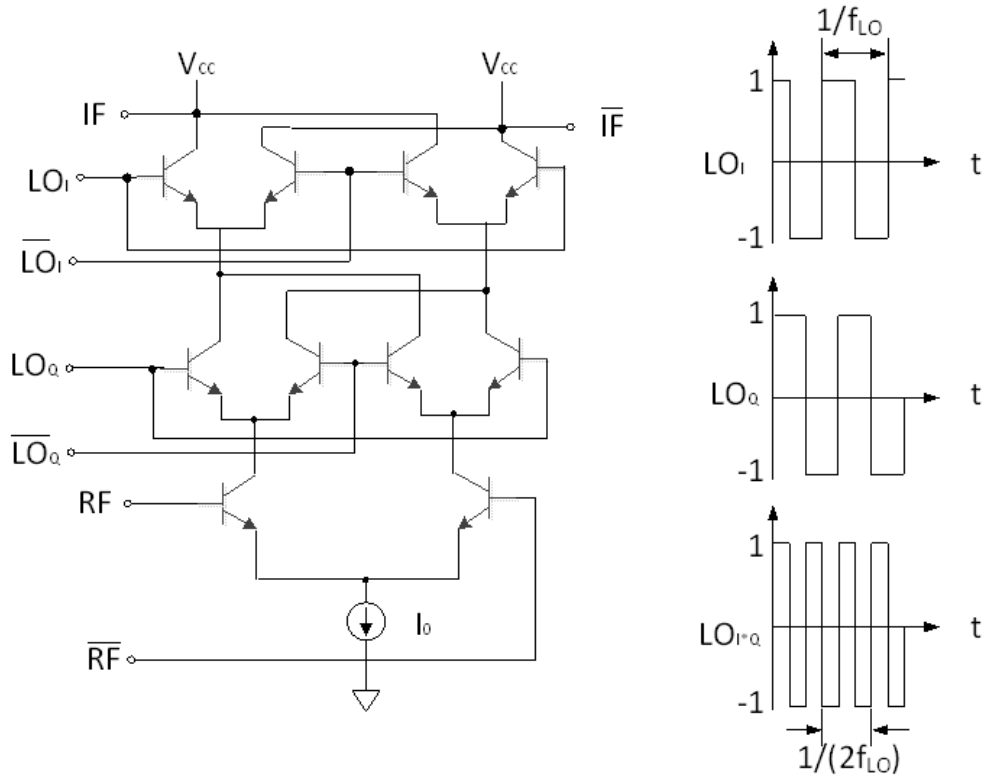$$f_{IF} =| f_{RF} - 2nf_{LO} | (n:\text{int}eger) \tag{4.3}$$



Figure 4.1: Schematic and LO-switching-cycles of active subharmonic mixer
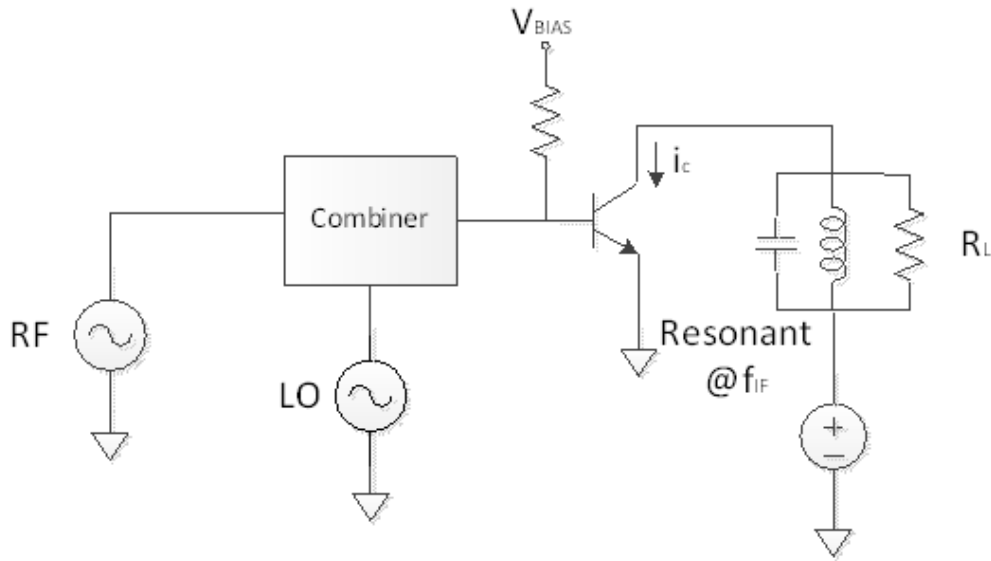
Figure 4.2: Simplified schematic of a transconductance mixer

For $2^{nd}$ passive mixer, n = 1 is adopted. Therefore 120 GHz signals are utilized as LO signals for the $2^{nd}$ APDP passive SHM.

The above mentioned three kinds of subharmonic mixers are the most frequently utilized SHM topologies. The topology of active subharmonic mixer is frequently adopted in recent reports like [13], [4], [8] in SiGe. This work mainly investigates in topologies of the transconductance SHM and APDP SHM, and compares the performance.



APDP
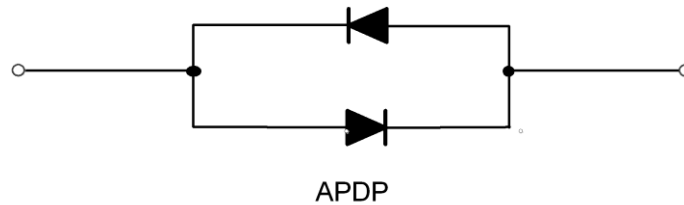
Figure 4.3: Schematic of an anti-parallel-diode-pair

Comparing active SHM based on stacked switching cores with transconductnce SHMs, active SHM does not behave like switches at frequencies near the $f_T$ of the transistors while transconductance SHMs still function well even for frequencies beyond $f_T$(or $f_{max}$) [10]. Comparing passive SHM with SHMs based on active SHM, passive SHM dissipates no DC power. Based on all these above mentioned considerations, two subharmonic mixers, the transconductance SHM and the passive SHM are studied, simulated, measured and compared in this work.

Table 4.1 gives a brief performance comparison between the two chosen SHMs: transconductance SHM and passive SHM in [9], [10], [11] and [22]. A comparison of the transconductance SHMs in [9],[10] with passive SHMs in [11],[22] shows that with the same subharmonic index, while the transconduct-

ance SHM has a better gain performance than passive subharmonic mixer, passive subharmonic mixer has better noise performance and smaller power consumption, but used higher LO power.

Table 4.1: Performance comparison of transconductance SHMs

and passive SHMs

| | RF/fT /fmax (GHz) | Conv. Gain (dB) | LO power (dBm) | NF (dB) | Power consumption (mW) |
|---|---|---|---|---|---|
| [9] | 77/80/- | 0.7 | 10 | 23 | 22 |
| [10] | 650/240/330 | -13 | -18 | 42 | 33 |
| [11] | 60/-/- | -13.2 | 3 | - | 0 |
| [22] | 120/270/300 | -8 | 5 | 8 | - |

## 4.3    4th and 2nd transconductance subharmonic mixers

### 4.3.1   Schematic of 4th and 2nd transconductance subharmonic mixers

The schematic of the 245 GHz transconductance subharmonic mixer is shown in figure 4.4. Q1, Q2 are the mixer core and they are biased close to the turn-on voltage in order to maximize the nonlinearity characteristic of the transistors. Resistor ladders are utilized for the Q1 and Q2 biasing. Two parallel shunt series stub transmission lines are used to achieve isolation between the LO and RF ports. A quarter wavelength at LO open shunt stub and a quarter wavelength at LO series stub form an open impedance at LO frequency. A quarter wavelength at RF open shunt stub and a quarter wavelength at RF series stub form an open impedance at RF frequency. The two transmission lines T1 and T2 are used to provide 90 degree phase delay at 245 GHz and the whole input network makes the RF signals become anti-phase while the LO signals are kept in-phase at the input of the transistors.
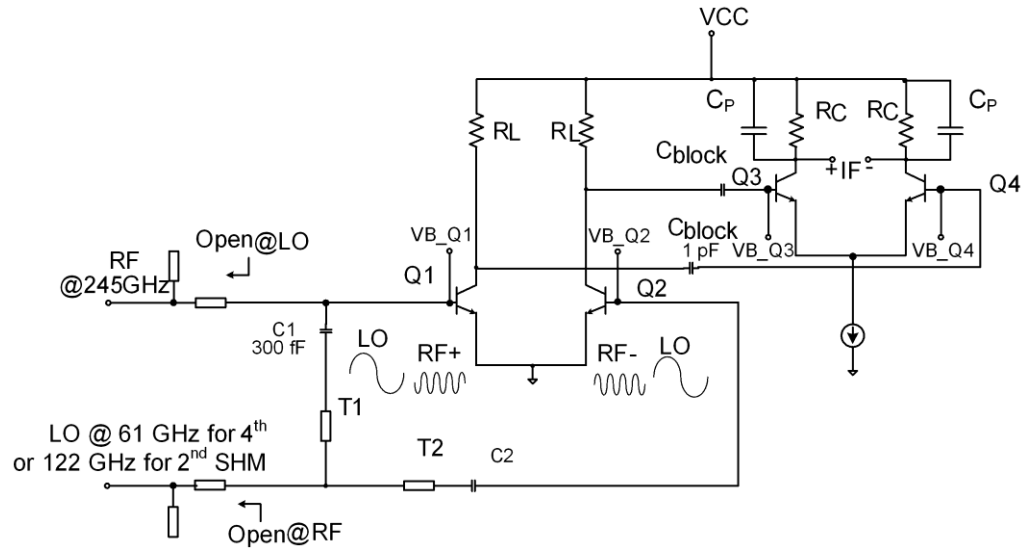
Figure 4.4: Schematic of 4<sup>th</sup> and 2<sup>nd</sup> SHM

In order to enable standalone SHM measurement, after the mixing core stage, a differential common emitter buffer stage is utilized as the output buffer stage to provide impedance matching to 50 Ohm. 50 Ohm resistive loads are used in the buffer for output matching. Filtering capacitors CP (400 fF) are used in parallel to the resistor loads to filter out frequency components higher than IF. Q3 and Q4 are biased with transistor biasing at the base terminal. A capacitor of 1 pF is placed between mixer and buffer stage for DC blocking.

## 4.3.2 Simulation and measurement results of 4<sup>th</sup> transconductance subharmonic mixer

Figure 4.5 shows the chip photo of the 4<sup>th</sup> transconductance SHM in IHP 0.13 um SG13S technology. Chip size is 1*0.75 mm2. On the left are GSG RF input pads, and on the right are the differential GSGSG IF output pads. At the bottom, the 60 GHz LO input pads are located. On the top the DC pads are placed [23].
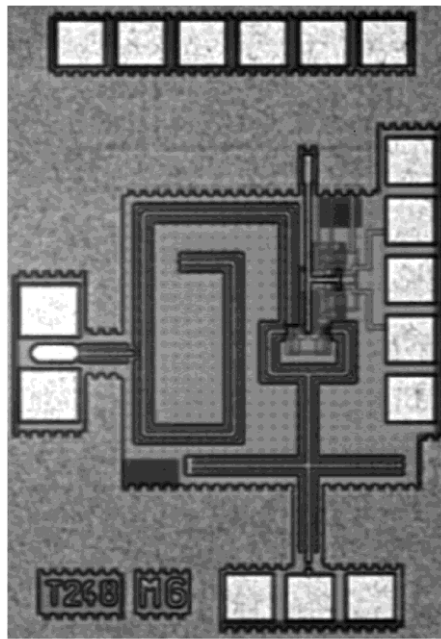
Figure 4.5: chip photo of 4<sup>th</sup> trasconductance SHM

S11 simulation and measurement results of the input RF port are shown in figure 4.6. Measurement and simulation results of conversion gain for the sub harmonic mixer are shown in figure 4.7 and 4.8. The mixer was measured with LO power of 8 dBm for saturation. Figure 4.7 shows the conversion gain of the mixer when the IF is fixed at 1 GHz. It indicates that the conversion gain is -7 dB when the RF frequency is 245 GHz with a 3 dB bandwidth (-9 to -6dB) from 240.5 GHz to 252.7 GHz. The simulated gain of the buffer is 6 dB, so the conversion gain of the mixer core alone is -15 to -12 dB in the frequency range from 240.5 GHz to 252.7 GHz. Figure 4.8 shows the IF frequency response. The conversion gain decreases when the IF frequency increases. Gain drops when the IF frequency decreases due to the DC blocking capacitors between the mixer and buffer stage. In figure 4.7 and 4.8, the differences between the simulated and measured conversion gain is about -5 dB at operating frequency 245 GHz, and this could be due to the inaccuracies of the transistor models or the EM simulation of the passives.

The simulated output 1 dB compression point is at -9.1 dBm. The simulated noise figure is 39 dB at 245 GHz.
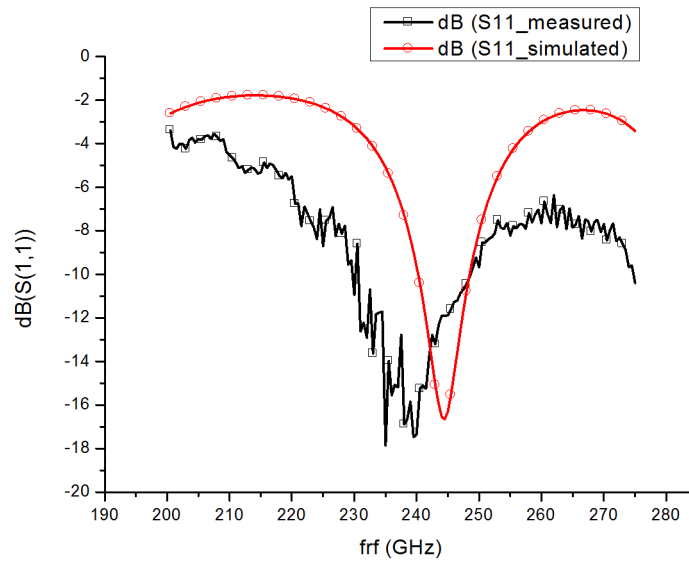
Figure 4.6: S11 simulation and measurement results of SHM at input RF port
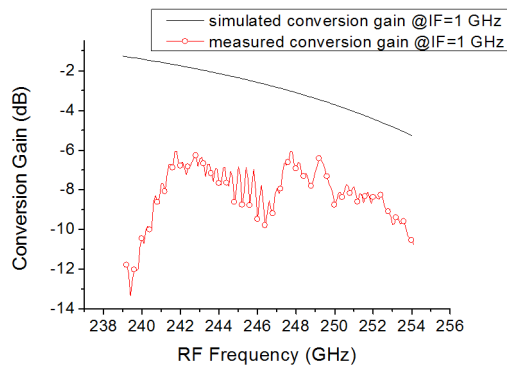


Figure 4.7: Measurement results of SHM with fixed IF at 1 GHz

### 4.3.3 Simulation and measurement results of 2$^{nd}$ transconductance subharmonic mixer

2$^{nd}$ transconductance subharmonic mixer is fabricated in SG13G2 BiC-MOS technology.

Conversion gain of the 2$^{nd}$ transconductance SHM is extracted by subtracting the S21 of CB LNA [1] from the conversion gain of integrated receiver, as shown in section 5.2. Simulated and extracted measured conversion gain of SHM are shown in figure 4.9. There are around 5 dB difference between the simulation and calculated measured results due to inaccuracies of the transistor models or the EM simulations of the passives.
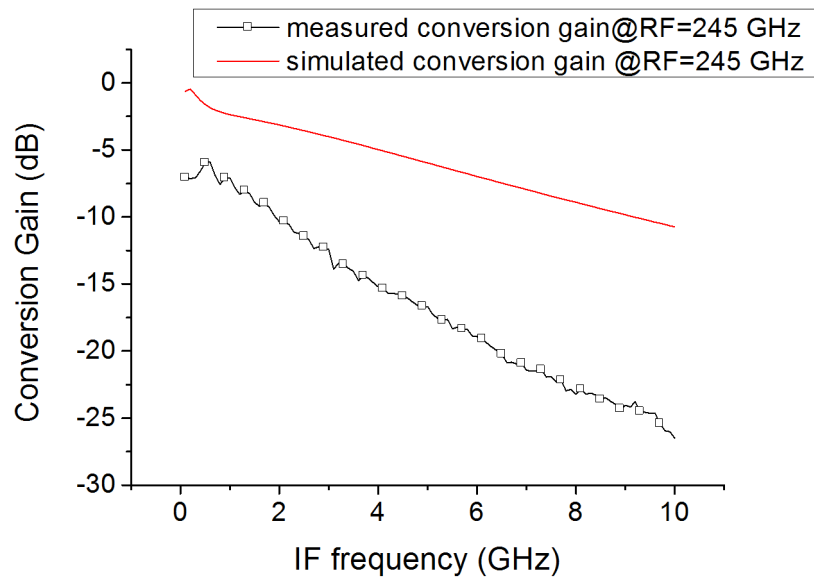
Figure 4.8: Measurement results of SHM with fixed LO at 61 GHz
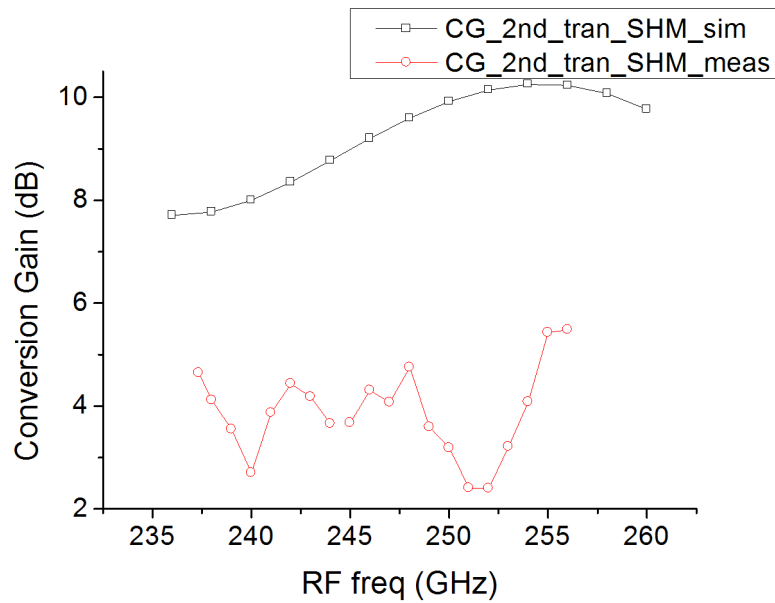


Figure 4.9: Measurement and simulation results of conversion gain of 2$^{nd}$ transconductance SHM with fixed IF frequency of 1 GHz
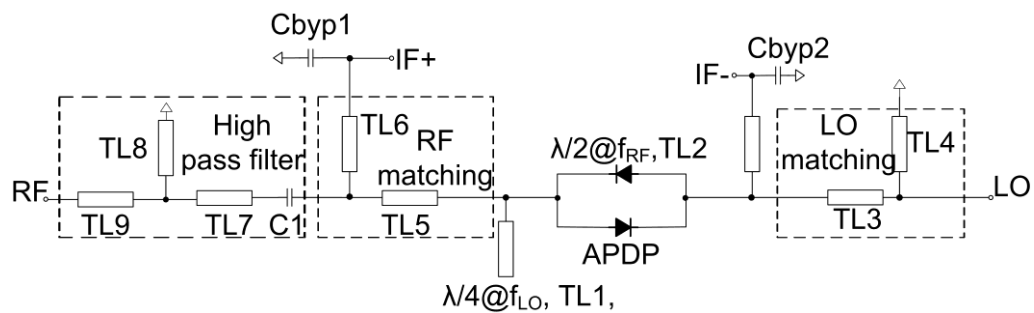


Figure 4.10: Schematic of 2$^{nd}$ passive subharmonic mixer

## 4.4    Passive subharmonic mixer

### 4.4.1    Schematic of passive subharmonic mixer

Figure 4.10 shows the schematic of the passive sub harmonic mixer [24]. An antiparallel diode pair is the mixing core of the passive sub-harmonic mixer. At RF port, TL1, an open quarter wave length shunt stub at LO, forms the grounding for LO signals and open for RF signals, so that the diodes are terminated with a short-circuit at LO signals but RF signals are not affected. Transmission line TL5 and TL6 form the RF matching network. A high pass filter is designed at the input of the RF port, which comprises of transmission lines TL7, TL8, TL9 and capacitor C1 [11]. The high pass filter not only provides good rejection at IF frequency, preventing IF leakage to the RF port and allowing RF signals passing through, but as well resonates out the input capacitance of the bond pad. Similarly, at LO port, TL2, a ground half wave length shunt stub at RF , forms the grounding for RF signals and open for LO signals. Transmission line TL3 and TL4 form the LO matching network. The components used in the input and output networks are electrically small enough at IF to be essentially transparent at IF frequency and IF signals are extracted differentially from both sides of the APDP through the bypass capacitors $C_{byp1}$ and $C_{byp2}$ [22].

In order to provide high local oscillator (LO) power to the $2^{nd}$ APDP SHM, a PA is added between the oscillator and SHMs to amplify the power of oscillating signal. Figure 4.11 shows the schematic of the VCO-PA chain. The PA uses one-stage differential-cascode, with transformer coupled at input and output topology [25]. In [25], the PA is a standalone circuit with input and output matching to 50 Ohm including bondpads and the PA is matched to 245 GHz doubler directly including bondpads. While in this work, the PA is matched to the subhamonic mixer directly including the bondpads.

The schematic of the 120 GHz oscillator is also shown in figure 4.11. The oscillator has to provide a 120 GHz single-ended signal to $2^{nd}$ SHM. A push-push oscillator topology was chosen [13] . With this topology, it is possible to provide a signal path with frequency of 60 GHz to the 1/64 frequency divider and to provide the 120 GHz signal via a buffer to the PA. Cascode circuits are utilized as buffer stages.

### 4.4.2    Measurement results of passive subharmonic mixer

Chip photo of the $2^{nd}$ passive SHM is shown in figure 4.12. The chip is fabricated in SG13G2 BiCMOS technology. The chip includes the VCO-PA

chain. In order to give a clear description of the interface between VCO-PA chain and $2^{nd}$ APDP passive SHM, figure 4.13 presents the output power of the VCO-PA chain versus tuning frequency range. 6.5 dBm output power is obtained at 122 GHz.

The standalone 120 GHz push-push VCO is also measured. The 120 GHz push-push VCO changes from 116.9 GHz to 126.4 GHz by increasing the tuning voltage Vtune from 0 V to 3 V. An output power of about -1 dBm is measured at 122 GHz. Figure 4.14 presents the output power of the VCO versus tuning frequency range. Phase noise of -96dBc/Hz at 1 MHz offset is measured at 1.5 V with a corresponding LO frequency of 122 GHz, as shown in figure 4.15.

Figure 4.16 shows the conversion loss of the passive SHM with fixed VCO tuning voltage $V_{tune}$ of 1.3 V with corresponding VCO-frequency at 122 GHz, when the input RF frequency is swept. The passive SHM achieves a conversion loss of 16 dB when the RF frequency is approaching 244 GHz, with the 3-dB RF frequency bandwidth extending from 241.5 GHz to 246.5 GHz.
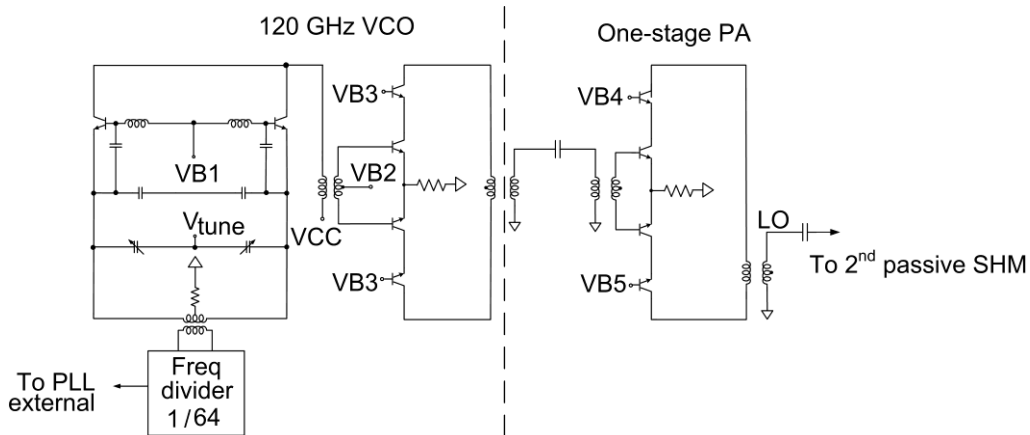


Figure 4.11: Schematic of the 120 GHz VCO-PA chain for $2^{nd}$ passive SHMS
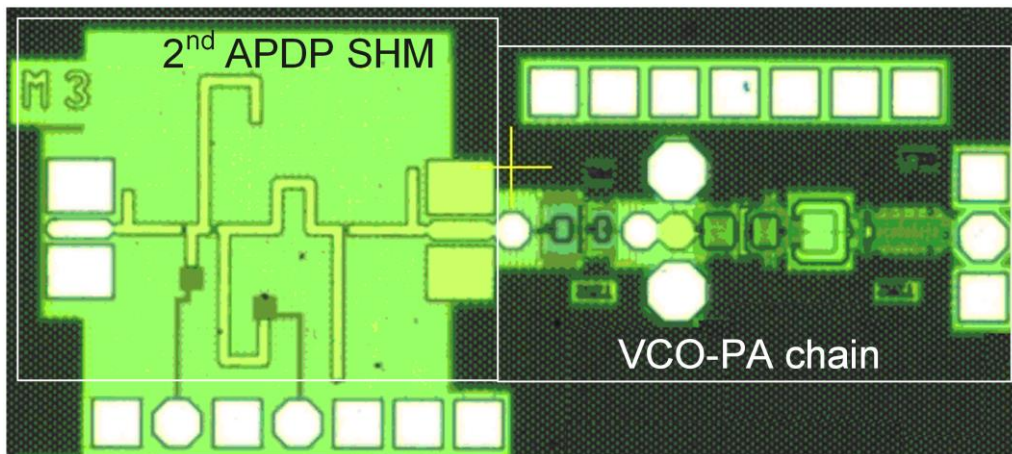


Figure 4.12: Chip photo of $2^{nd}$ passive SHM including VCO-PA chain

Figure 4.16 also presents the conversion loss of the passive SHM versus RF frequency with fixed IF frequency 1 GHz. Input RF frequency is swept from 236 GHz to 255 GHz simultaneously when LO frequency changes from 116.9 GHz to 126.4 GHz by increasing the tuning voltage $V_{tune}$ from 0 V to 3 V to keep the IF frequency constant. Passive SHM achieves 3-dB RF frequency bandwidth extending from 236 GHz to 250 GHz, with a 14 GHz 3-dB bandwidth. Conversion loss of the passive SHM increases when RF frequency goes up.

The simulated 1dB compression point of the passive SHM is at 0 dBm. In measurement, the 1 dB compression point of the passive receiver is larger than -22 dBm.
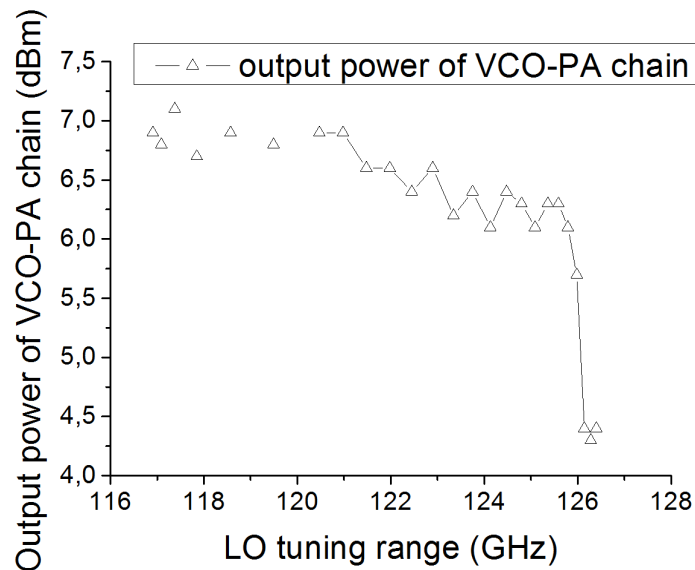
Figure 4.13: Output power of VCO-PA chain versus LO tuning range
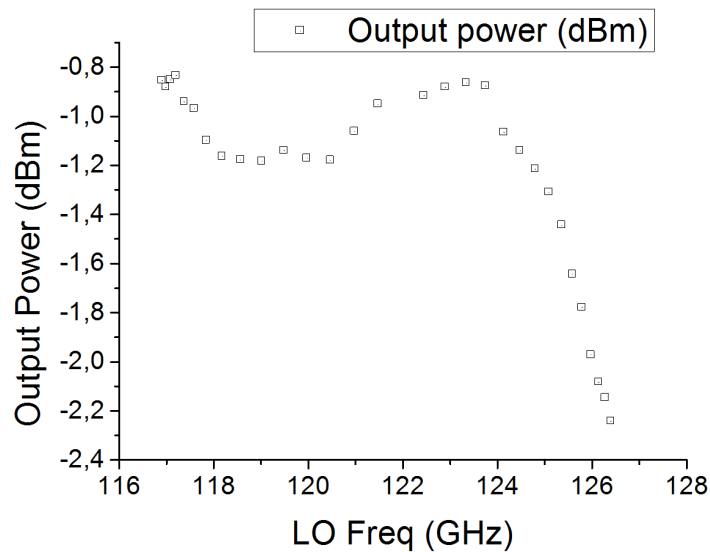
Figure 4.14: Output power of VCO versus LO tuning range
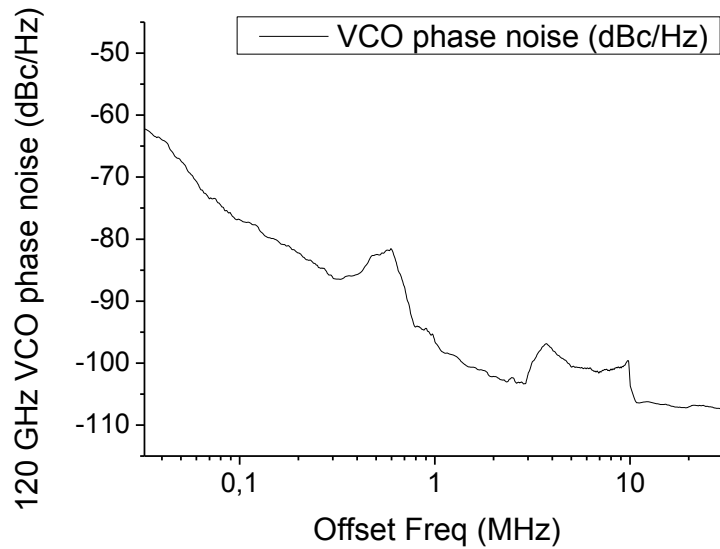
Figure 4.15: Phase noise of the 120 GHz VCO
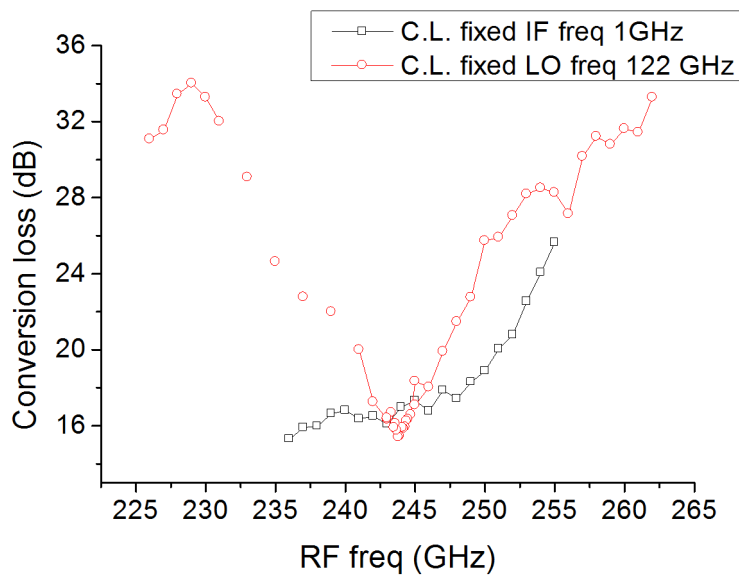


Figure 4.16: Conversion loss of passive SHM versus RF frequency with fixed

IF frequency of 1 GHz, and with fixed LO frequency 122 GHz

## 4.5    3-port measurement setup of SHMs

Measurement setup of the subharmonic mixers for LO signals at 60 GHz is illustrated in figure 4.17. Measurement setup of the subharmonic mixers for LO signals at 120 GHz is illustrated in figure 4.18.

In figure 4.17, 4 port network analyzer ZVA67 provides RF signals RF/18 and (RF/16-279MHz/16) to frequency extender Z325. 245 GHz RF signal is

obtained by the RF signal multiplications in Z325. 245 GHz RF signal is supplied to device under test through the waveguide transition S-band WR 3.4-S-band and probe tip WR 3.4-GSG-50. 61 GHz LO signal is supplied directly by the vector network analyzer. IF signal is displayed on spectrum analyzer FSV30. DC probes MCW-14 Multi-Contact Wedge provide the DC bias for the chip in on-wafer measurements.

In figure 4.18, 4 port network analyzer ZVA67 provides RF signals RF/18 and (RF/16-279MHz/16) to frequency extender Z325. 245 GHz RF signal is obtained by the RF signal multiplications in Z325. 245 GHz RF signal is supplied to device under test through the waveguide transition S-band WR 3.4-S-band and probe tip WR 3.4-GSG-50. 120 GHz LO signal is supplied by VDI AMC 326 and probetip VR 8.0. VDI AMC 326 is an amplifier multiplier by 12 chain, and the LO/12 signal is provided directly by the vector network analyzer. IF signal is displayed on spectrum analyzer FSV30. DC probes MCW-14 Multi-Contact Wedge provide the DC bias for the chip in on-wafer measurements.

Main difference between figure 4.17 and 4.18 is the different LO generation methods for 120 GHz and 60 GHz LO signals.
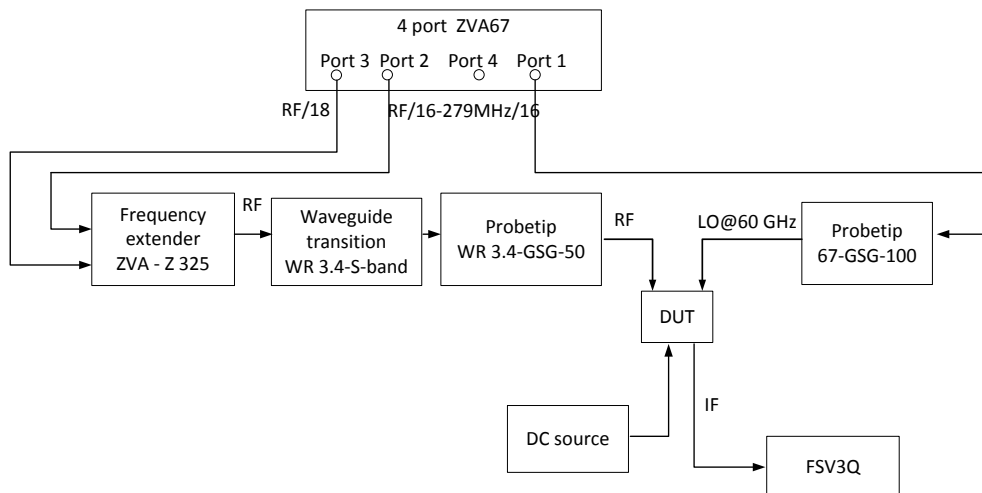


Figure 4.17: SHM measurement setup for LO@60 GHz
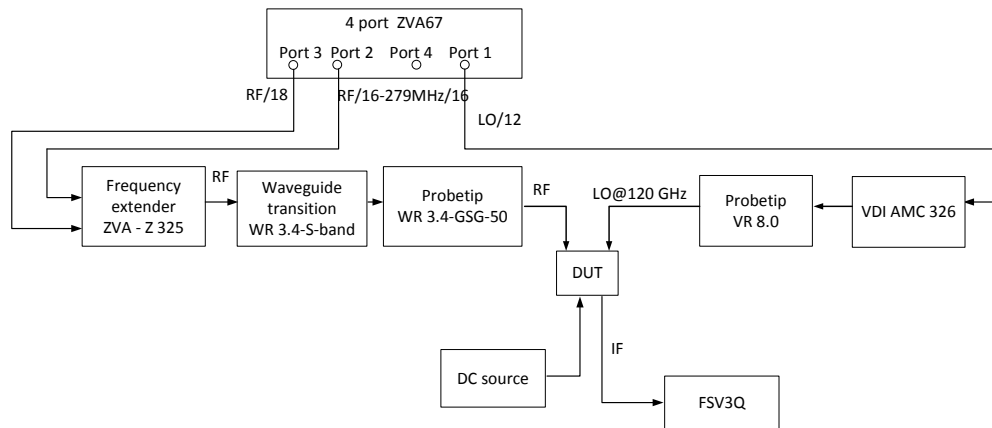
Figure 4.18: SHM measurement setup for LO@120 GHz

# 5     Subharmonic receiver design

## 5.1     4<sup>th</sup> transconductance subharmonic receiver
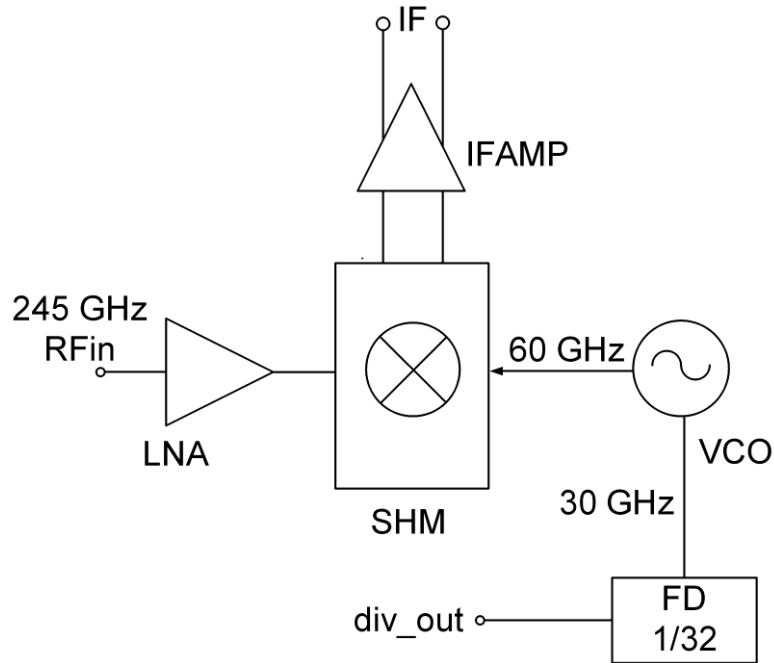
Figure 5.1: Topology of 4<sup>th</sup> transconductance subharmonic receiver

The topology of the 4<sup>th</sup> transconductance receiver is shown in figure 5.1. [1] The integrated receiver is fabricated in SG13G2 technology. The receiver consists of a 245 GHz CB LNA, a 4<sup>th</sup> transconductance SHM, an IF amplifier (IFAMP), a 60 GHz push-push voltage controlled oscillator (VCO), and a 1/32 frequency divider (FD) for the 30 GHz fundamental frequency output of the VCO. Bondpads at the interface of LNA and mixer are excluded, and conjugate matching is implemented between the LNA and mixer interface for maximum power transfer. At the interface between VCO and SHM, VCO output is coupled to SHM by a transformer; bondpads at the interface between VCO and SHM are excluded, and a MIM capacitor with bottom plate connected to ground is placed to represent the bondpad capacitance of SHM; both ports are impedance matched to 50 Ohms and then directly connected. The IFAMP is a two stage pseudo differential common emitter amplifier. The IFAMP utilizes a 300 Ohm poly silicon resistor as load in the first stage. At the output stage, 50 Ohm resisters are utilized as load.

The LNA, SHM and VCO were designed and tested both as separate components as well as in their fully integrated configurations as receivers in IHP SiGe BiCMOS SG13G2 technology. Besides standalone subcircuits,

LNA-SHM chain without VCO is also designed and measured. The LNA is described as in section 3.3; SHM is described in section 4.2.1 and in section 4.2.2; 120 GHz VCO is described in section 4.3.2.
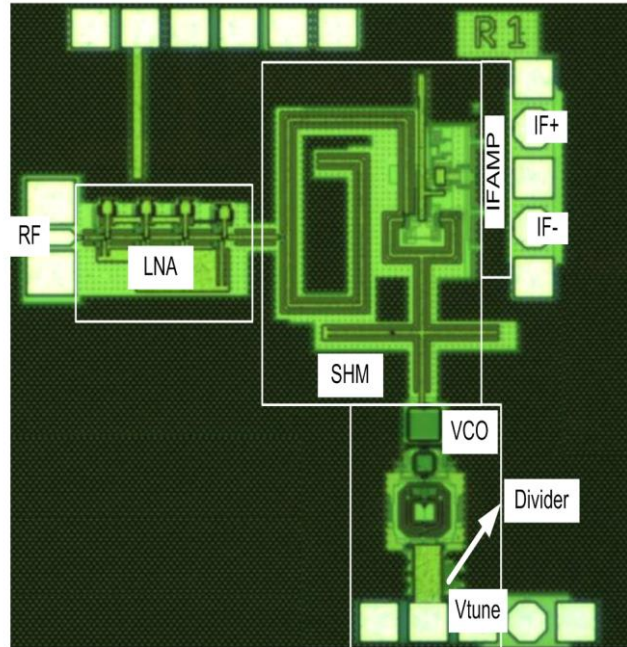


Figure 5.2: Chip photo of 4$^{th}$ transconductance subharmonic receiver

The chip photo of the complete integrated receiver is shown in figure 5.2. The chip size is 1.1x1.3 mm$^2$ . Large areas of decoupling MIM capacitors are included in the chip between the supply and the ground.

The receiver was measured applying 2 V LNA supply voltage with current of 22 mA, 3 V SHM supply voltage with current of 16 mA, 1.3 V supply voltage of IFAMP with current of 13 mA, and 3.3 V supply voltage of the VCO with current of 63 mA. The total chip dissipates only 358 mW.

Figure 5.3 presents the conversion gain of SHM and LNA-SHM chain, when the IF frequency is fixed at 1 GHz and RF and LO frequencies sweep simultaneously with an LO power of 8 dBm for saturation.

Figure 5.4 shows the single-ended conversion gain of the receiver with fixed VCO tuning voltage $V_{tune}$ of 2 V with corresponding VCO-frequency at 60.4 GHz, when the input RF frequency is swept. The receiver achieves 21 dB peak-conversion gain at IF frequency of 1 GHz. Measurement results agree with the simulation results. The conversion gain decreases when the IF frequency decreases due to the DC blocking capacitor (1 pF) between the 4$^{th}$ sub harmonic mixer and the IF buffer amplifier. The 3-dB bandwidth at the upper side band reaches from 241.8 GHz to 243.9 GHz, with the IF 3-dB bandwidth

extending from 0.1 GHz to 2.2 GHz. 3-dB RF bandwidth in the lower-side band extends from 239.7 GHz to 241.3 GHz in mirror, with the IF 3-dB bandwidth extending from 0.4 GHz to 2 GHz. 1 dB compression point is at -37 dBm with IF frequency of 1 GHz and $V_{tune}$ of 2 V. IFAMP contributes around 16 dB gain in the receiver, which is calculated from the difference between the conversion gain of the subharmonic receiver (21 dB) and that of the standalone LNA-mixer chain (5 dB) .
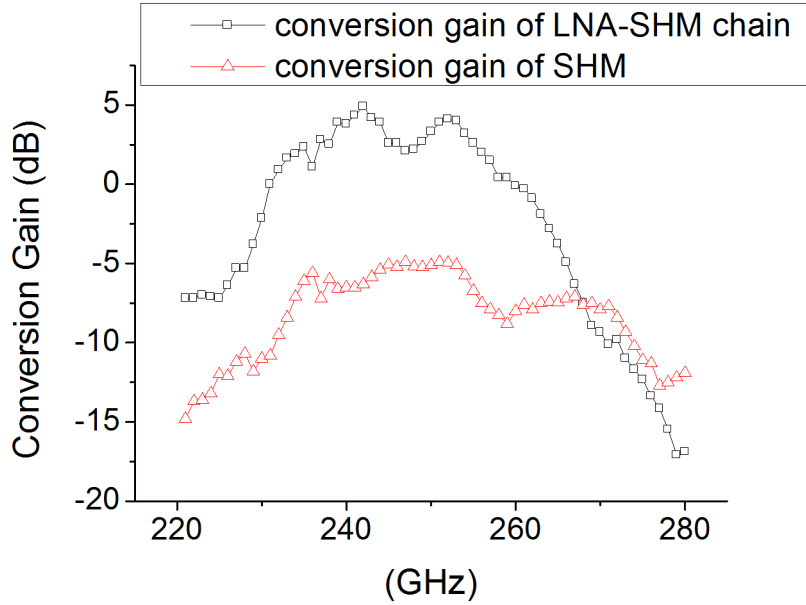


Figure 5.3: Conversion gain of SHM, LNA-SHM chain

Figure 5.5 presents the conversion gain of the receiver versus RF frequency with tuning voltage from 0 V to 3 V and fixed IF frequency 1 GHz. The input RF frequency is swept from 234 GHz to 246 GHz while keeping the IF frequency constant. A tuning bandwidth of 12 GHz is achieved and in the whole frequency range the conversion gain is nearly flat.

With an LO frequency of 60.4 GHz, IF frequency at 1 GHz, corresponding RF frequency of 242.7 GHz, a -121 dBm/Hz output noise power is obtained. According to spectrum analyzer specifications, 95% confidence level is achieved within 0.28 dB deviation. With 21 dB conversion gain, according to equation 5.1 [26], this corresponds to a 32 dB single-side-band (SSB) NF, which exceeds the simulated SSB NF of the receiver 28 dB by 5 dB. This is probably due to the inaccuracy in modeling. In simulation, the NF of the LNA alone is 11.7 dB at 243 GHz, according to Friis equation, the relatively high NF of the 4th subharmonic mixer leads to the high overall noise figure 32 dB.

$$NF = P_0 - N_0 - G \quad (N_0 = -174 dBm / Hz) \tag{5.1}$$
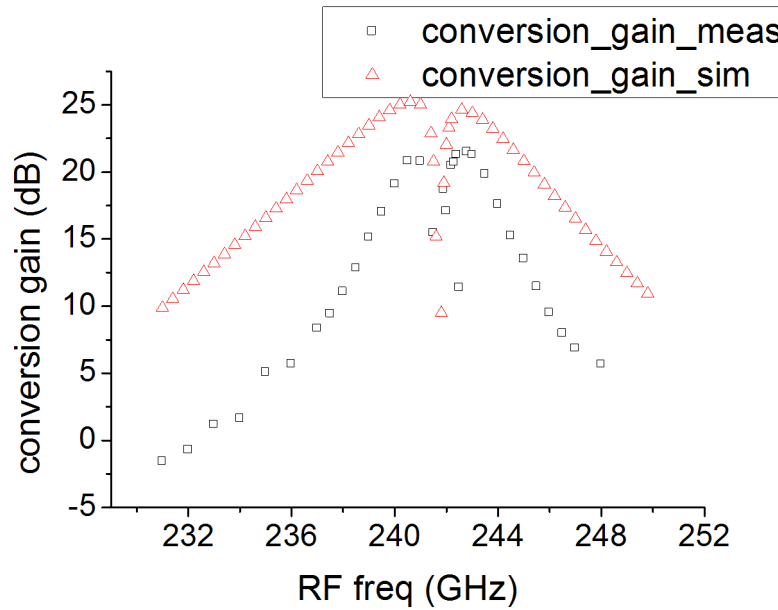
Figure 5.4: Conversion gain of the receiver versus IF frequency

Figure 5.6 presents the measured and simulated SSB NF of the receiver versus IF frequency. SSB NF increases when IF decrease towards DC due to the reduction of the conversion gain. Measurement results agree well with the simulation results.

Figure 5.7 presents measurement results of the output power versus input power sweep. 1 dB compression point is at -37 dBm extrapolated from the power sweep.

## 5.2    2$^{nd}$ transconductance subharmonic receiver

A receiver based on 2$^{nd}$ transconductance SHM and 120 GHz VCO were designed and measured for the 245 GHz ISM band. The receiver consists of a 4 stage common base LNA, 2$^{nd}$ transconductance SHM and 120 GHz VCO, as shownin figure 5.8. [27] The integrated reciever is fabricated in SG13G2 technology. The chip photo of the receiver is shown in figure 5.9. Chip size is only 1.0x1.4mm2. The receiver comprises of CB LNA, 2$^{nd}$ transconductance SHM, 120 GHz VCO. Metal shielding is adapted for the pad design. Large areas of decoupling MIM capacitors are also included in the chip between the supply and the ground.
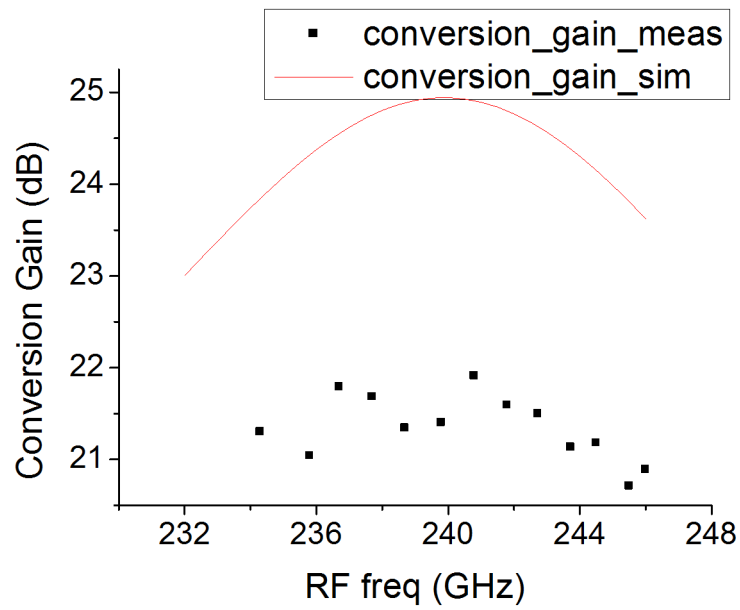
Figure 5.5: Conversion gain of the receiver versus RF frequency with fixed IF

frequency of 1 GHz
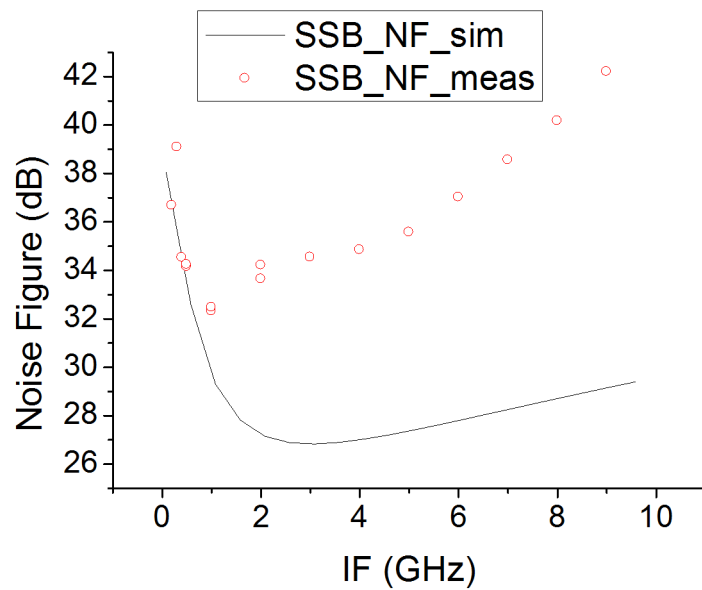


Figure 5.6: SSB NF of the receiver versus IF frequency

The receiver was measured applying 2 V LNA supply voltage with current of 25 mA, 3 V SHM supply voltage with current of 17 mA, and 3.3 V supply voltage of the VCO with current of 28 mA. The total chip dissipates only 200 mW.
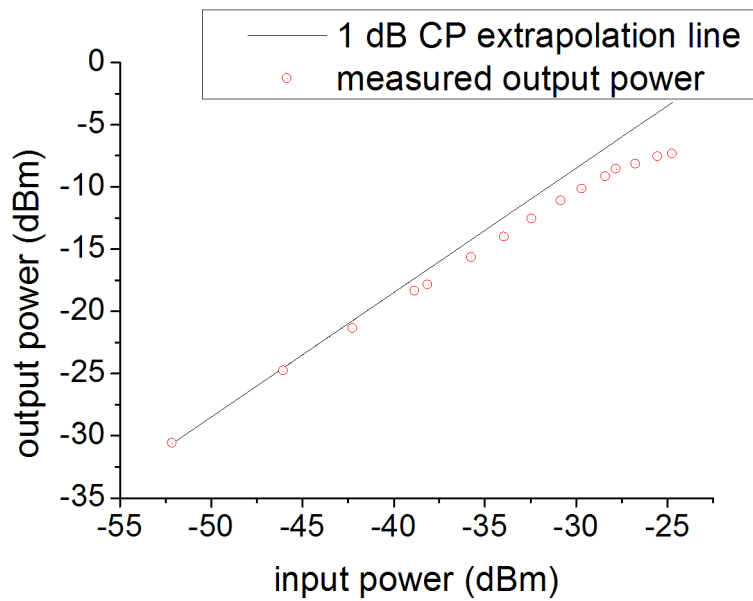
Figure 5.7: output power vs input power sweep
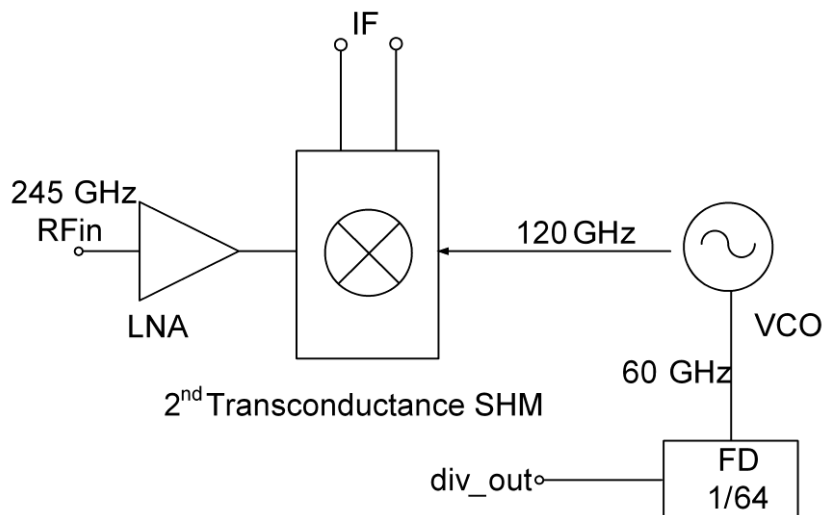


Figure 5.8: Topology of the 2nd transconductance subharmoinic receiver

In order to have a thorough understanding of the gain distribution, and interface between circuit blocks of the receiver, the CB LNA, 120 GHz VCO were designed and tested both as separate components as well as in their fully integrated configurations. Bondpads at the interface of LNA and mixer are excluded, and conjugate matching is implemented between the LNA and mixer interface for maximum power transfer. At interface between VCO and SHM, because both ports are impedance matched to 50 Ohm, the two ports at the interface are connected directly with bondpads.

The CB LNA has a 3-dB bandwidth extending from 237 GHz to 261 GHz. A gain of 11 dB is achieved at 243 GHz, and the simulated NF is 12 dB. The CB LNA measurement results are the same as the CB LNA in IHP SG13G2 technology shown in section 3.3.
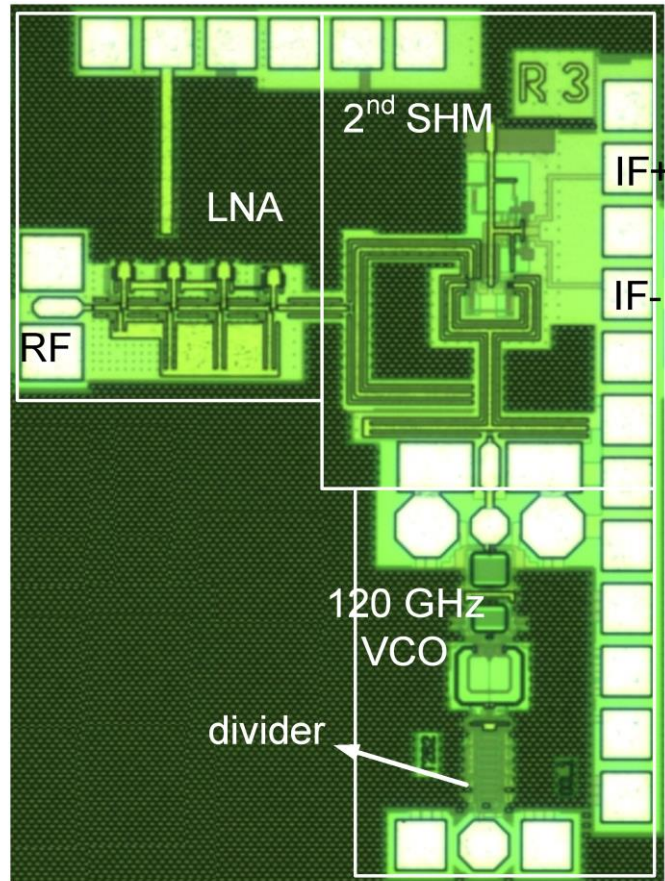
Figure 5.9: Chip photo of the 2$^{nd}$ transconductance subharmonic receiver
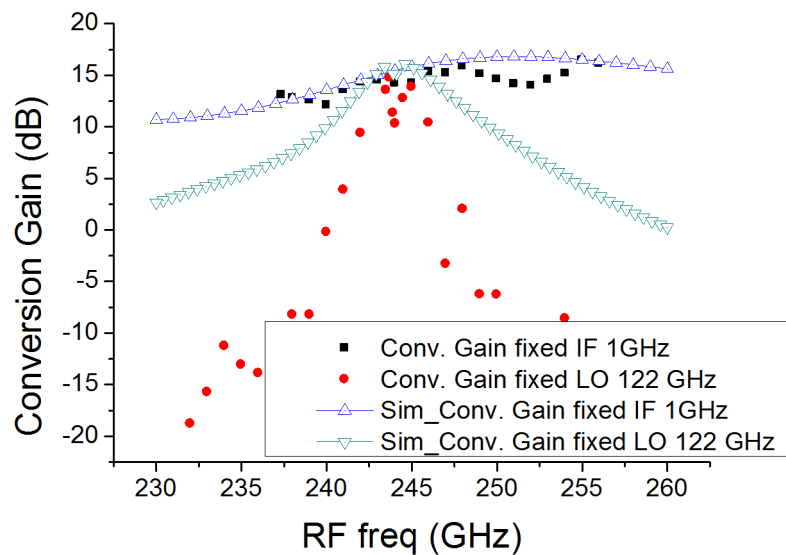


Figure 5.10: Conversion gain of 2$^{nd}$ transconductance subharmonic receiver

versus RF frequency

The VCO-frequency changes from 116.9 GHz to 126.4 GHz by increasing the tuning voltage $V_{tune}$ from 0 V to 3 V. An output power of -1 dBm is meas-

ured at 122 GHz, and a phase noise of -88 dBc/Hz at 1 MHz offset is measured at $V_{tune}$ of 1.3 V with corresponding LO frequency of 122 GHz; phase noise of -96 dBc/Hz at 1 MHz offset is measured at $V_{tune}$ of 0 V. 120 GHz VCO measurement results is the same as the 120 GHz VCO in section 4.3.2.



Figure 5.11: Output IF power versus input RF power

Figure 5.10 shows the simulation and measured conversion gain of the receiver versus RF frequency, with fixed VCO tuning voltage ($V_{tune}$: 1.3 V) which corresponds to an LO frequency of 122 GHz. Measurement results agree fairly well with the simulation results. The receiver achieves 15 dB peak-conversion gain in the lower side band (<244 GHz) with the 3-dB lower RF frequency bandwidth extending from 242.5 GHz to 243.8 GHz; and it reaches 14 dB peak conversion gain in the upper side band (>244 GHz) with 3-dB RF frequency bandwidth extending from 244.03 GHz to 245.9 GHz. The limited IF bandwidth is due to the filtering of capacitors CP (400 fF) in parallel with the load resistors RL in the 2$^{nd}$ SHM as shown in figure 4.4. In figure 5.11, the conversion gain drops when the RF frequency approaches 244 GHz due to the decoupling capacitors between the mixing core and output buffer stage. The 2$^{nd}$ transconductance SHM contributes 3.3 dB gain to the receiver gain, which is calculated from the difference between the conversion gain of the receiver and the gain of LNA.

Figure 5.10 also presents the conversion gain of the receiver with fixed IF frequency at 1 GHz. In this case, LO frequency is swept from 116.9 GHz to 126.4 GHz (tuning voltage from 0 V to 3 V). The input RF frequency is swept simultaneously to keep the IF frequency constant at 1 GHz. The receiver achieves 3-dB RF frequency bandwidth extending from 241 GHz to 256 GHz, with a 15 GHz 3-dB bandwidth.

With an LO frequency of 122 GHz, IF frequency at 1 GHz, and a corresponding RF frequency of 245 GHz, a -142.3 dBm/Hz output noise power is obtained for the receiver. With 14.3 dB conversion gain, this corresponds to a 17 dB single-side-band (SSB) NF [26].

Figure 5.11 presents the output IF power versus the input power with an LO frequency of 122 GHz, IF frequency at 1 GHz, corresponding RF frequency of 245 GHz. The measured input 1 dB compression point is at -24 dBm.

## 5.3    2nd passive subharmonic receiver

2nd passive subharmonic receiver consists of a 4 stage common base LNA, 2nd APDP passive SHM, IF amplifier, and a 120 GHz VCO-PA chain, as shown in figure 5.12. [24] The integrated receiver is fabricated in SG13G2 technology. The IF amplifier is a two stage differential IF amplifier, the schematic of the IF amplifier is shown in figure 5.13. In order to realize DC coupling between the first and second stages, a source follower is inserted between the two stages. At the output, the two load resistors R9, R10 are chosen to be 50 Ohm in order for impedance matching. In measurement, at the output an external differential to single-ended balun is utilized to measure the conversion gain of the receiver. The external balun is calibrated by network analyzer.
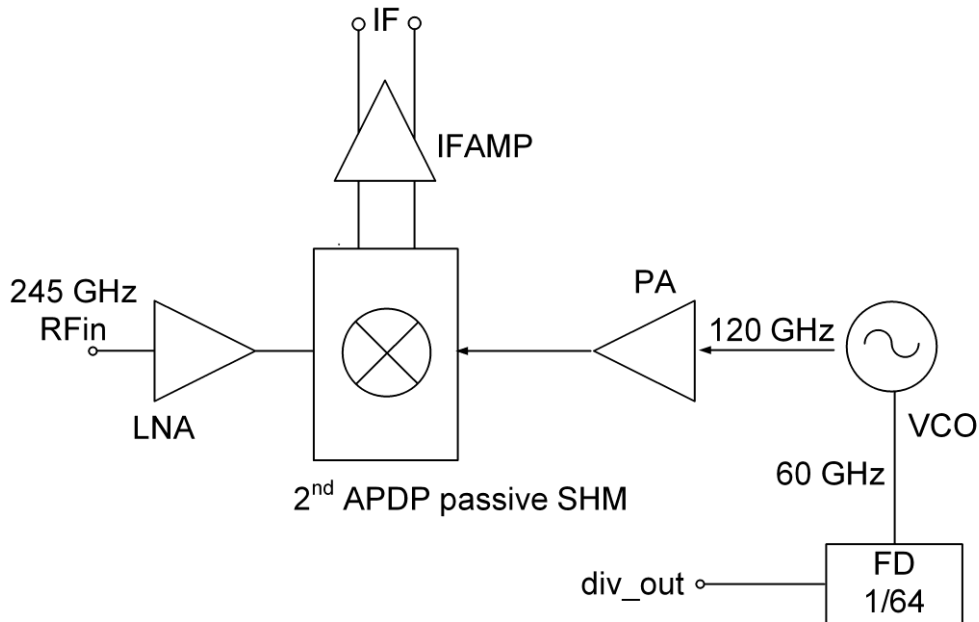


Figure 5.12: Topology of 2nd passive subharmonic receiver
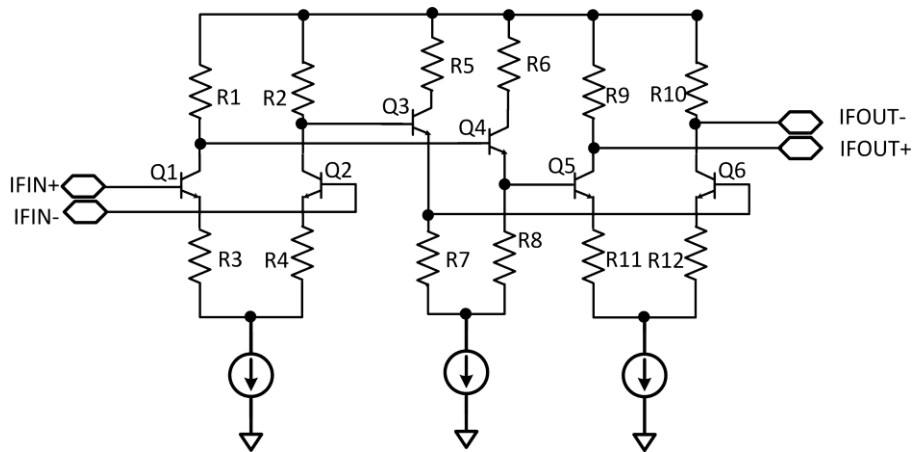
Figure 5.13: Schematic of the two stage differential IF amplifier
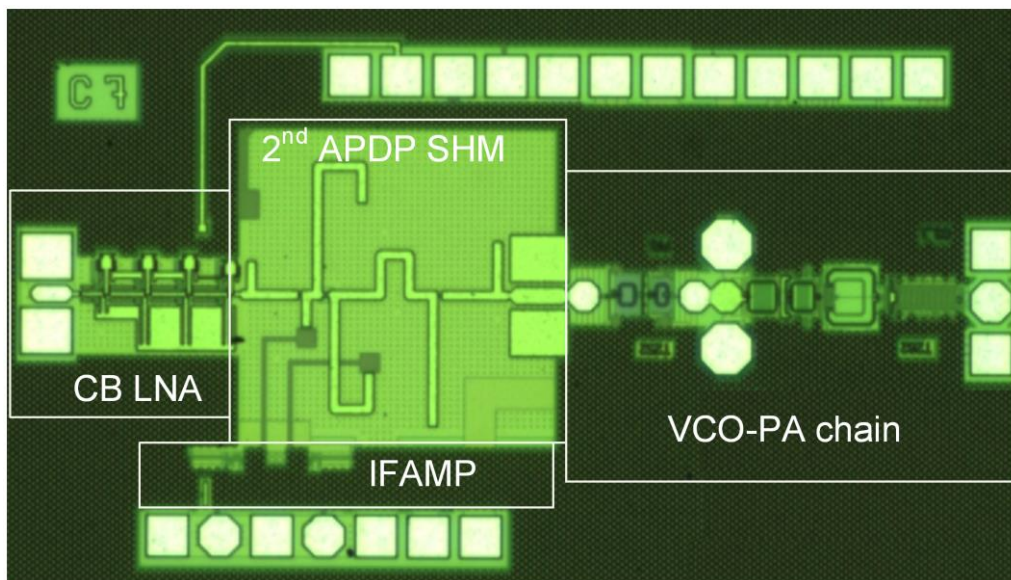


Figure 5.14: Chip photo of 2nd passive subharmonic receiver

In order to obtain a thorough understanding of the gain distribution of the 2nd passive subharmonic receivers, the CB LNA, 2nd passive SHM,120 GHz VCO, 120 GHz VCO-PA chain were designed and tested both as separate components as well as in their fully integrated configurations. Bondpads at the interface of LNA and mixer are excluded, and conjugate matching is implemented between the LNA and mixer interface for maximum power transfer. At interface between VCO-PA chain and SHM, because both ports are impedance matched to 50 Ohm, the two ports at the interface are connected directly with bondpads.

The CB LNA has a 3-dB bandwidth extending from 237 GHz to 261 GHz. A gain of 11 dB is achieved at 243 GHz, and the simulated NF is 12 dB. The CB LNA measurement results is the same as the CB LNA in IHP SG13G2 technology shown in section 3.3.

The VCO-frequency changes from 116.9 GHz to 126.4 GHz by increasing the tuning voltage $V_{tune}$ from 0 V to 3 V. An output power of -1 dBm is measured at 122 GHz, and a phase noise of -88 dBc/Hz at 1 MHz offset is measured at $V_{tune}$ of 1.3 V with corresponding LO frequency of 122 GHz; phase noise of -96 dBc/Hz at 1 MHz offset is measured at $V_{tune}$ of 0 V. The 120 GHz VCO measurement results are the same as for the 120 GHz VCO in section 4.3.2.
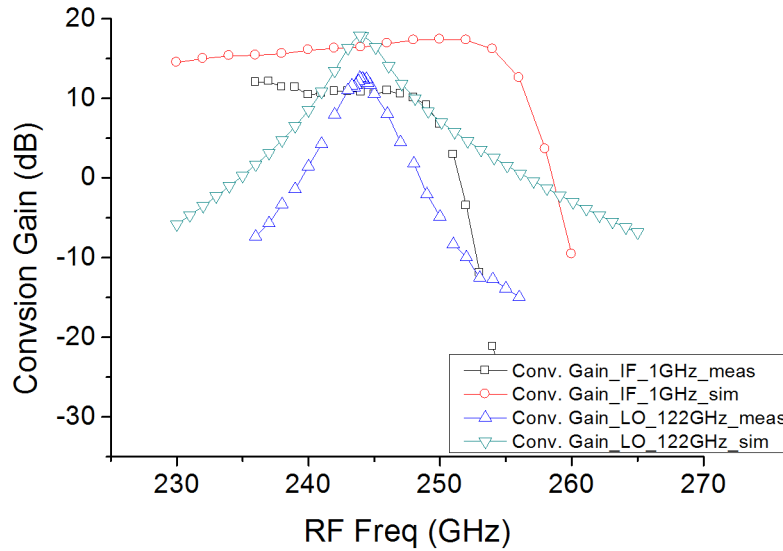


Figure 5.15: Conversion gain of passive receiver versus RF frequency



Figure 5.16: Noise figure of 2$^{nd}$ passive receiver versus IF frequency

For the VCO-PA chain, 6.5 dBm output power is obtained at 122 GHz. Measurement results of VCO-PA chain is the same as in 4.3.2.

A chip photo of the 2nd passive subharmonic receiver is shown in figure 5.14. Chip size of the receiver is 1.9x1.0 mm$^2$. On the left are the RF input GSG pad; on the top are the dc pads for CB LNA, IF amplifier and VCO-PA chain; at the bottom are the GSGSG IF output pads and two redundant dc pads. Metal shielding is adopted for the pad design.

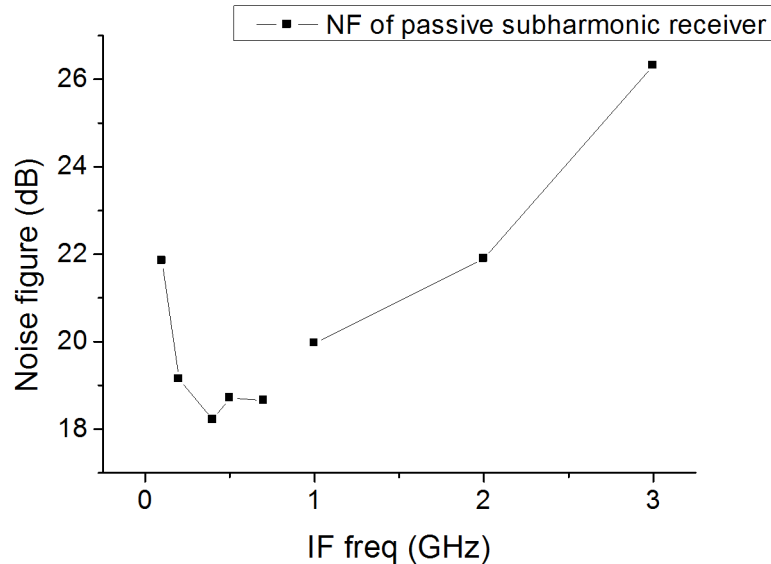The passive receiver was measured applying 2.1 V CB LNA base bias voltage with current of 2.5 mA, 2 V CB LNA supply voltage with current of 24.8 mA, 2.5 V IF amplifier supply voltage with current of 17.9 mA, 4 V PA supply voltage with current of 31 mA and 3.3 V 120 GHz VCO supply voltage with current of 27 mA. The total chip dissipates only 312 mW.

Figure 5.15 shows the conversion gain of the receiver with fixed VCO tuning voltage V$_{tune}$ of 1.3 V with corresponding VCO-frequency at 122 GHz, when the input RF frequency is swept. Passive receiver achieves 12.5 dB peak conversion gain when RF frequency is approaching LO frequency 244 GHz with the 3-dB RF frequency bandwidth extending from 242.5 GHz to 245.5 GHz. The limited IF bandwidth is due to the filtering of bypass capacitors Cbyp1 and Cbyp2 (2 pF) in the 2nd passive SHM. Because there is no ac coupling capacitors either in the IF path of mixer or in IF amplifier, conversion gain reaches maximum when RF frequency approaches LO frequency. The IF amplifier contributes 17.5 dB gain in passive receiver, which is calculated from the difference between the conversion gain of the 2nd passive subharmonic receiver (12.5 dB) and 2nd passive SHM in chapter 4.3.2 (-16 dB), and then further subtraction of the LNA gain (11 dB).

Figure 5.15 also presents the conversion gain of the receiver versus RF frequency with tuning voltage from 0 V to 3 V and fixed IF frequency 1 GHz. The input RF frequency is swept from 236 GHz to 255 GHz while keeping the IF frequency constant. Passive receiver achieves 3-dB RF frequency bandwidth extending from 236 GHz to 249 GHz, with a 13 GHz 3-dB bandwidth. Conversion gain of the receiver drops when RF frequency goes up.

For the 2nd passive receiver, with LO frequency 122 GHz, IF frequency at 1 GHz, corresponding RF frequency is 245 GHz, a -143.4 dBm/Hz output noise power is obtained. With 10.6 dB conversion gain, this corresponds to a 20 dB single-side-band (SSB) NF [26]. Figure 5.16 presents the noise figure of the passive receiver.

The simulated 1dB compression point is at -19 dBm. In measurement, the 1 dB compression point of the passive receiver is larger than -22 dBm.

## 5.4     Measurement setup for subharmonic receivers

Measurement setup of the subharmonic receivers is illustrated in figure 5.17.

4 port network analyzer ZVA67 provides RF signals RF/18 and (RF/16-279MHz/16) to frequency extender Z325. 245 GHz RF signal is obtained by the RF signal multiplications in Z325. 245 GHz RF signal is supplied to device under test through the waveguide transition S-band WR 3.4-S-band and probe tip WR 3.4-GSG-50. 61 GHz or 122 GHz LO signal are supplied internally by the integrated VCO. IF signal is displayed on spectrum analyzer FSV30. DC probes MCW-14 Multi-Contact Wedge provide the DC bias for the chip in on-wafer measurements.
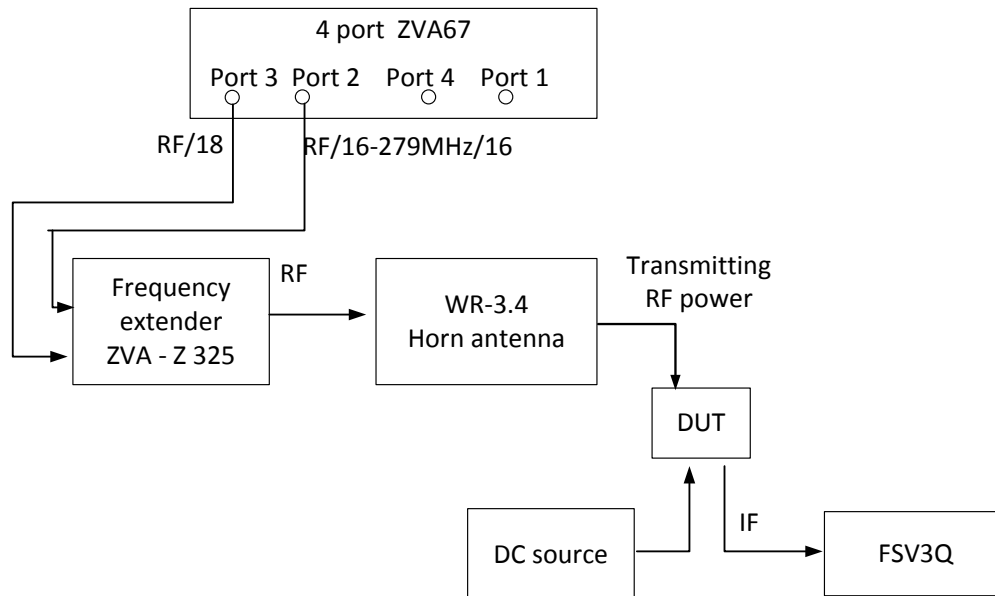


Figure 5.17: Measurement setup

## 5.5     System analysis of three subharmonic receivers

Table 5.1 gives system analysis of the three subharmonic receivers. Gain, noise figure and linearity of each circuit block are measured or simulated in Cadence. Measurement results of overall gain, noise figure and linearity are given. In comparison overall gain, noise figure and linearity of the receivers are as well simulated by ADS system design simulation tools.

For 4th transconductance subharmonic receiver, simulation results of total chain by ADS are in good accordance with the measurement results. For 2nd transconductance subharmonic receiver, there is 7 dB discrepancy between the simulated overall gain and measured overall gain, simulation results of noise figure and linearity performance agree with the measurement results. For 2nd

passive subharmonic receiver, simulation results of total chain by ADS are in good accordance with the measurement results. Due to the RF feed power limitation at 245 GHz of the instruments, 1 dB compression point of passive receiver could not be measured yet.

Comparing 4$^{th}$ transconductance receiver with 2$^{nd}$ transcoductance receiver, 4$^{th}$ transconductance SHM has an NF of 38.8 dB, while 2$^{nd}$ transconductance SHM has an NF of 26.7 dB, therefore 4$^{th}$ transconductance receiver has an overall NF of 32 dB, which is larger than NF of the 2$^{nd}$ transconductance receiver 19 dB. Comparing passive receiver with 2$^{nd}$ transcondcutance receiver, although passive SHM has smaller NF than 2$^{nd}$ transconductance SHM, conversion loss of the passive SHM (-17 dB) in chain with gain of CB LNA (11 dB) fails to compress noise from IF amplifier, therefore the two subharmonic receivers have comparable NF. Therefore low noise IF amplifier should be implemented to improve the noise performance of 2$^{nd}$ passive receiver. There is still headroom for the NF improvement of passive receiver.

2$^{nd}$ passive receiver has the highest 1 dB compression point. 4$^{th}$ transconductance receiver has the smallest 1 dB compression point. Linearity of the 4$^{th}$ transconductance receiver and 2$^{nd}$ passive receiver are mainly limited by the IF amplifier. Optimizing linearity of IF amplifier can still improve the linearity performance of 4$^{th}$ transconductance receiver and 2$^{nd}$ passive receiver.

There is a compromise between gain and linearity in receiver design. 4$^{th}$ transconductance receiver has the highest gain and lowest input 1 dB compression point. 2$^{nd}$ transconductance receiver has the second highest gain and second highest input 1 dB compression point. 2$^{nd}$ passive receiver has the lowest gain and highest input 1 dB compression point.

Table 5.1: System analysis of three subharmonic receivers

|  |  | CB LNA | SHM | IF amp | Total chain (ADS sim) | Total chain (meas) |
|---|---|---|---|---|---|---|
| 4$^{th}$ tran rec. | Gain (dB) | 11 | -5 | 15* | 20.8*** | 21 |
|  | NF (dB) | 10.6** | 38.8** | 3.4** | 30.9*** | 32 |
|  | input 1 dB CP (dBm) | -14.45** | -6.7** | -21.86** | -32.7*** | -37 |
| 2$^{nd}$ tran rec. | Gain (dB) | 11 | 10.8 | - | 21.7*** | 14 |
|  | NF (dB) | 10.65** | 26.7** | - | 19.3*** | 19 |
|  | Input 1dB CP (dBm) | -14.45** | -8.65** | - | -20.4*** | -24 |
| 2$^{nd}$ passive rec. | Gain (dB) | 11 | -17*** | 16.6* | 9.7*** | 10.6 |
|  | NF (dB) | 10.6** | 19.4*** | 5.9** | 16.9*** | 20 |
|  | Input 1dB CP (dBm) | -14.45** | 0** | -21.47** | -19.7*** | >-22 |

*Estimated IF amplifier gain by subtracting measured LNA, SHM gain from the measured conversion gain of the whole chain

**Simulation results in cadence

***Simulation results in ADS

## 5.6    Comparison state of the art

Table 5.2 summarizes the performance comparison of the three receivers with state of the art.

Comparing the three receivers with state of the art, receivers in this work include VCO and has higher integration level than receivers in [28], [29] and [4]. Comparing $2^{nd}$ transconductance receiver and $2^{nd}$ passive receiver with $4^{th}$ transconductance receiver, $2^{nd}$ subharmonic receivers have lower conversion gain (14 dB and 10.6 dB compared with 32 dB in $4^{th}$ transconductance receiver), but have better noise performance due to the $2^{nd}$ subharmonic index is utilized (19 dB and 20 dB compared with 32 dB in $4^{th}$ transconductance receiver), and also better 1 dB compression point (-24 dBm and -19 dBm compared with -37 dBm in $4^{th}$ transconductance receiver). Therefore, with tradeoff between gain, noise and linearity, the two $2^{nd}$ subharmonic receivers are better candidate for gas spectroscopy application than $4^{th}$ transconductance receiver.

Comparing $2^{nd}$ subharmonic receivers in this work with that in [4], transconductance and passive subharmonic receivers in this work have a bit smaller conversion gain (14 dB and 10.6 dB) compared with that of [4] (16 dB), comparable noise figure (19 dB and 20 dB compared with 18 dB in [4]), but much smaller power consumption (107 mW and 99.6 mW) which is only half of the receiver in [4] (216 mW), due to the single-ended receiver topology.

Comparing the two $2^{nd}$ subharmonic receivers in this work, $2^{nd}$ transconductance subharmonic receiver although has a bit higher gain (14 dB) and a bit better noise figure (19 dB) than that of passive subharmonic receiver (gain of 10.6 dB and noise figure of 20 dB), 1dB compression point of passive receiver (-19 dBm) is better than that of transconductance receiver (-24 dBm). Therefore the two $2^{nd}$ subharmonic receivers have comparable performance in gain, noise and linearity tradeoff.

From table 5.2, excluding the power of local oscillating circuits, the two $2^{nd}$ subharmonic receivers have comparable power consumption (107 mW and 99.6 mW); nevertheless including the power of local oscillating circuits, $2^{nd}$ transconductance subharmonic receiver has much lower power (200 mW) than that of passive subharmonic receiver (312 mW), because passive subharmonic receiver requires higher LO power than that of $2^{nd}$ transconductance subharmonic receiver. In order to supply high LO power, an additional P A stage is added in the local oscillating circuits. Therefore, although passive subharmonic mixer has zero power consumption, high LO power requirement leads to even higher power consumption when integrated with local oscillating circuits.

In conclusion, the $2^{nd}$ transcondutance subharmonic receiver and $2^{nd}$ passive subharmonic receiver have comparable performance in gain, noise and linearity tradeoff. The $2^{nd}$ transconductance subharmonic receiver has lower power consumption when including the LO circuits.

Table 5.2: Comparison state of the art

| | RF (GHz) | Ft/fmax | Integration level | LO Freq. (GHz) | Conv. Gain (dB) | Power dissipa-tion(mW) | NF (dB) | 1 dB CP (dBm) | Technology |
|---|---|---|---|---|---|---|---|---|---|
| **[28]** | 220 | - | Atten.,LNA Mixer | 55 | 3.5 | 110 | 7.4 | - | 0.1um mHEMT |
| **[29]** | 220 | - | Atten.,LNA,Mixer, LO-chain | 109 | 2 | - | 8.4 | - | 0.1um mHEMT |
| **[4]** | 220 | 280/435 | LNA, Mixer | 110 | 16 | 216 | 18 | - | .13um SiGe HBT |
| **$4^{th}$ tran rec. (This work)** | 245 | 300/500 | LNA,$4^{th}$ SHM IFAMP,VCO | 61 | 21 | 358/158 (w./w.o.) | 32 | -37 | .13um SiGe HBT |
| **$2^{nd}$ tran rec. (This work)** | 245 | 300/500 | LNA, $2^{nd}$ SHM VCO | 122 | 14 | 200/107 (w./w.o.) | 19 | -24 | .13um SiGe HBT |
| **$2^{nd}$ passive rec. (This work)** | 245 | 300/500 | LNA,$2^{nd}$ SHM IFAMP,VCO-PA | 122 | 10.6 | 312/99.6 (w./w.o.) | 20 | -19(sim) >-22(meas) | .13um SiGe HBT |

*w./w.o.: with/without VCO

# 6 Subharmonic receiver in gas spectroscopy application

## 6.1 Dynamic range of 2$^{nd}$ transconductance subharmonic receiver

### 6.1.1 Sensitivity and dynamic range

The thermal noise power level $P_{no}$ of a receiver, with conversion gain $G_A$ and noise figure NF is given in equation 6.1 [34].

$$P_{no} = kTBG_A NF \qquad (6.1)$$

$K$ is Boltzmann's constant, $T$ is absolute temperature, $B$ is bandwidth. Observing that $10\log_{10}(kT) = -174\ dBm$ and assuming that the minimum detectable input level is X decibels above the thermal noise, we can write for the output minimum detectable signal power $P_{o,mds}$:

$$P_{o,mds} = -174dBm + 10\log(B) + 10\log(G_A) + 10\log(NF) + X(dB) \qquad (6.2)$$

And for the corresponding input minimum detectable signal power or sensitivity $P_{sensitivity}$ in other words:

$$P_{sensitivity} = -174dBm + 10\log(B) + 10\log(NF) + X(dB) \qquad (6.3)$$

Assuming the input 1 dB compression point and output 1 dB compression point are $P_{in,1dB}$ and $P_{o,1dB}$ respectively, now the dynamic range of receiver is

$$DR = P_{in,1dB} - P_{sensitivity} = P_{o,1dB} - P_{o,mds} \qquad (6.4)$$

### 6.1.2 Sensitivity and dynamic range of 2$^{nd}$ transconductance subharmonic receiver

In this chapter, 2$^{nd}$ transconductance subharmonic receiver is utilized in the gas spectroscopy. Sensitivity and dynamic range of 2$^{nd}$ transconductance subharmonic receiver is calculated.

For the sensitivity, the overall noise bandwidth B of the receiver rather than the RF bandwidth is relevant. This means, that e.g. bandpass filtering at IF or low-passfiltering after power detection in the spectrum analyzer increases the sensitivity extremely. Sensitivity relies only on the smallest narrow-band

filtering in the receiver chain. According to the receiver measurement setup configuration, it is approximately determined by the resolution bandwidth (RBW) of the spectrum analyzer. RBW of the spectrum analyzer is 3 MHz. Referring to section 5.2, NF is of 17 dB, conversion gain $G_A$ is of 14.3 dB, input referred 1 dB compression point is -24 dBm. Therefore according to equation 6.3, the sensitivity of the receiver is:

$$P_{sensitivity} = -174 + 10\log(3*10^6) + 17 + X = (-92.22 + X) \text{ dBm} \qquad (6.5)$$

According to equation 6.4, the dynamic range of the receiver is :

$$DR = P_{in,1dB} - P_{sensitivity} = -24 - (-92.22 + X) = (68.22 - X) \text{ dB} \qquad (6.6)$$

In equation 6.5, 6.6, X is the minimum detectable input signal level above the thermal noise (in decibels).

From equation 6.3 we can see that by changing B we can increase or decrease sensitivity and hence DR. This would however affect the measurement speed. Referring to section 5.2, the gain variation of the receiver in the frequency band is 2.6 dB. In a heuristic way, assuming that X should be larger than the gain variation of the receiver in the frequency band of interest plus 10 dB for reliable detection above the noise floor, therefore X is around 12.6 dB, $P_{sensitivity}$ is -79.62 dBm, and DR is 55.62 dB.

## 6.2    On-chip antenna design

At frequencies beyond 200 GHz, it is extremely difficult and costly to interconnect the front-end IC with an off-chip antenna. On the other hand, on-chip antennas can be made quite small and exhibit very good matching properties due to the precise lithography and semiconductor fabrication process. IHP has developed several on-chip antennas for mm-Wave applications [45][30][31].
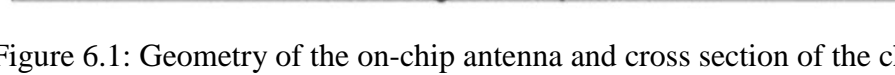
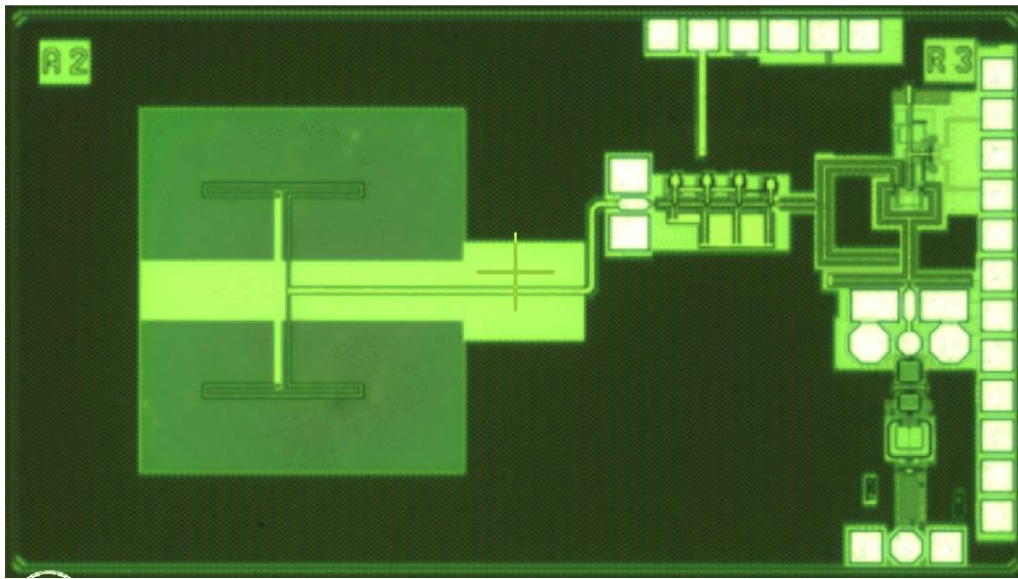Figure 6.1: Geometry of the on-chip antenna and cross section of the chip

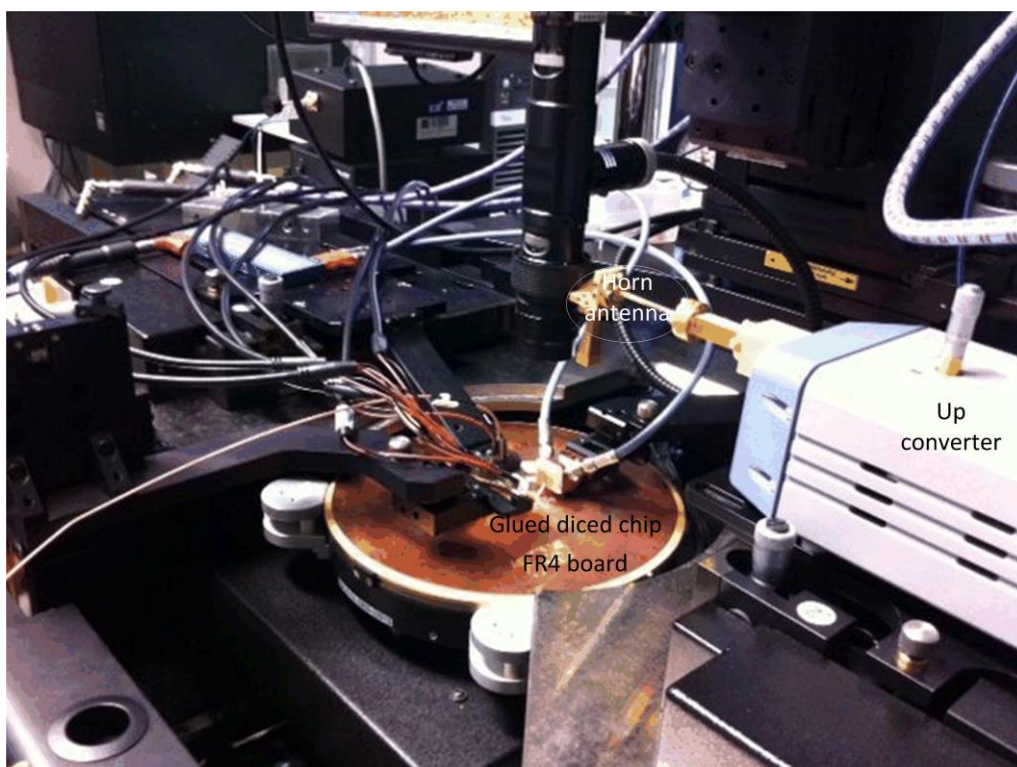Figure 6.2: Chip photo of 2$^{nd}$ transconductance subharmonic receiver

with antenna



Figure 6.3: A picture of the on-chip measurement of subharmonic receivers

with antenna

One of these on-chip antennas has been integrated with the 2$^{nd}$ subharmonic receiver [30]. The antenna design is shown in figure 6.1 [31].
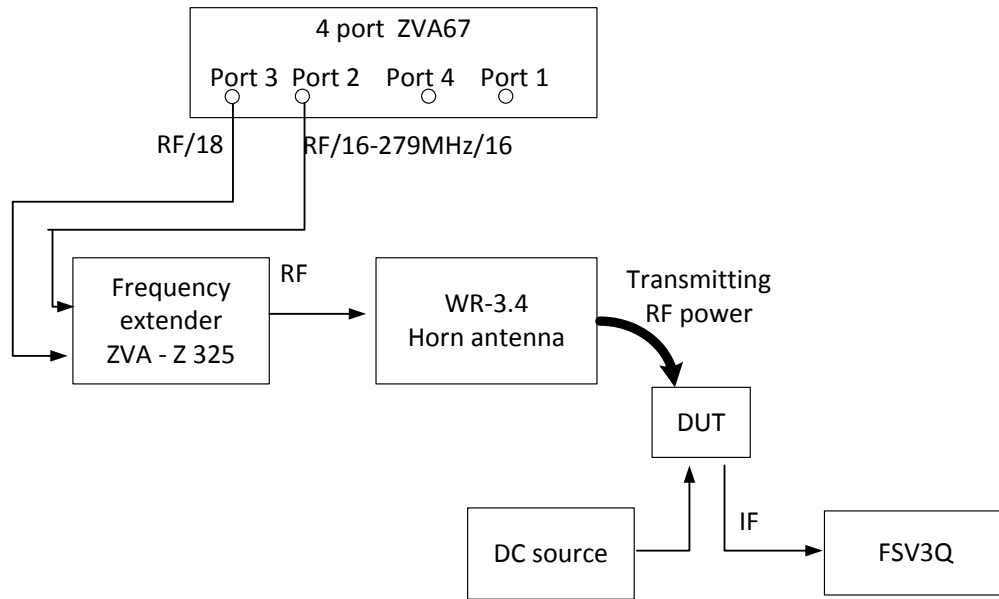
Figure 6.4: Details of the setup of the on-chip measurement of subharmonic receivers with antenna
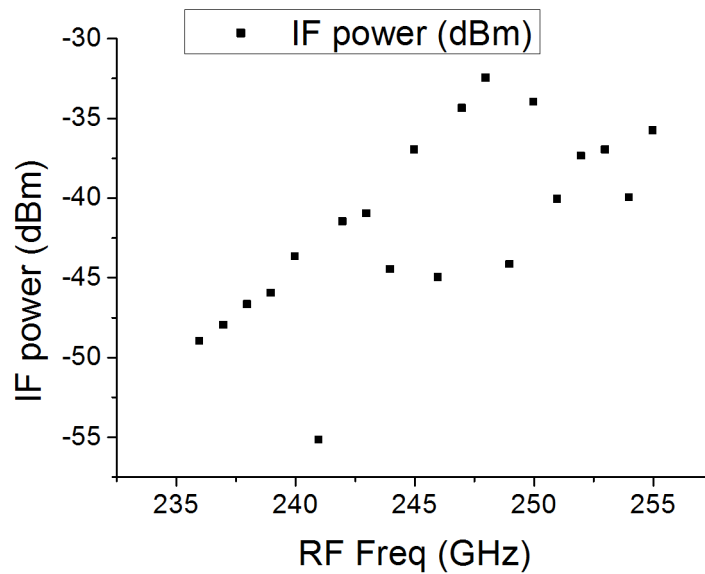


Figure 6.5: Output power of IF signals at 250 MHz

In IHP SG13G2 technology, the top thick layer TM2 is used to realize the radiators and the feeding transmission lines, while M1 serves as ground layer for both the circuit and the feeding lines. The antenna is composed of two half-wavelength folded dipoles. It is connected directly to the input of LNA by a 50 Ohm microstrip transmission line. The ground plane of the module acts as a reflector for the antenna. The height of the antenna above the reflector, which is approximately equal to the thickness of the silicon bulk, is optimized to be 200 µm for better performance. The on-chip antenna achieves gain of around 7 dBi

throughout the bandwith 235 GHz-255 GHz. Figure 6.2 shows the chip photo of the 2nd transconductance subharmonic receiver with on-chip antenna.

## 6.3 On chip measurements of 2nd transconductance subharmonic receiver with on-chip antenna

### 6.3.1 3-port measurement setup for 2nd transconductance subharmonic receiver with on-chip antenna

On chip measurements of the 2nd transconductance subharmonic receiver is performed. Figure 6.3 is a picture of the setup of the measurement.

In figure 6.3, the diced chip of the subharmonic receiver with on-chip antenna is glued on an FR4 board in order to perform measurements. Frequency extender ZVA-Z325 is working as frequency up-converter and feeds the up-converted 245 GHz RF signals into a standard WR-3.4 horn antenna [30]. The yellow horn antenna transmits power towards the glued diced receiver chip. The diced receiver chip receives 245 GHz RF signal through on-chip antenna, downconvert the RF signal and deliver the IF signals.

Figure 6.4 shows more details of the equipment setup. 4 port network analyzer ZVA6F provides RF signals RF/18 and (RF/16-279MHz/16) to frequency extender Z325. 245 GHz RF signal is obtained by the RF signal multiplications in Z325. 245 GHz RF signal is transmitted to the DUT by WR-3.4 horn antenna. A 122 GHz LO signal is supplied internally by the integrated VCO. The IF signal is displayed on the spectrum analyzer FSV3Q. DC probe MCW-14 Multi-Contact Wedge provides the DC bias to DUT.

### 6.3.2 Measurement results of 2nd transconductance subharmonic receiver with on-chip antenna

Using the setup mentioned above, with IF frequency fixed at 250 MHz, the IF output power is measured as shown in figure 6.5.

According to Friis power transmission equation 6.7, where $P_t$ is transmit power, $G_t$ and $G_r$ are the transmit and receive antenna gain, and R is the distance between antennas, $\lambda$ is wave length, the link budget can be calculated according to

$$P_r = P_t \frac{G_t G_r \lambda^2}{(4\pi R)^2} \tag{6.7}$$

Assuming $G_t$ of the horn antenna is 20 dBi, $G_r$ is 7 dBi, the distance between the horn antenna and chip is 10 cm, according to equation 6.7, the received RF power $P_r$ is $P_t - 33.22$ dBm. Accordingly, the conversion gain of the receiver can be obtained by subtraction $P_r$ dBm from the received IF signal power. The results are as shown in figure 6.6.
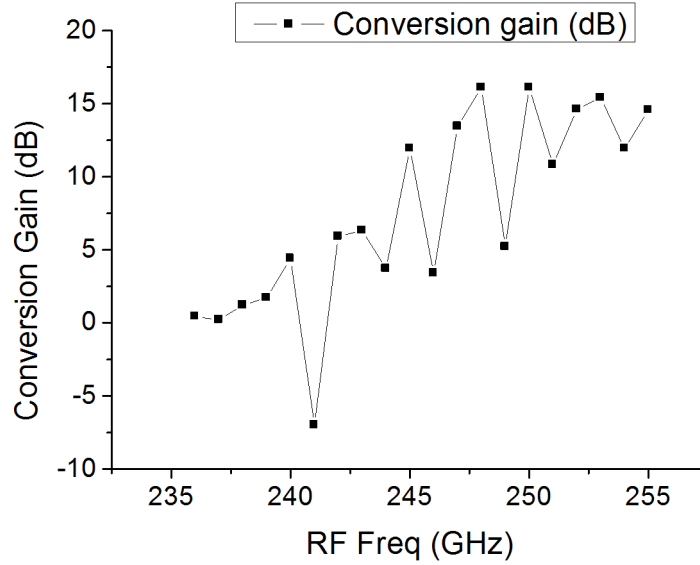


Figure 6.6: Calculated conversion gain of receiver
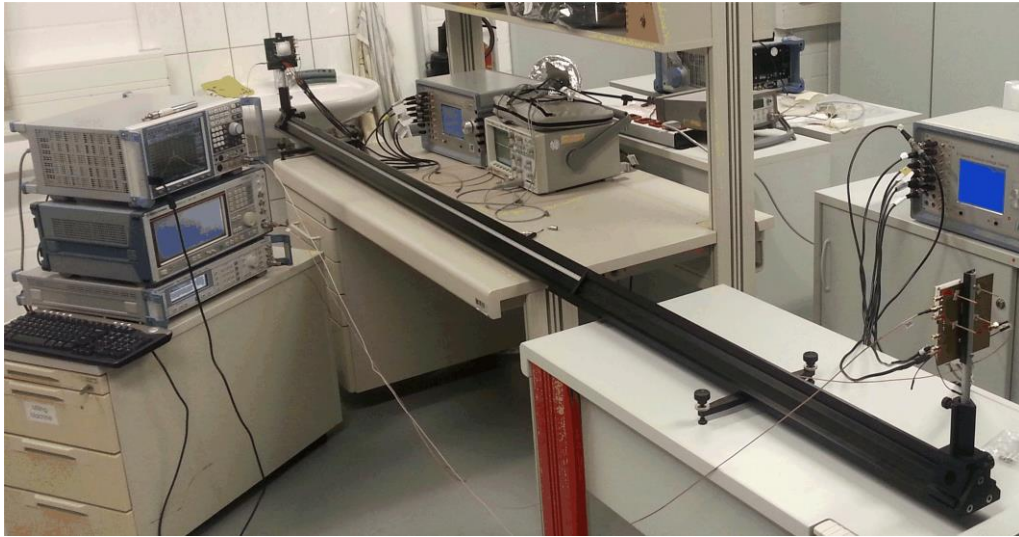


Figure 6.7: Setup of gas spectroscopy application

## 6.4    2$^{nd}$ transconductance subharmonic receiver in gas spectroscopy application

The demonstrator of the gas spectroscopy uses an optical bench for movable mounting of TX and RX boards, see figure 6.7.

For the RX board, the 245 GHz receiver chip is bonded on a plug-in board. The plug-in board is then mounted on a carrier board with a PLL device (ADF4007). For the TX board, the 245 GHz transmitter chip is also bonded on a plug-in board and then mounted on a carrier board with PLL devices as well. The output power of 245 GHz transmitter without on-chip antenna is 0 dBm. The EIRP with on-chip antenna is 7 dBm at 245 GHz. For more details on the 245 GHz transmitter, the reader is referred to [31]. For both TX and RX chips, in order to improve the gain, a dielectric lens has been attached above the on-chip antenna. The lens is made of High Density Polyethylene (HDPE) with a permittivity of $\xi r= 2.32$ and has a diameter of 40 mm and a focal length of 25 mm. It is of plano-convex type with two refracting surfaces. Thus energy reflected at the lens surface is not radiated back towards the antenna and disturb the performance. Comparing on-chip antenna alone and on-chip antenna together with lens, the gain increases from 7 dBi to 33 dBi. The half power beamwidth (HPBW) decreases from 62◦ to 2.1◦. The lens are shown in figure 6.7. The focal distance of the lens can be used to tune the gain of the antenna-lens combination.
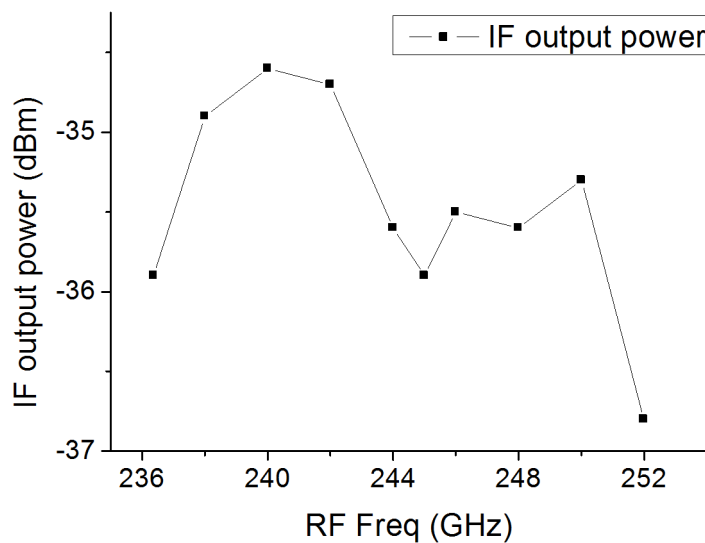


Figure 6.8: IF output power versus RF frequency

The VCO of TX and RX are controlled by two PLLs to obtain a stable IF frequency. The reference signals for the PLL are delivered from two high-quality signal generators (SML01 from Rhode Schwarz). With TX and RX 1.5 meter apart, by simultaneously changing the reference signal of the two PLLs in TX and RX, a fixed IF frequency of 163 MHz is obtained. TX frequency changes from 236.4 GHz to 252 GHz, while LO frequency of RX changes from 236.5 GHz to 252.1 GHz. The power of the IF signal versus RF frequency is shown as in figure 6.8. In the whole frequency tuning range, the IF output

power is within 3 dB bandwidth. Figure 6.9 shows the IF spectrum when TX and RX is 1.5 meter apart.

According to equation 6.7, assuming the far field condition, $P_t$= 0 dBm, $G_r$= 20 dBi, $G_t$= 20 dBi, the received RF power $P_r$ is -43.74 dBm. The conversion gain of the receiver can be obtained by subtraction -43.74 dBm from the received IF signal power. The results are as shown in figure 6.10. Compare the calculated conversion gain with on-chip conversion gain measurement results (14 dB) in Chapter 5, there are around 4 dB differences. This might be due to the impedance mismatching between antenna and LNA or loss due to propagation effects.
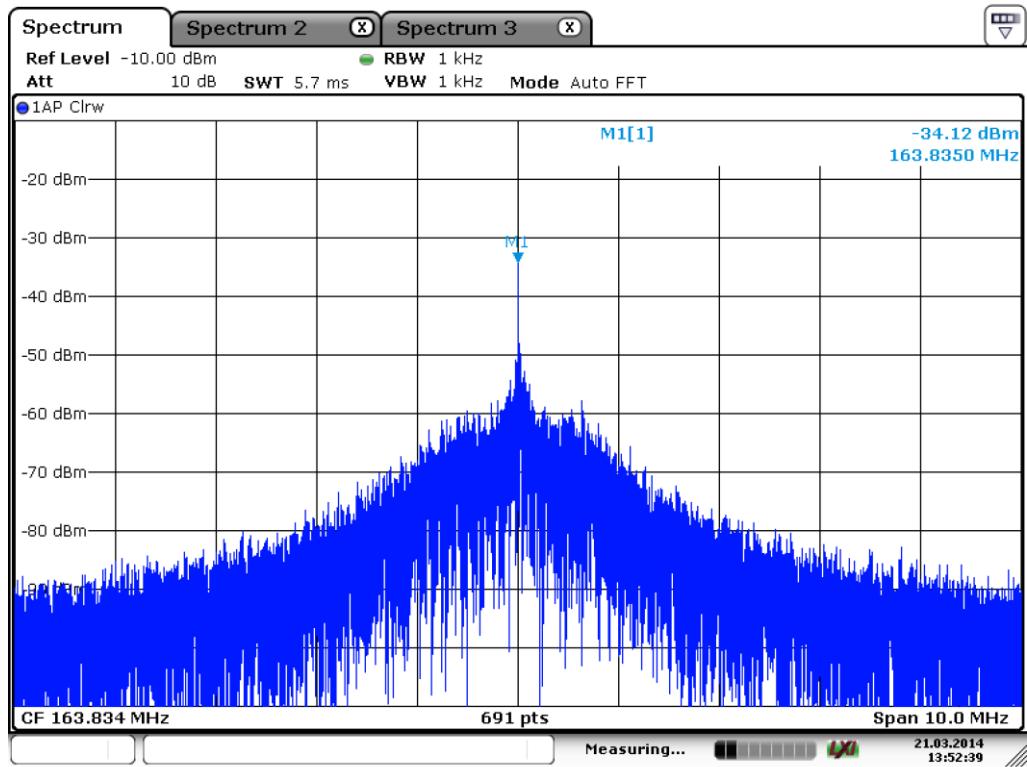


245GHz_TX_10cm_distance
Date: 21.MAR.2014 13:52:38

Figure 6.9: IF spectrum of the received signal:IF frequency at 163 MHz,

TX and RX 1.5 meter apart

By using a 0.6m long gas absorption cell between TX and RX , a gas spectroscopy demonstrator is built, see figure 6.11. On the left is TX , on the right is RX. For this experiment another receiver chip with slightly higher gain (5 dB) but otherwise comparable performance in noise figure (17.4 dB) was used.[33] The experiment was carried out in cooperation between group of Prof Hübers, DLR, Germany and IHP.

The applicability of sensor system was demonstrated by the measured spectra of methanol. The spectra are obtained by applying frequency ramps for the reference frequency of TX and RX, respectively, with constant frequency offset to generate fixed IF signal of RX. The IF power is recorded during ramping time by a spectrum analyzer. Figure 6.12 shows the absorption spectrum of methanol with gas pressure of 20 Pa after processing of data from spectrum analyzer. The ramping time is 1616 s to measure the presented spectrum, and the spectrum analyzer recorded 16160 data points during this time. Note the excellent agreement between the simulated and the measured spectrum (base line correction) [33].
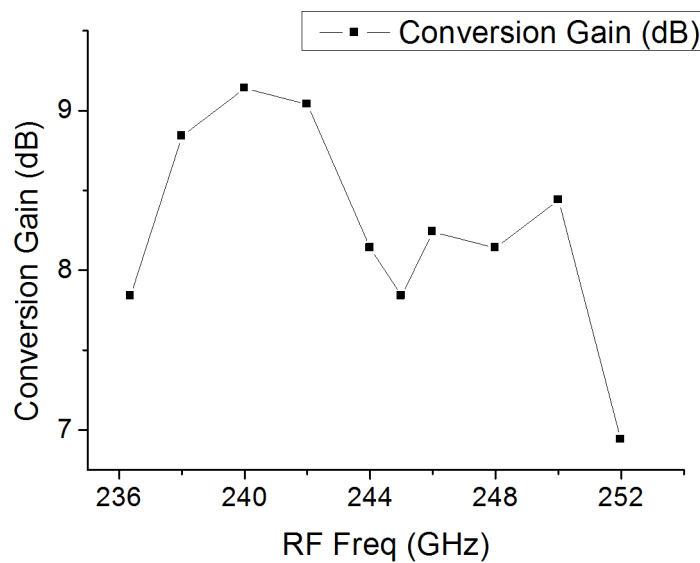


Figure 6.10: Caculated conversion gain of subharmonic receiver according to power transmission link in gas spectroscopy system
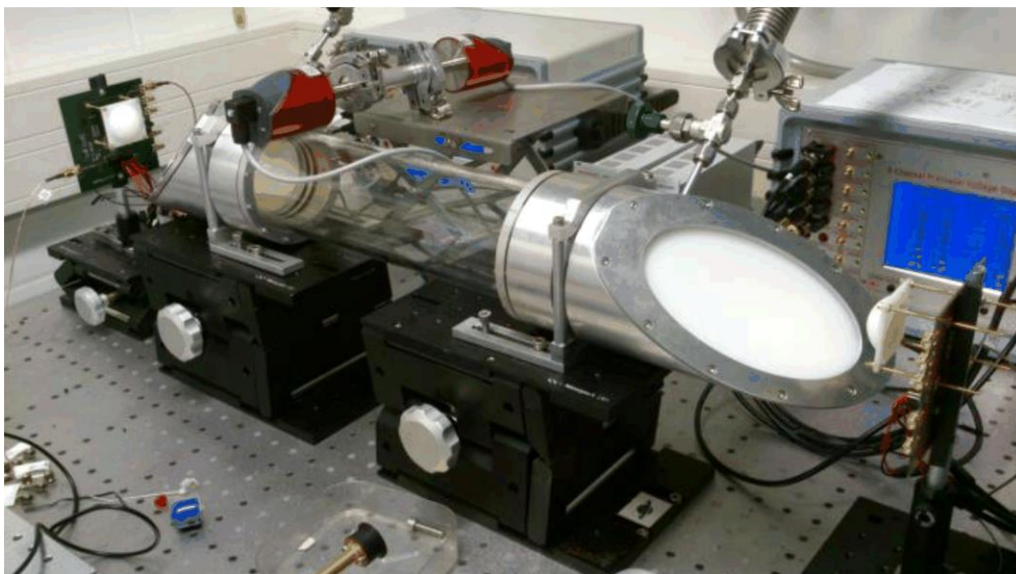
Figure 6.11: Photograph of the TX/RX system demonstrator
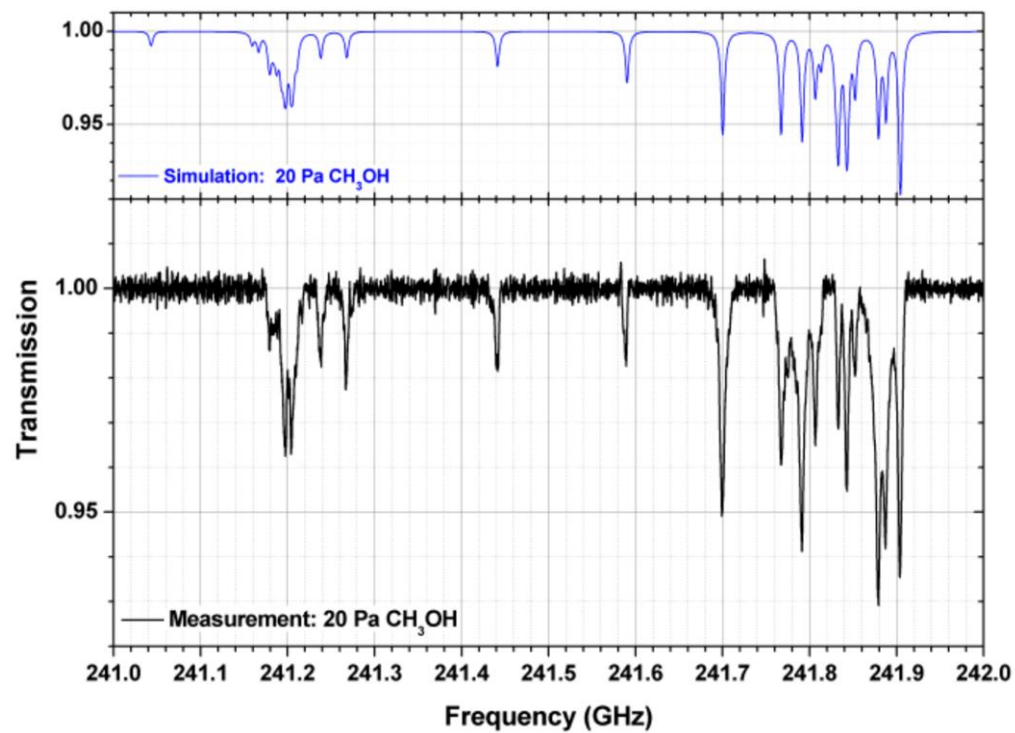
with gas absorption cell



Figure 6.12: Spectrum of methanol: measured spectrum after averaging of data

points and base line correction (bottom) and simulated spectrum (top)

# 7    Conclusion and Outlook

In chapter 2, three types of IHP SiGe BiCMOS technologies are introduced. Design model and RF models for passives like MIM capacitors, resistors in the design kit are explored. Bondpad and probe pad design was discussed. The advantages and disadvantages of spiral inductors vs. transmission lines beyond 100 GHz are discussed. Transmission lines are chosen to be utilized as inductors for circuits beyond 100 GHz.

Three types of transmission lines are designed and simulated using an EM field solver. A comparison and discussion of the three types of transmission lines is given. For an experimental validation of the usefulness of the different transmission line types, 122 GHz LNAs with the three transmission line topologies are designed, measured and compared. Good agreement is achieved between the simulation and measurement results. TL A with highest Q leads to highest LNA gain. Full-chip EM simulation methodology can achieve best accuracy in design. Nevertheless it was shown that a design methodology with conventional transmission line models can already achieve enough accuracy. And given with frequency margin in simulation redesigned LNAs are successfully achieved to solve the problem of frequency shift. This investigation was published in [16].

Noise analysis of HBTs yields $NF_{min}$ of the transistor in terms of current gain of the transistor, transistor transconductance, base resistance and transit frequency. It was found out that for extreme high-frequency LNA design, in order for the transistors to work at extreme high-frequency, transistors are biased close to the peak $f_T$ instead at minimum $NF_{min.}$

A four stage common base LNA topology was investigated. In simulation, the common base topology has much better gain performance than common emitter topology per stage. Comparing common base of 2 stages with cascode topology, gain of common base topology is a little higher than cascode, and noise figure is 1dB less than that of cascode topology. Power dissipations of the two are comparable.

A four stage common base 245 GHz LNA is designed and measured in 0.25 um SG25 H1 BiCMOS (DotFive) technology. A four stage common base 245 GHz LNA with 12 dB gain, 25 GHz 3-dB bandwidth, and a small power dissipation of 28 mW is demonstrated[19]. The base bias voltage decreased to reduce current density compared with that in simulation. This phenomenon is explained and verified well by including a parasitic inductance between the base terminal and ground. Measurement results agree well with the simulation.

A modified common base LNA is designed and measured in SG13G2 BiCMOS technology. S21 of the CB LNA has a 3-dB bandwidth extending from 237 GHz to 261 GHz. A gain of 11 dB is achieved at 243 GHz. S11 and S22 are below -4 dB at 245 GHz. The simulated NF is 12 dB.[1]

Three different kinds of subharmonic mixers were investigated: active subharmonic mixer, transconductance subharmonic mixer and passive subharmonic mixer. Comparing active SHM with transconductnce SHMs, active SHM does not behave like switches at frequencies near the $f_T$ of the transistors while transconductance SHMs still function well even for frequencies beyond $f_T$ (or $f_{max}$) [10]. Comparing passive SHM with SHMs based on active SHM, passive SHM dissipates no DC power. Based on all these above mentioned considerations, two subharmonic mixers, the transconductance SHM and the passive SHM are studied, simulated, measured and compared in this work.

The conversion gain of 4th transconductance SHM is -7 dB when the RF frequency is 245 GHz with a 3 dB bandwidth (-9 to -6dB) from 240.5 GHz to 252.7 GHz. [23] Conversion gain of the 2nd transconductance SHM is extracted by subtracting the S21 of CB LNA [1] from the conversion gain of integrated receiver [27]. The conversion gain of 2nd transconductance SHM is 5 dB when the RF frequency is 245 GHz with a 3 dB bandwidth from 236 GHz to 256 GHz.

With fixed VCO tuning voltage $V_{tune}$ of 1.3 V with corresponding VCO-frequency at 122 GHz, when the input RF frequency is swept, the passive SHM achieves a conversion loss of 16 dB when the RF frequency is approaching 244 GHz, with the 3-dB RF frequency bandwidth extending from 241.5 GHz to 246.5 GHz. For conversion loss of the passive SHM versus RF frequency with fixed IF frequency 1 GHz, input RF frequency is swept from 236 GHz to 255 GHz simultaneously when LO frequency changes from 116.9 GHz to 126.4 GHz by increasing the tuning voltage $V_{tune}$ from 0 V to 3 V to keep the IF frequency constant. Passive SHM achieves 3-dB RF frequency bandwidth extending from 236 GHz to 250 GHz, with a 14 GHz 3-dB bandwidth.[24]

Based on the LNA and SHM implementations , three kinds of subharmonic receivers were realized and presented: 4th transconductance subharmonic receiver, 2nd transconductance subharmonic receiver and 2nd passive subharmonic receiver.

In section 5.6, table 5.2 summarizes the performance comparison of the three receivers with state of the art and shows that the subharmonic receivers are favourable compared with the published results of other groups.

In chapter 6, sensitivity and dynamic range of receiver is discussed. Based on a partly heuristic metric, sensitivity and dynamic range of 2nd transconduct-

ance subharmonic receiver is calculated as follows: $P_{sensitivity}$ is -79.62 dBm, and DR is 55.62 dB.

On chip measurement setup of the $2^{nd}$ transconductance subharmonic receiver was introduced. On-chip measurement of the receiver is performed and according to Friis power transmission equation, the conversion gain of the receiver can be calculated and obtained.

A demonstrator of the gas spectroscopy uses an optical bench for movable mounting of TX and RX boards. In a first experiment with TX and RX 1.5 meter apart, by simultaneously changing the reference signal of the two PLLs in TX and RX, a fixed IF frequency was obtained. TX frequency changes from 236.4 GHz to 252 GHz, while LO frequency of RX changes from 236.5 GHz to 252.1 GHz. The power of the IF signal versus RF frequency was measured with good results. According to Friis power transmission equation, assuming the far field condition, the conversion gain of the receiver was calculated.

By using a 0.6m long gas absorption cell between TX and RX , a gas spectroscopy demonstrator was built in cooperation with colleagues at IHP. The applicability of sensor system was demonstrated by the measured spectra of methanol. Figure 6.12 in section 6.4 shows the absorption spectrum of methanol with gas pressure of 20 Pa after processing of data from spectrum analyzer. An excellent agreement between the simulated and the measured spectrum was achieved [33].

In a future project, work will continue with the target to design transmitter and receivers at 480 GHz or 720 GHz. The RF circuit design will strive for even higher frequency. Various circuit topologies will be investigated to find the most suitable one for future transmitter and receiver design.

# 8 References

[1] Y. Mao, K. Schmalz, J. Borngräber, and J. C. Scheytt, "245-GHz LNA, Mixer, and Subharmonic Receiver in SiGe Technology," IEEE Trans. Microw. Theory Tech., vol. 60, no. 12, pp. 3823–3833, 2012.

[2] Infrared spectroscopy: fundamentals and applications, Barbara Stuart, Wiley, 1st edition, 2004.

[3] I. R. Medvedev, C. F. Neese, G. M. Plummer, and F. Lucia, "Submillimeter spectroscopy for chemical analysis with absolute specificity," in Optics Letters, vol. 35, no. 10, 2010, pp. 1533–1535.

[4] E. Öjefors, B. Heinemann, and U. R. Pfeiffer, "Subharmonic 220- and 320-GHz SiGe HBT receiver front-ends," IEEE Trans. Microw. Theory Tech., vol. 60, no. 5, pp. 1397–1404, 2012.

[5] Y. Sun and J. Borngräber and F. Herzel and W. Winkler, "A fully integrated 60 GHz LNA in SiGe:C BiCMOS technology," in IEEE BCTM, 2005, pp. 14–17.

[6] W. Winkler, W. Debski, B. Heinemann, F. Korndorfer, H. Rücker, K. Schmalz, J. C. Scheytt, and B. Tillack, "122 GHz low-noise-amplifier in SiGe technology," in IEEE ESSCIRC, 2009, pp. 316–319.

[7] K. Schmalz, J. Borngraber, M. Yanfei, H. Rucker, and R. Weber, "A 245 GHz LNA in SiGe Technology," IEEE Microw. Wireless Compon. Lett., vol. 22, no. 10, pp. 533–535, 2012.

[8] A. Müller and M. Thiel and H. Irion and H. ÜO. RuoSS, "A 122 GHz SiGe active subhamronic mixer," in European Gallium Arsenide and other semiconductor application symposium, 2005, pp. 57–60.

[9] J.-J. Hung, T. Hancock, and R. G.M., "A 77 GHz SiGe sub-harmonic balanced mixer," IEEE J. Solid-State Circuits, vol. 40, no. 11, pp. 2167–2173, 2005.

[10] E.Öjefors and B.Heinemann and U.R.Pfeiffer, "A 650 GHz SiGe receiver front-end for Terahertz imaging arrays," in IEEE ISSCC Symp. Dig, 2010, pp. 430–431.

[11] Michael W. Chapman and Sanjay Raman, "A 60-GHz uniplanar MMIC 4x subharmonic mixer," in IEEE IMS Symp. Dig, 2001, pp. 95–98.

[12] D. M. Pozar, Microwave Engineering. John Wiley Sons, Inc., 2012.

[13] K. Schmalz, W. Winkler, J. Borngräber, W. Debski, B. Heinemann, and

J. Scheytt, "A Subharmonic Receiver in SiGe Technology for 122 GHz Sensor Applications," IEEE J. Solid-State Circuits, vol. 45, no. 9, pp. 1644–1656, 2010.

[14] D. Van-Hoang, V. Subramanian, and G. Boeck, "60 GHz SiGe LNA," in IEEE ICECS, 2007, pp. 1209–1212.

[15] U. R. Pfeiffer, C. Mishra, R. M. Rassel, S. Pinkett, and S. K. Reynolds, "Schottky Barrier Diode Circuits in Silicon for Future Millimeter-W ave and Terahertz Applications," IEEE Trans. Microw. Theory Tech., vol. 56, no. 2, pp. 364–371, 2008.

[16] Y. Mao, K. Schmalz, J. Borngräber, and J. C. Scheytt, "Comparison of 122 GHz LNAs in SiGe with different transmission line topologies," in IEEE MTT-S Internationa Microwave Workshop Series on Millimeter Wave Integration Technologies (IMWS), 2011, pp. 152–155.

[17] W. Winkler, J. Borngräber, H. Gustat, and F. Korndorfer, "60 GHz transceiver circuits in SiGe:C BiCMOS technology," in IEEE ESSCIRC, 2004, pp. 83–86.

[18] H. Rücker, B. Heinemann, R. Barth, J. Bauer, K. Blum, D. Bolze, J. Drews, G. G. Fischer, A. Fox, O. Fursenko, T. Grabolla, U. Haak, W. Höppner, D. Knoll, K. Köpke, B. Kuck, A. Mai, S. Marschmeyer, T. Morgenstern, H. H. Richter, P. Schley, D. Schmidt, K. Schulz, B. Tillack, G. Weidner, W. Winkler, D. Wolansky, H.-E. Wulf, and Y. Yamamototo, "SiGe BiCMOS technology with 3.0 ps gate delay," IEEE Int. Electron Device Meeting, pp. 651–654, 2007.

[19] Y. Mao, K. Schmalz, J. Borngräber, and J. C. Scheytt, "A 245 GHz CB LNA in SiGe," in European Microwave Integrated Circuits Conference (EuMIC), 2011, pp. 224–227.

[20] B. Heinemann, R. Barth, D. Bolze, J. Drews, G. Fischer, A. Fox, and et al, "SiGe HBT technology with fT/fmax of 300 GHz/500 GHz and 2.0 ps CML gate," in IEEE IEDM, 2010, pp. 30.5.1–30.5.4.

[21] P. R. Gray, P. J. Hurst, S. H. Lewuis, and R. G. Meyer, Analysis and design of analog integrated circuits. John Wiley Sons, Inc., 2001.

[22] Y. Sun and C. Scheytt, "A 122 GHz Sub-Harmonic Mixer With a Modified APDP Topology for IC Integration," IEEE Microw. Wireless Compon. Lett., vol. 21, no. 12, pp. 679–681, 2011.

[23] Y. Mao, K. Schmalz, J. Borngräber, and J. C. Scheytt, "A 245 GHz CB LNA and SHM mixer in SiGe technology," in 12th Topical Meeting on Silicon Monolithic Integrated Circuits in RF Systems (SiRF), 2012, pp. 5–8.

[24] Y. Mao, K. Schmalz, J. Borngräber, J. C. Scheytt, and C. Meliani, "245 GHz subharmonic receivers in SiGe," in IEEE Radio Frequency Integrated Circuits Symposium (RFIC), 2013, pp. 101–104.

[25] K. Schmalz, W. Winkler, J. Borngräber, W. Debski, B. Heinemann, H. Rücker, and J. Scheytt, "A 245 GHz transmitter in SiGe technology," in IEEE RFIC, 2012, pp. 195–198.

[26] Ojefors E. and Pfeiffer, U., "A 94-GHz Monolithic Front-End for Imaging Arrays in SiGe:C Technology," in IEEE EuMIC, 2008, pp. 252–254.

[27] Y. Mao, K. Schmalz, J. Borngräber, J. C. Scheytt, and C. Meliani, "245 GHz subharmonic receiver in SiGe," in IEEE MTT-S International Microwave Symposium Digest (IMS), 2013, pp. 1–4.

[28] M. Abbasi, S. E. Gunnarsson, N. Wadefalk, R. Kozhuharov, J. Svedin, S. Cherednichenko, I. Angelov, I. Kallfass, A. Leuther, and H. Zirath, "Single-chip 220-GHz active heterodyne receiver and transmitter MMICs with on-chip integrated antenna," IEEE Trans. Microw. Theory Tech., vol. 59, no. 2, pp. 466–478, 2011.

[29] S. Gunnarsson, N. Wadefalk, J. Svedin, S. Cherednichenko, I. Angelov, H. Zirath, I. Kallfass, and A. Leuther, "A 220 GHz single-chip receiver MMIC with integrated antenna," IEEE Microw. Wireless Compon. Lett., vol. 18, no. 4, pp. 284–286, 2008.

[30] K. Schmalz, J. Borngräber, W. Ruoyu, M. Yanfei, and C. Meliani, "Sub-harmonic 245 GHz SiGe receiver with antenna," in IEEE EuMic, 2013, pp. 121–124.

[31] K. Schmalz, W. Ruoyu, J. Borngräber, W. Debski, W. Winkler , and C. Meliani, "245 GHz SiGe transmitter with integrated antenna and external PLL," in IEEE IMS, 2013, pp. 1–3.

[32] Slides for "Integrated Circuits for Wireless Communications" , Paderborn University.

[33] K. Schmalz, Y. Mao,  J. Borngräber, P. Neumaier and H.-W. Hübers, "Tunable 245 GHz transmitter and receiver in SiGe technology for gas spectroscopy", IEEE Electronic Letters, vol. 50, no. 12, 2014, pp. 881-882.

[34] Slides for "Microwave circuit design", TU Delft.

[35] S. Decoutere, S. Van Huylenbroeck, B. Heinemann, A. Fox, P. Chevalier, A. Chantre, T. F. Meister, K. Aufinger, and M. Schröter, "Advanced process modules and architecture, " in Proc. BCTM 2009, Oct. 2009, pp. 9-16.

[36] IHP Dotfive25B process specification.

[37] H. Rücker, B. Heinemann, W. Winkler, R. Barth, J. Borngräber, J. Drews, G. Fischer, A. Fox, T. Grabolla, U. Haak, D. Knoll, F. Korndörfer, A. Mai, S. Marschmeyer, P. Schley, D. Schmidt, J. Schmidt, K. Schulz, B. Tillack, D. Wolansky, and Y. Yamamoto, "A 0.13 μm SiGe BiCMOS technology featuring fT/fmax of 240/330 GHz and gate delays below 3 ps," in Proc. BCTM Conf., 2009, pp. 166-169.

[38] IHP SG13B/SG13S process specification.

[39] H. Rücker, B. Heinemann, A. Fox, "Half-Terahertz SiGe BiCMOS Technology", IEEE SiRF, 2012, pp. 133-136.

[40] IHP SG13G2 process specification.

[41] ADS 2012 help.

[42] The Design of CMOS Radio-Frequency Integrated Circuits, Th. Lee, Cambridge University Press 2004, 2nd edition.

[43] High-Frequency Integrated Circuits, S. Voinigescu, Cambridge University Press, 2013.

[44] Guofu Niu, "Noise in SiGe HBT RF Technology: Physics, Modeling, and Circuit Implications", proceedings of the IEEE, vol. 93, no. 9, 2005, pp. 1583-1597.

[45] Ruoyu Wang, Yaoming Sun, Kaynak M., Beer Stefan, Borngraber J, Christoph Scheytt J, "A micromachined double-dipole antenna for 122 – 140 GHz applications based on a SiGe BiCMOS technology", IEEE IMS 2012, pp. 1-3.

[46] Bradley Richard Jackson, "Subharmonic Mixers in CMOS Microwave Integrated Circuits", PHD thesis, Queen's University Kingston, Ontario, Canada March 2009.

Orin007nal Publication List

• Yanfei Mao and K. Schmalz and J. Borngräber and J. C. Scheytt, "245-GHz LNA, Mixer, and Subharmonic Receiver in SiGe Technology," in IEEE TMTT, vol. 60, no.12, pp. 3823-3833, 2012.

• Yanfei Mao and K. Schmalz and J. Borngräber and J. C. Scheytt, "Comparison of 122 GHz LNAs in SiGe with different transmission line topologies," in IEEE MTT-S Internationa Microwave Workshop Series on Millimeter Wave Integration Technologies (IMWS), pp. 152-155, Feb. 2011.

• Yanfei Mao and K. Schmalz and J. Borngräber and J. C. Scheytt, "A 245 GHz CB LNA in SiGe," European Microwave Integrated Circuits Conference (EuMIC), pp. 224-227, 2011.

• Yanfei Mao and K. Schmalz and J. Borngräber and J. C. Scheytt, "A 245 GHz CB LNA and SHM mixer in SiGe technology," in 12th Topical Meeting on Silicon Monolithic Integrated Circuits in RF Systems (SiRF), pp.5-8, 2012.

• Y. Mao and K. Schmalz and J. Borngräber and J. C. Scheytt, "245 GHz subharmonic receiver in SiGe," in 7th European Microwave Integrated Circuits Conference (EuMIC), pp. 183-186, 2012.

• Yanfei Mao and K. Schmalz and J. Borngräber and J. C. Scheytt and C. Meliani, "245 GHz subharmonic receivers in SiGe," in IEEE Radio Frequency Integrated Circuits Symposium (RFIC), pp. 101-104, 2013.

• Y. Mao and K. Schmalz and J. Borngräber and J. C. Scheytt and C. Meliani, "245 GHz subharmonic receivers in SiGe," in IEEE MTT-S International Microwave Symposium Digest (IMS), pp. 1-4, 2013.

**Lebenslauf**

| | |
|---|---|
| Name | Yanfei |
| Vorname | Mao |
| Wohnort | Yiwu |
| Geburtsdatum/-ort | 01.09.1983 |
| Nationalität | Chinesisch |
| Familienstand | ledig |

**Schulbildung**

| | |
|---|---|
| 09/1990 - 07/1995 | Grundschule |
| 09/1995 - 07/1998 | Junior Mittelschule |
| 09/1998-07/2001 | Gymnasium |

**Studium**

| | |
|---|---|
| 09/2002 - 07/2006 | Zhejiang University |
| 09/2006 - 07/2007 | Fudan University |
| 09/2007 - 07/2009 | TU Delft |
| 09/2009 - 10/2014 | Universität Paderborn |

**Wissenschaftliche Tätigkeit**

| | |
|---|---|
| 09/2009 - 10/2014 | IHP GmbH |

| | |
|---|---|
| **Sprachkenntnisse** | Englisch |
| | Chinesisch |

Ort, Datum

Unterschrift

**Drei Stichwörter für den Deutschen Fakultätentag zur Dissertation:**

- 245 GHz
- Subharmonic receivers
- Gas spectroscopy